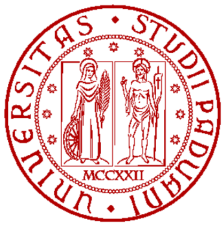

**Università degli Studi di Padova**

Dipartimento di Fisica e Astronomia "Galileo Galilei"

Corso di Dottorato di Ricerca in Fisica – XXX ciclo

Tesi di Dottorato di Ricerca in Fisica

# New Perspectives in Nanodosimetry

**Coordinatore:** Ch.mo Prof. Gianguido Dall'Agata
**Supervisore:** Dott.ssa Valeria Conte
**Referente Interno:** Ch.ma Prof.ssa Silvia M. Lenzi

**Dottoranda:** Anna Selva

Anno Accademico 2017/2018

*A Davide,*
*ancora una volta.*
*E al futuro che verrà.*

University of Padua
Department of Physics and Astronomy "Galileo Galilei"

PhD Course in Physics – XXX cycle

Doctoral Thesis in Physics

# New Perspectives in Nanodosimetry

Presented by **Anna Selva**

**Course Coordinator:** Prof. Gianguido Dall'Agata
**Supervisor:** Dr. Valeria Conte
**University co-supervisor:** Prof. Silvia M. Lenzi

**Abstract**

The biological effectiveness of ionizing radiation is closely related to the number and spatial distribution of its initial interactions within critical subcellular structures of nanometric size, such as the DNA. The detailed analysis of this interaction pattern is the main aim of nanodosimetry, which is the study of the stochastics of radiation interactions at the nanometre scale.

At the Legnaro National Laboratories of the Italian Institute of Nuclear Physics, the Startrack nanodosimetric counter is operative, which can measure the ionization yield in sensitive volumes of nanometric size. From these data, new track structure descriptors can be defined, which are measurable and directly correlated to given biological effects.

This thesis aims at the development of new techniques and methodologies to be applied to the nanodosimetric analysis, in order to optimize the correlation between the physical description of track structure given by nanodosimetry and biological effects at cellular level, as a first step towards its application to radiation therapy and radiation protection.

*The work described in this thesis has been carried out at the Legnaro National Laboratories of the Italian National Institute of Nuclear Physics, in the framework of the experiments MITRA and NADIR.*

# Contents

# Chapter 1

# Introduction

The action of ionizing radiation on living organisms takes the form of a complex chain of physical, chemical and biological processes initiated in sub-cellular structures, which can possibly evolve into more or less permanent damage at cellular, tissue or organ level, and in the most severe cases result in the death of the organism itself. Even if the deleterious effects at tissue or organ level can become evident only after days, months or even years after the initial exposure, a correlation must exist between the initial features of radiation interactions and the likelihood of late effects. In the field of human healthcare, both for the protection from hazard radiation exposure and for the optimization of treatment plans in radiotherapy, there is the need to identify physical quantities that are measurable at the relevant target size and suitable to characterize the effectiveness of radiation to induce biological damage.

In radiological clinical practice as well as in radiation protection, the likelihood of late biological effects is generally correlated to the absorbed dose $D$, which is defined as the mean energy $\mathrm{d}\bar{\varepsilon}$ imparted by ionizing radiation to a given volume of matter, divided by its mass $\mathrm{d}m$ (ICRU, 2011):

$$D = \frac{\mathrm{d}\bar{\varepsilon}}{\mathrm{d}m} \tag{1.1}$$

The unit of absorbed dose is the Gray [Gy], which corresponds to 1 J/kg. However, absorbed dose alone is not enough to quantify the effectiveness of ionizing radiation. For the same absorbed dose, particles of different type and energy induce varying amount of damage: lower for photons and electrons, higher for protons, neutrons or heavier ions.

These differences in radiation response for particles of different type and energy can be quantified, for instance, by means of clonogenic assays, which assess the fraction of surviving[(1)] cells after irradiation with a given dose. By repeating the assay for different dose levels, survival curves can be drawn to describe cell survival as a function of absorbed dose. Two examples of such curves are reported in Figure 1.1: for a given dose level, the fraction of surviving cells is higher for photon irradiation than for carbon ion. The curve generally exhibits a shoulder when the cells are irradiated with photons or electrons, while its shape is exponential when the irradiation is carried out with protons or heavier ions,

[(1)] A cell is considered as surviving if it is able to produce a colony of at least 50 daughters (corresponding to 5 or 6 duplication cycles). This is done in order to exclude cells which have a limited reproductive capacity as a consequence of radiation damage.

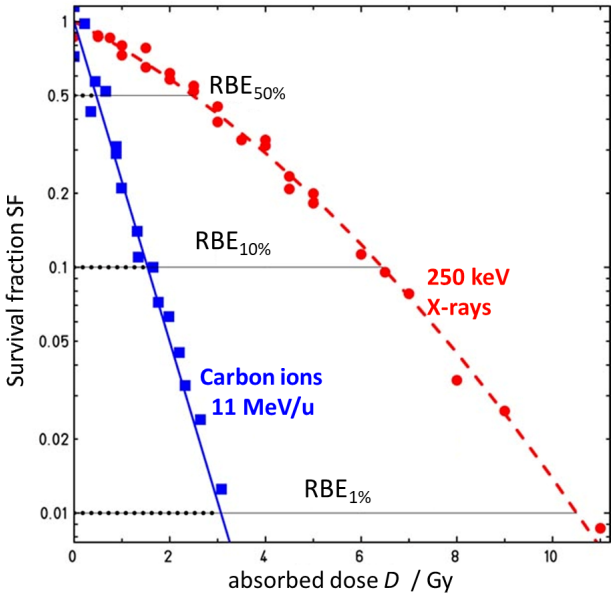


**Figure 1.1:** Examples of cell survival curves for radio-resistant CHO-K1 (Chinese hamster ovary) cells, under irradiation of orthovoltage X-rays and low-energy carbon ions. The variation of the RBE with the survival level is also shown. Modified from (Weyrather, 2004).

especially at low energies. In addition, the shape of the survival curve depends on the intrinsic radiosensitivity of the cell line.

In order to quantify the differences in cell survival curves produced by different radiations, an empirical parameter can be introduced, the *Relative Biological Effectiveness* (RBE). It is defined as the ratio of the absorbed dose of a reference radiation (usually gamma rays from a $^{60}$Co source) and that of the radiation under consideration which must be given in order to obtain the same biological effect. The RBE is 1 for X-rays, gamma rays and high-energy electrons, while it increases to about 3 for carbon ions used in radiotherapy. For any given biological system, the RBE depends on the way the radiation interacts with the system, specifically on the type and spatial distribution of the interactions, which in turn depend on the radiation quality (particle type and energy).

A commonly used descriptor of radiation quality is the (unrestricted) *linear energy transfer* (LET), defined[(2)] as the mean energy lost per unit path length by an incident particle due to electronic interactions, which is numerically equal to the electronic stopping power (ICRU, 2011):

$$\mathrm{LET} = \frac{\mathrm{d}E}{\mathrm{d}l} \tag{1.2}$$

In the above formula, $\mathrm{d}E$ is the energy lost by the incident particle and $\mathrm{d}l$ is the travelled path length.

The variation of RBE for 10% cell survival as a function of LET is shown in Figure 1.2

[(2)] Strictly speaking, the given definition of LET applies only to charged particles. However, a generalization of the LET concept can be made also for indirectly ionizing radiation such as photons or neutrons, based on the average LET of the secondary particles they generate.

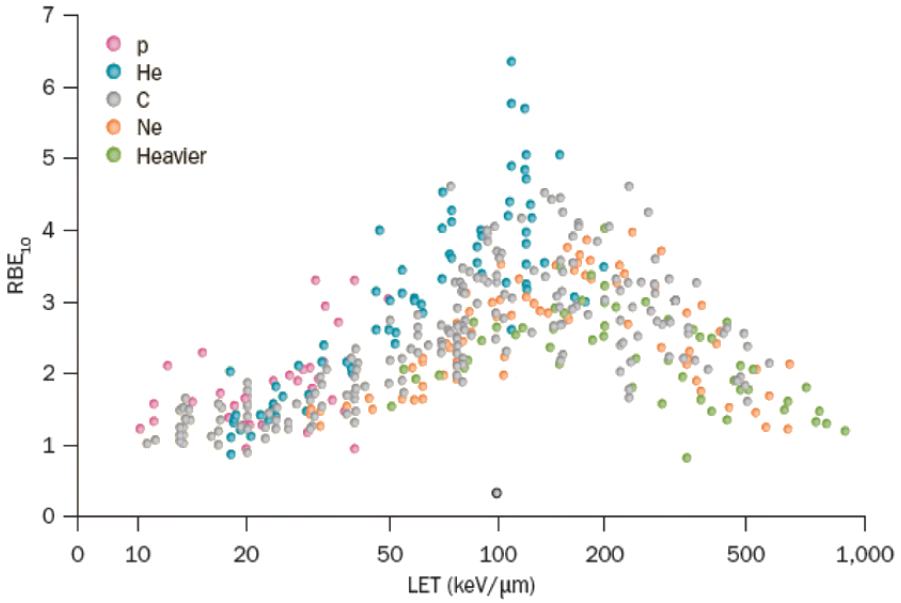


**Figure 1.2:** Dependence of RBE for 10% cell survival on the LET in water of the incident radiation, for different cell lines under proton and light ion irradiation. The data are taken from the PIDE database (Friedrich, 2013). Figure taken from (Durante, 2016).

for different incident radiations: the general trend is an increase up to values of $100 - 150\,\mathrm{keV}/\mu\mathrm{m}$, a maximum and then a decrease for higher LET values (Durante, 2016). However, this unique trend is only a first approximation: at a closer view, particles of the same LET give rise to different RBE. In particular, the position of the maximum is particle-type dependent, and shifted to lower LET values for particles of lower charge state. For the same LET value, low-$Z$ ions are therefore slightly more effective than high-$Z$ ones (Schardt, 2010). The limitations of LET as a radiation quality descriptor are due to the fact that it fails to describe the microscopic pattern of particle interactions, because it does not take into account the fine structure of particle tracks with emerging delta electrons. It is clear that the same LET can be reached by light ions with low velocity or alternatively by heavier particles with higher energy. The track structure of ions at the same LET differs in the penumbra extension, because the energy and range of ejected secondary electrons increase with ion velocity.

As an example, Table 1.1 shows the values of some track-structure parameters for several ions having the same LET of $100\,\mathrm{keV}/\mu\mathrm{m}$. Data refer to propane gas at density of $1\,\mathrm{g/cm^3}$ (Grosswendt,2014). It is worth observing that protons have the smallest specific energy, corresponding to the minimum mean free path for primary ionizations $(\lambda\rho)_{\mathrm{ion}}$ and also to the shortest penumbra radius $(R\rho)_\delta$. The penumbra radius depends only on ion velocity, and not on atomic number or charge.

Because of that, for slower ions the energy deposition is more localized around the primary particle path, and this locally high interaction density can explain the increased effectiveness of protons with respect to that of neon ions of the same LET. The so-called particle track structure, *i.e.* the detailed spatial and temporal pattern of initial interactions, must be taken into account for a full understanding of radiation effects.

| Ion type | $E/m$ [MeV/u] | $(\lambda\rho)_{\text{ion}}$ [$\mu$g/cm$^2$] | Max $E_\delta$ [keV] | $(R\rho)_\delta$ [$\mu$g/cm$^2$] |
|---|---|---|---|---|
| $^{1}$H | 0.15 | 0.0505 | 0.33 | 0.789 |
| $^{4}$He | 1.4 | 0.0563 | 3.0 | 20.5 |
| $^{12}$C | 21 | 0.0590 | 45 | 2150 |
| $^{16}$O | 44 | 0.0631 | 95 | 7800 |
| $^{20}$Ne | 75 | 0.0649 | 163 | 19900 |

**Table 1.1:** Comparison of track structure parameters for particles with the same LET of 100 keV/$\mu$m in propane at unit density: specific energy $E/m$, mass mean free path for primary ionizations $(\lambda\rho)_{\text{ion}}$, maximum energy of the secondary electrons $E_\delta$ and corresponding penumbra radius $(R\rho)_\delta$, calculated according to (Kiefer, 2008).

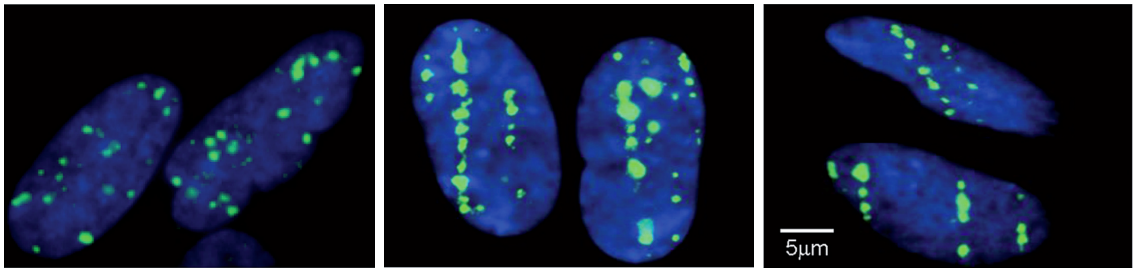


**(a)** $\gamma$ rays **(b)** $^{16}$O **(c)** $^{56}$Fe

**Figure 1.3:** $\gamma$H2AX foci distributions (green blobs) in human skin fibroblast cells (type 82-6) irradiated horizontally with (a) 662-keV gamma rays from a $^{137}$Cs source, (b) 77-MeV/u oxygen ions, (c) 600-MeV/u iron ions. The cells are stained with a DNA marker (blue regions). The tracks of oxygen and iron ions passing through the cells can be clearly identified. From (Wang, 2013).

The importance of track structure for the assessment of biological damage is also confirmed by the analysis of the activity of DNA repair mechanisms, which can be monitored experimentally with immunofluorescence techniques thanks to the phosphorylation (*i.e.*, the addition of a $PO_3{}^{2-}$ 2-phosphoryl group) of the histone protein H2AX (Rogakou, 1998): after the radiation insult, thousands of H2AX proteins near the damaged site are phosphorylated to $\gamma$H2AX, highly amplifying the effect. If these proteins are tagged with fluorescent compounds, the resulting blot (called focus) around the original damage site can be visualized by confocal microscopy, allowing to correlate the spatial distribution of initial lesions with the incident radiation quality, as shown in Figure 1.3. With such an analysis, it can be seen that for gamma radiation the damage is uniformly distributed inside the cell, while for oxygen and iron ions the damage is localized in well-defined spatial positions around the primary particle track. The biological effectiveness of ionizing radiation is therefore critically dependent on particle track structure.

Because of its critical importance for reproduction and all regulatory activities of the cell, it is generally assumed that DNA is the critical target for radiation action (Goodhead, 1994). The correlation between particle track structure and biological damage should therefore be stronger if the former is studied at the DNA level, *i.e.* considering a spatial

scale of about 1 nm. At this scale, a description based on the continuous slowing-down approximation is not valid and the discrete and stochastic nature of the interaction processes must be taken into account. This is the main aim of nanodosimetry, which is the study of the stochastics of radiation interactions in sensitive volumes of nanometric size.

A complete study of the track structure, including all physical processes at play (elastic scattering, atomic and molecular excitations, ionizations, charge-changing processes...) is nowadays possible by means of Monte Carlo track structure codes (see Chapter 2), provided that a complete and accurate database of interaction cross sections is available. This is not a trivial requirement, since experimental cross section data in the low-energy range are affected by large uncertainties (Nikjoo, 2006; Incerti,2010b). In any case, this approach remains unfeasible experimentally.

Due to this limitation, experimental nanodosimetry studies only the ionization component of particle tracks, which is nowadays possible by means of single-electron or single-ion counting techniques. It is assumed that the stochastics of the ionization process rules the induction of initial DNA damage and that it is still significant to determine the final cellular consequences, in spite of the long and complex chain of intermediate chemical and biological processes (Conte, 2012).

At the Legnaro National Laboratories of the Italian Institute of Nuclear Physics, the Startrack nanodosimetric counter is operative (De Nardo, 2002a). Its core part is an almost wall-less sensitive volume filled with gas at low pressure, with a thickness in mass per area which is the same as that of a nanometric volume at unit density. The number of low-energy electrons produced in this volume by ionizing radiation can be extracted and counted by means of an electron collector and amplification system, allowing the study of the ionization yield as a function of the radiation quality.

An extensive study has already been carried out for many light ions of interest for hadrontherapy, namely, protons, lithium and carbon ions at different energies (Conte, 2012; Conte, 2014), both when the sensitive volume is crossed centrally by the incident beam and when the primary particles pass outside it at a fixed distance. The results of this study showed a consistent characterization of the ionization yield when the counter is filled at the design gas pressure of 300 Pa, corresponding to a mass thickness of 2 $\mu$g/cm$^2$, *i.e.* about 20 nm at unit density. However, it is expected that the correlation between particle track structure and biological response is more direct when the sensitive volume size is closer to DNA dimensions. It is therefore of interest to investigate if the operative range of the Startrack counter can be extended in order to reach a sensitive volume size of about 1 nm.

Apart from the Startrack counter, two other nanodosimeters are operative to date. It has been shown that these devices provide a consistent characterization of particle track structure, based on measurements and taking into account its discrete and stochastic nature. The measurement of the ionization yield obtained with these counters could be the basis for the definition of new physical descriptors of radiation quality, directly correlated with given end-points of biological damage, to be applied in radiation therapy or radiation protection. In this respect, the main drawback of these nanodosimetric counters is that they are designed for fundamental research and are therefore very complex and bulky, not suited for an everyday use. The development of a simplified, portable nanodosimeter could pave the way for a more widespread application of nanodosimetry to radiation protection

or radiation therapy.

This thesis has therefore a three-fold objective:

- To characterize the response of the Startrack counter in different operating conditions, in particular, at several gas densities, in order to analyse the stochastics of the ionization yield in a volume about 1 nm in size;
- To study the correlations between initial features of radiation interactions and the likelihood of final biological damage, in order to define new descriptors of radiation quality based on the nanodosimetric analysis of particle track structure;
- To carry out a proof-of-principle study for a portable nanodosimeter, in order to see if a simplified device based on nanoparticles which are sensitive to ionizing radiation can provide enough information for a consistent characterization of particle track structure.

These objectives are analysed in Chapter 4, 5 and 6 respectively, after a description of the state of the art of nanodosimetry, both from the experimental and the computational point of view (Chapter 2), and a detailed description of the structure and working principles of the Startrack counter (Chapter 3). The main results of this work and its future perspectives are finally summarized in the Conclusions.

# Chapter 2

# Nanodosimetry

It has been seen in the Introduction that radiation effects are strongly correlated to the topology of initial physical interactions analysed at the nanometre scale, where the discrete and stochastic nature of the physical processes plays a relevant role. In this respect, nanodosimetry can provide valuable help for the characterization of particle track structure.

At the nanometre scale, radiation effects are due to the incidence of single primary particles, because the probability of two-particle crossing is very low and can be neglected but for very high doses. Nanodosimetry analyses therefore the stochastic of the ionization yield for single particle traversal. Moreover, the investigation is restricted to charged ions and the secondary electrons they produce in sites of nanometric size, because the probability of photon or neutron interactions can be neglected given their much longer scattering length. For the same reason, nuclear reactions induced by charged particles do not play a role.

In experimental nanodosimetry, and in some cases in Monte Carlo simulations as well, it is assumed that from the point of view of particle transport and degradation a sensitive volume of millimetric size in which the density is of the order of $10^{-6}\,\mathrm{g/cm^3}$ (for instance, a gas-filled volume at a pressure of around 100 Pa) is equivalent to a volume of nanometric size at unit density. The ionization yield is assumed to be the same in volumes of identical thickness in mass per area, and differences between gas and condensed phase are assumed to play only a minor role.

This Chapter presents the state of the art of nanodosimetry, both from the experimental and the theoretical point of view: after a discussion of the general methodology of nanodosimetry (valid for both experiment and simulations), the results obtained with the Startrack counter at the standard gas pressure of 300 Pa are discussed for different incident radiation qualities and impact parameters. The experimental cluster size distributions are then used to validate the results of the *MC-Startrack* simulation code, a Monte Carlo track structure code which was specifically developed to simulate step-by-step the electron production and collection from the sensitive volume of the Startrack counter. A theoretical model for the description of particle track structure and a possible procedure to relate the ionization yields in different materials are also discussed. Finally, an experimental finding which could be the basis for a new concept of radiation quality is presented and discussed.

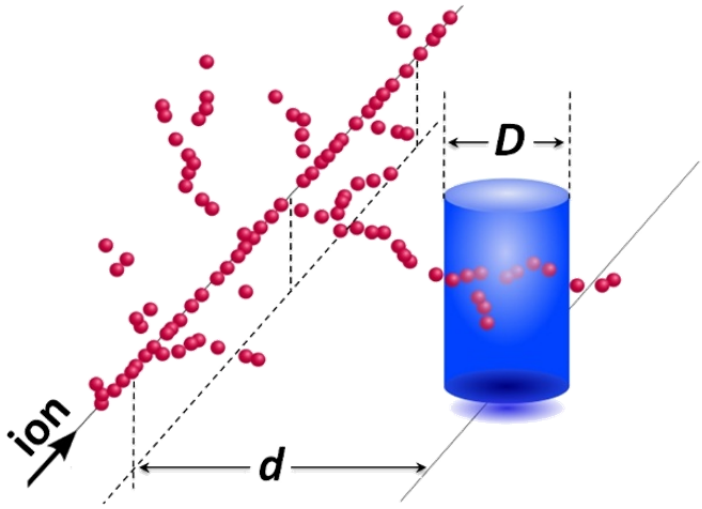


**Figure 2.1:** Pictorial representation of the nanodosimetric analysis: an ionizing particle passes at a distance $d$ from the centre of a cylindrical target volume of diameter $D$. Each red sphere represents an ionization event. At the passage of each primary ion, the number $\nu$ of ionizations inside the target volume is counted, and the ionization cluster-size distribution is derived by repeating this procedure for a huge number of primary particles.

## 2.1 The nanodosimetric analysis

The nanodosimetric study of particle tracks (both experimental and Monte Carlo) focuses on the analysis of the number $\nu$ of ionizations produced inside a sensitive target of equivalent nanometric size at the passage of each primary particle. In such small volumes this magnitude is dominated by its statistical fluctuations, and it must be analysed by considering its probability distribution $P_\nu$, usually called the *ionization cluster-size distribution* (ICSD). This distribution describes the interplay between the track structure of the incident particle and the features of the target volume, and depends on the type and energy of the incident ion, on the shape, size and chemical composition of the target, and on the irradiation geometry (more specifically, from the distance between each particle track and the centre of the target volume, the so-called *impact parameter*).

In practical nanodosimetric experiments as well as in Monte Carlo simulations, once the target geometry and the shape of the radiation field have been defined, a huge number of primary particles is shot towards the target, and the number of ionization induced by each of them inside the sensitive volume is recorded in a histogram. The frequency distribution of the number of ionizations is then derived by normalizing on the total number of primary ions $N_{\mathrm{prim}}$. If $N_{\mathrm{prim}}$ is high enough, the frequency distribution can be used as an estimator for the probability distribution $P_\nu$:

$$P_\nu(Q,d,D) \approx \frac{N_\nu(Q,d,D)}{N_{\mathrm{prim}}} \qquad \text{for} \quad N_{\mathrm{prim}} \to \infty \tag{2.1}$$

The dependence on particle type and energy (*i.e.*, the radiation quality $Q$), on the impact parameter $d$ and on target size $D$ are made explicit. If an extended beam is considered

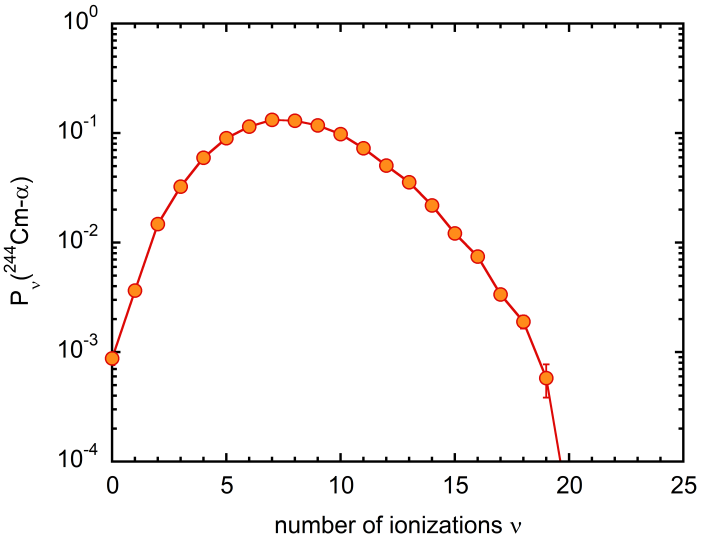


**Figure 2.2:** Ionization cluster-size distribution $P_\nu$ measured with the Startrack counter for $\alpha$ particles from a $^{244}$Cm source in a sensitive volume with a mass thickness of $2\,\mu g/cm^2$.

(*i.e.*, a distribution of different impact parameters is present) the dependence on the beam geometry should also be considered. Since $P_\nu$ is a probability distribution, it is defined for $0 \leq P_\nu \leq 1$; and it is normalized to 1:

$$\sum_{\nu=0}^{\infty} P_\nu(Q,d,D) = 1 \tag{2.2}$$

An example of the shape of the probability distribution $P_\nu$ for $\alpha$ particles produced by a $^{244}$Cm calibration source crossing centrally the target volume (impact parameter $d = 0\,mm$) is shown in Figure 2.2.

From the $P_\nu$ distribution, specific track structure descriptors can be derived. The most straightforward are the moments $M_\xi$:

$$M_\xi = \sum_{\nu=0}^{\infty} \nu^\xi P_\nu(Q,d,D) \tag{2.3}$$

The first moment $M_1$ for $\xi = 1$ corresponds to the mean number of ionizations produced by particles of that type and energy inside the target volume, while the second moment $M_2$ is related to the variance of the distribution, which is $M_2 - M_1^2$.

The inverse cumulative distribution function $F_k$ can also be defined:

$$F_k = \sum_{\nu=k}^{\infty} P_\nu(Q,d,D) \tag{2.4}$$

It follows from this definition that $F_k$ can increase up to a maximum value of 1. The $F_k$ values correspond to the probability of measuring $k$ or more ionizations in a nanometric target volume at the passage of each primary particle: they are therefore related to the degree of complexity of the damage.

## 2.2 Nanodosimetric counters

In order to count the number of ionizations produced by incident primary particles, two different approaches can be used: one based on the counting of the low-energy electrons produced in the ionization process, the other based on the counting of ions. The latter has the advantage that ions have a higher mass and do not easily escape the target volume, improving the detection efficiency. However, they are difficult to separate in time due to their low diffusion, and the recombination probability is high. The ions must therefore be extracted from the interaction region and amplified in vacuum, requiring a differential pumping system. The counting of electrons does not require a vacuum stage, however, their efficient collection is more difficult due to their lower mass.

Three different nanodosimeters are operative at present: the *Startrack Counter* at the Legnaro National Laboratories of INFN, the *Ion Counter* installed at the Physikalisch-Technische Bundesanstalt in Germany, and the *Jet Counter* developed at the National Centre for Nuclear Research in Poland. Differently from the Startrack counter, the latter two are based on ion-counting techniques. A fourth counter, based on the same design of the Ion Counter, was developed and installed at the Loma Linda University Medical Centre (Bashkirov, 2006), but is no longer operative to date.

The Startrack counter is based on single-electron counting techniques and was developed with the aim of studying the ionization yield of different charged ions at varying distance from the primary particle track: it is therefore installed on a movable platform in order to move it orthogonally to the beam trajectory (De Nardo, 2002a). The main idea on which the design is based is to separate physically the region of production of the electrons (the so-called *interaction region*) from that of amplification, by means of a transfer section in which the electrons are separated in time so that they reach the multiplication stage individually (De Nardo, 2002b). Each electron gives therefore rise to a single pulse, and gas gain fluctuations do not affect the information on the number of initial ionizing events. A schematic drawing of the counter is shown in Figure 2.3; a detailed analysis of its structure and working principles can be found in Chapter 3.

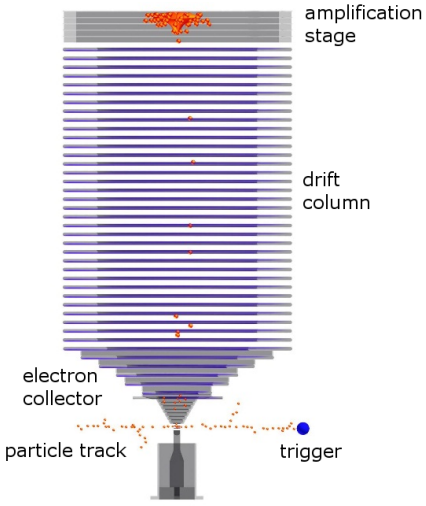


**Figure 2.3:** Startrack Counter: schematic drawing of the operation principle.

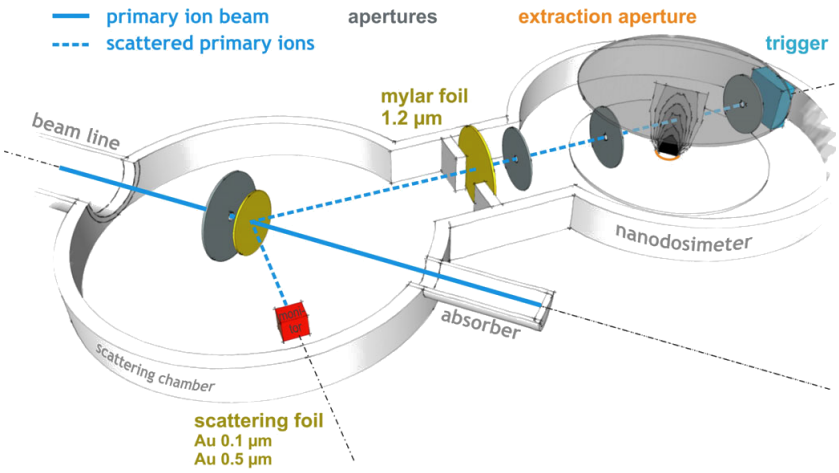


**Figure 2.4:** Ion Counter: schematic drawing of the operation principle. From (Hilgers, 2015).

The wall-less sensitive volume of the counter is a cylinder 3.7 mm in both diameter and height. It is filled with pure propane at a pressure that can in principle be varied to change its mass thickness. The design has however been optimized for a standard pressure of 300 Pa, corresponding to a mass thickness of $2\,\mu g/cm^2$. In this configuration, the average detection efficiency is about 20%.

The Ion Counter (Garty, 2002) consists of a low-pressure cylindrical interaction chamber, connected to an acceleration stage in vacuum. The interaction chamber contains a wall-less sensitive volume defined by a parallel-plate capacitor with a hole 1 mm in diameter on the bottom electrode, which connects it to the following acceleration stage. The distance between the two plates of the capacitor is 50 mm. Rutherford scattering on a gold foil is used in order to reduce the beam intensity before its entrance in the gas-filled chamber.

Primary particles cross the sensitive volume and then hit a trigger detector which gives the start signal for the acquisition. The ions produced by ionizations in the gas drift towards the aperture due to the low electric field which is present between the capacitor plates, and are then collected by an ion counter located in the acceleration stage. Only the ions produced above the extraction aperture can be collected effectively; however, the exact shape and size of the target volume is defined by means of an efficiency map contour, and depends on the gas pressure inside the interaction chamber and on the electric field both in the parallel-plate capacitor and in the acceleration stage. The Ion Counter is usually operated with propane or nitrogen. A schematic drawing of its operating principle is reported in Figure 2.4.

The Jet counter (Pszona, 2000) consists of a stainless steel cylindrical interaction chamber, 10 mm in diameter and 5 mm in height, separated from a gas reservoir by means of a piezoelectric valve. When the valve is opened, a jet of nitrogen expands into the interaction chamber through a nozzle 1 mm in diameter, and is ionized by the incident particles which cross the interaction chamber at half its height. The ions are then extracted from the cavity into a vacuum chamber by means of an electric field defined by a grid; another grid guides them to the amplification stage. A turbomolecular pump ensures the removal

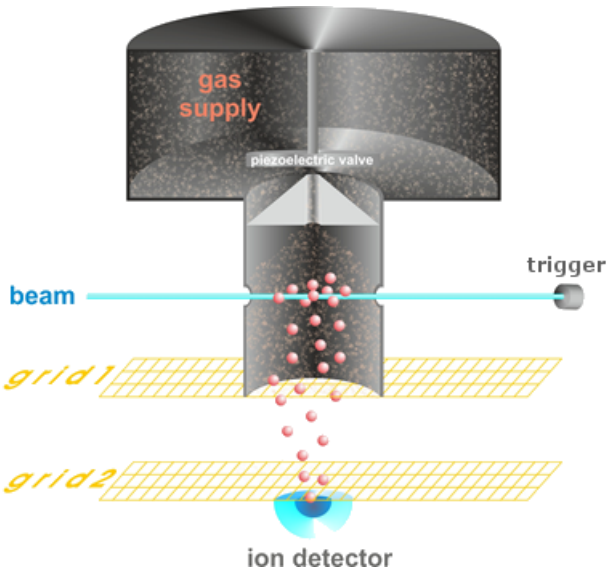


**Figure 2.5:** Jet Counter: schematic drawing of the operation principle.

of the residual nitrogen before the following gas jet.

The equivalent size of the target volume depends on the gas pressure inside the reservoir and the opening time of the valve; and is assessed by measuring the transmission of mono-energetic electrons through the gas layer. Such measurements have also shown that the sensitive volume is well defined only for about 200 $\mu$s; an electronic gate is therefore used to count only the ions produced in this time window. The average detection efficiency is about 40%. A schematic drawing of the Jet Counter is shown in Figure 2.5. This counter can also measure the cluster size distribution produced by incident primary electrons (Bantsar, 2006); however, in this case the measured distribution is due to more than one electron, due to their large angular scattering which makes the development of a proper trigger difficult. The single-event cluster size distribution is therefore derived from a deconvolution procedure, assuming a Poissonian time structure of the primary beam.

An example of the ionisation cluster size distribution measured with the three different counters is reported in Figure 2.6: their shape is markedly different, due to the different response function of each detector. In particular, the one measured by the Jet counter is peaked at a lower cluster size, because its sensitive volume is the smallest of the three, while the distribution measured by the Ion counter is shifted to higher cluster sizes, because of its higher detection efficiency which allows to analyse bigger clusters as well.

## 2.3 Experimental nanodosimetry with the Startrack counter

An extensive study of particle track structure has been carried out with the Startrack counter in the standard working conditions of 300 Pa of propane pressure, corresponding to a mass thickness of the sensitive volume of 2 $\mu$g/cm$^2$ (Conte, 2012; Conte, 2014). The ionization cluster size distributions $P_\nu(Q, d, D)$ have been measured for protons, deuterons, lithium and carbon ions, at several incident energies and impact parameters. The impact

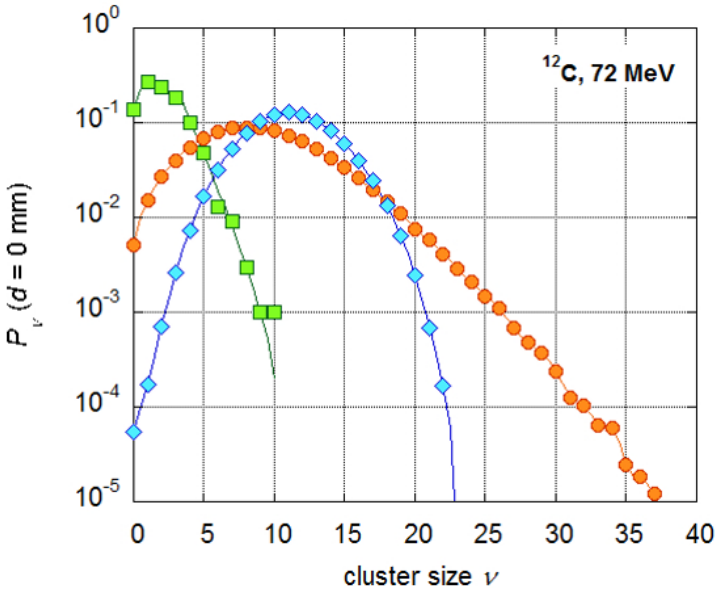


**Figure 2.6:** Ionization cluster size distributions measured with the Jet counter (green), the Ion counter (orange) and the Startrack counter (blue), for 72-MeV carbon ions at impact parameter $d = 0$ mm.

| Ion type | $E$ [MeV] | $E/m$ [MeV/u] | $(\lambda\rho)_{\text{ion}}$ [$\mu$g/cm$^2$] | $D/\lambda_{\text{ion}}$ | Max $E_\delta$ [keV] | Max $(R\rho)_\delta$ [$\mu$g/cm$^2$] |
|---|---|---|---|---|---|---|
| $^1$H | 20 | 20 | 2.05 | 1.0 | 43.6 | 2010 |
| $^2$H | 16 | 8 | 0.941 | 2.2 | 17.4 | 411 |
| $^6$Li | 48 | 8 | 0.105 | 19.3 | 17.4 | 411 |
| $^7$Li | 26.7 | 3.81 | 0.0565 | 35.6 | 8.31 | 115 |
| $^{12}$C | 96 | 8 | 0.0261 | 77.6 | 17.4 | 411 |
| $^{12}$C | 240 | 20 | 0.0569 | 35.6 | 43.6 | 2010 |
| $\alpha$ source | 5.8 | 1.45 | 0.0587 | 34.5 | 3.16 | 22.4 |

**Table 2.1:** Summary of the radiation qualities used for the study at 300 Pa of propane pressure. For each primary ion, the following parameters are given: the specific energy $E/m$, the mean free path for primary ionization $(\lambda\rho)_{\text{ion}}$, the mean number of primary ionizations along the target diameter $D/\lambda_{\text{ion}}$, the maximum energy $E_\delta$ of secondary electrons and their corresponding maximum mass range $(R\rho)_\delta$.

parameter $d$ was varied between 0 mm and 8 mm, corresponding to an equivalent distance between 0 and 44 nm, after scaling at unit density. The beam diameter, as defined by the collimators system, was 0.8 mm, corresponding to 4.4 nm at unit density.

Table 2.1 reports the ion type, energy and mass mean free path for primary ionizations of the analysed radiation qualities, together with the maximum energy of the secondary electrons set in motion by the primary ions and an estimation of their maximum range. Even if the penumbra of particle tracks extends to much wider distances than the range of impact parameters considered in this study, about 99% of all ionizing collisions produced by secondary electrons take place within a distance of 50 nm from the primary track (Conte, 2012), and the number of electrons with an energy close to the maximum one is very small.

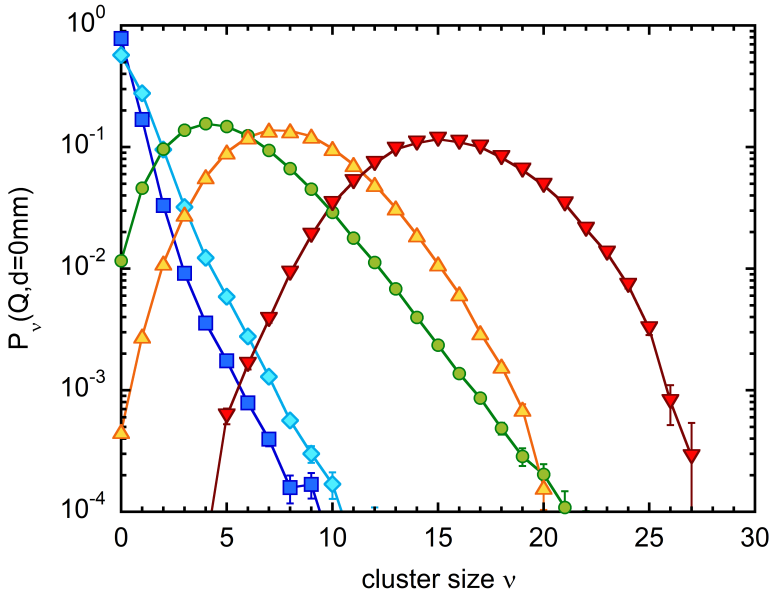


**Figure 2.7:** Ionization cluster size distributions at impact parameter $d = 0\,\mathrm{mm}$ for different radiation qualities: 20-MeV protons (dark blue squares), 16-MeV deuterons (light blue diamonds), 48-MeV $^6$Li ions (green circles), 240-MeV carbon ions (yellow triangles) and 96-MeV carbon ions (red upside-down triangles). Statistical uncertainties are plotted.

In the following, the main results of this study are presented separately for the case of the track core ($d \leq D/2$) and the penumbra region ($d > D/2$). The case of impact parameter $d = 0\,\mathrm{mm}$ is analysed in more detail.

### 2.3.1 Cluster-size distributions in the track core region

Figure 2.7 reports the measured ionization cluster size distributions for 20-MeV protons, 16-MeV deuterons, 48-MeV $^6$Li ions, 240-MeV and 96-MeV carbon ions. The probability distributions have two different shapes: either a monotonic decrease with a maximum at cluster size zero or a peaked shape with a maximum at a cluster size that depends on the radiation quality. This is explained by the different average number of primary ionizations in the sensitive volume, given by $D/\lambda_{\mathrm{ion}}$: in particular, for protons and deuterons this number is 1 and 2 respectively (see Table 2.1), while it is about 20 or higher for all other radiation qualities. Given an average detection efficiency of 20%, these values are in good agreement with the position of the maxima in the cluster size distributions.

The shape of the $P_\nu$ distributions depends therefore critically on the value of $D/\lambda_{\mathrm{ion}}$. Due to this, the distribution for particles of the same charge state is shifted to higher cluster sizes when the velocity is lower, due to the higher ionization cross section at lower specific energy. For particles at the same velocity, the primary ionization cross section scales with the $Z^2$ of the incident ion, shifting the cluster size distribution to higher clusters the higher the ion charge state. For particles of the same $D/\lambda_{\mathrm{ion}}$, the shape of the distribution is approximately the same (Conte, 2014).

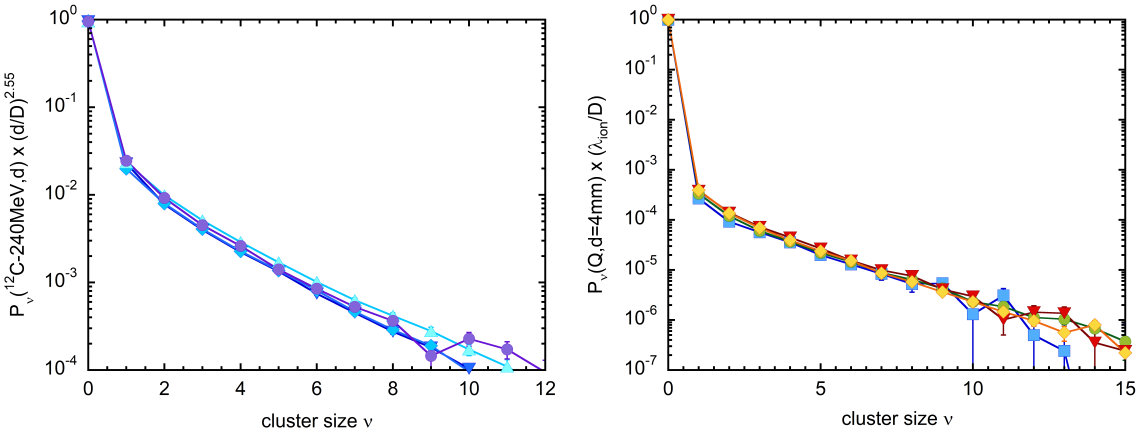


**(a)** **(b)**

**Figure 2.8:** (a) Ionization cluster size distributions for 240-MeV carbon ions at different impact parameters in the penumbra region, scaled by the factor $(d/D)^{-2.55}$: 4 mm (upside-down triangles), 5 mm (diamonds), 6 mm (triangles) and 8 mm (circles); (b) Ionization cluster size distributions at an impact parameter $d = 4$ mm for different radiation qualities, scaled by $D/\lambda_{\mathrm{ion}}$: 96-MeV carbon ions (red upside-down triangles), 26.7-MeV $^{7}$Li ions (yellow diamonds), 48-MeV $^{6}$Li ions (green circles), and 20-MeV protons (blue squares). In both cases, the probability of cluster size zero has been recalculated from the normalization equation.

If other impact parameters in the range $d \leq D/2$ are considered, it is found that the position of the maximum decreases with increasing impact parameter, due to the shortening of the average chord length through the sensitive volume. In the track core region, the shape of the cluster distribution is therefore mainly determined by the ionization mean free path of the primary particle, especially when the latter is short with respect to the dimensions of the sensitive volume. However, the contribution of secondary electrons affects the cluster size distribution, in particular at higher cluster sizes, and cannot be neglected even in the track core region.

### 2.3.2 Cluster-size distributions in the penumbra region

In the penumbra region, it was found that the shape of the cluster size distribution is very similar for all impact parameters and radiation qualities: a high probability of measuring zero electrons followed by an exponential decrease for higher cluster size, with approximately the same slope for all impact parameters. For $\nu > 0$, the distributions differ therefore only by a constant factor. The only exception is the case of $d = 3$ mm, for which a non-constant slope is visible, especially at lower clusters, due to the dense ionization cloud in the immediate vicinity of the primary track.

The decreasing probability of measuring cluster size greater than zero with increasing impact parameter is due to the combined effect of degradation of secondary electrons and reduction of the solid angle under which the sensitive volume is seen by the primary beam. The measured $F_1$ values scale with the impact parameter approximately as $(d/D)^{-2.55}$, almost independently on the radiation quality (Conte, 2012). The dependence of the probability distributions on the impact parameter $d$ is therefore only due to this factor, as

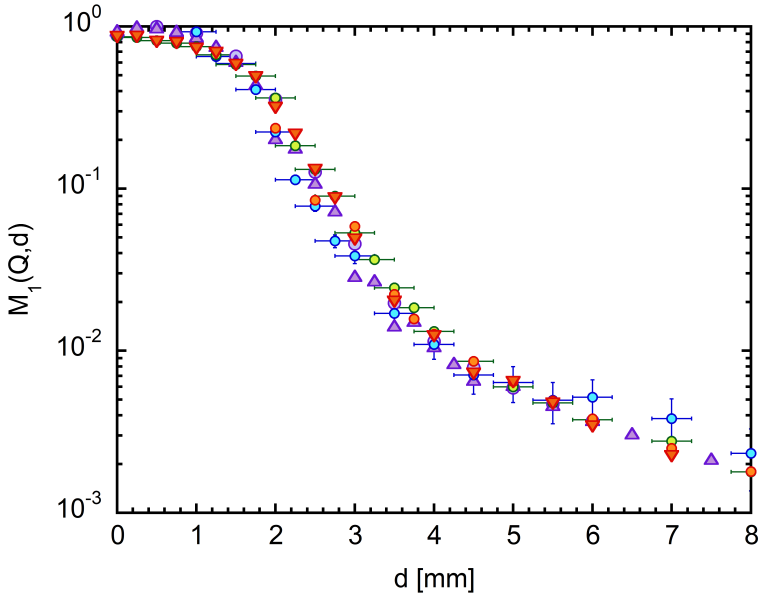


**Figure 2.9:** Mean ionization cluster size as a function the impact parameter $d$, for different radiation qualities, normalized to the value at $d = 0\,\mathrm{mm}$: 26.7-MeV $^7$Li ions (violet), and carbon ions at 240 MeV (blue), 150 MeV (green) and 96 MeV (orange). Different symbols correspond to different measuring shifts. For some of the data, uncertainties are plotted on both $M_1$ and $d$. The latter are estimated as 2/3 of the beam radius, *i.e.* $\pm 0.25\,\mathrm{mm}$.

shown in Figure 2.8(a).

The shape of the curve does not change with the type of primary particle or its velocity, however, the probability of measuring a cluster size greater than 0 is higher for ions with higher primary ionization density, due to the higher number of secondary electrons set in motion along a relevant track length. This suggests therefore a scaling on $D/\lambda_{\mathrm{ion}}$, which is presented in Figure 2.8(b): the probability of cluster sizes greater than zero is directly proportional to the mean number of primary ionizations along a relevant track segment.

The probability of a delta electron to enter the sensitive volume depends therefore critically on both impact parameter (scaling as $(d/D)^{-2.55}$) and radiation quality (scaling with $D/\lambda_{\mathrm{ion}}$). However, if the electron indeed enters the sensitive volume, the probability of occurrence of a given ionization cluster is independent of these parameters. Similar results on the independence of the shape of the $P_\nu$ distribution in the penumbra region from impact parameters and radiation quality were obtained with ion-counting nanodosimeters (Hilgers, 2017; Bashkirov, 2009).

For each impact parameter, the mean value $M_1$ of the ionization cluster size distributions also scales with the average number of primary ionizations $D/\lambda_{\mathrm{ion}}$. Its dependence on the impact parameter $d$ is instead shown in Figure 2.9: it shows a nearly constant value in the track-core region and a marked decrease when the primary beam begins to exit from the sensitive volume. For large impact parameters, *i.e.* from about 4 mm, the steepness of this decrease is reduced and the values of $M_1$ scale approximately with the solid angle under which the sensitive volume is seen from the primary particle, *i.e.* roughly as $1/d^2$.

## 2.4 Monte Carlo study of particle tracks

Monte Carlo methods are intrinsically suited to solve the problem of radiation transport and degradation inside a medium, due to their stochastic nature and lower need for simplifying assumptions as compared to analytical calculations. For macroscopic target volumes, the *condensed history* approach (Berger, 1963) is usually applied in order to obtain a sufficient level of accuracy in the description of the physical processes with reasonable computing times. However, this approach is inadequate for nanodosimetry: a step-by-step simulation of all the interactions is required for a detailed study of particle track structure.

To address this aim, many track structure codes have been developed (see (Nikjoo, 2006) for a detailed list). These codes model explicitly all collisions of the primary particle and the secondary electrons down to an energy of about 10 eV for electrons and around 0.3 MeV/u for ions. Apart from the physical track structure description, some of these codes also extend their modelling capability to the chemical diffusion of radicals and DNA damage, for instance GEANT4-DNA (Incerti, 2010b; Bernal, 2015), PARTRAC (Friedland, 2011) and KURBUC (Uehara, 1993).

The main disadvantage of these codes is that they include cross section for either water vapour or liquid water only, and the simulations cannot be directly compared to experimental data. In order to overcome this problem, a home-made code, called *MC-Startrack*, was developed by Grosswendt (Grosswendt, 2002a) to simulate the physics of the Startrack counter. It includes cross section databases for propane, nitrogen and carbon dioxide, which allow to simulate both pure propane and propane-based tissue-equivalent mixtures. Its main features and its validation against experimental data are described in the following.

### 2.4.1 The *MC-Startrack* code

The *MC-Startrack* code can simulate the track structure of electrons and light ions in an energy range of 10 eV to 100 keV and 0.1 MeV/u to 100 MeV/u, respectively. It is based on three main assumptions:

- A light ion travels along straight lines in the medium without changing its nature: *i.e.*, elastic scattering and nuclear collisions are neglected for short track segments;
- Energy transfers to the medium due to excitations and ionizations do not appreciably change the primary particle energy;
- Charge-changing processes can be neglected; electron pick-up is taken into account by means of an effective charge state, which depends on the ion velocity.

The simulation of the primary particle track is therefore reduced to that of its ionizing interactions, while the transport and degradation of secondary electrons is simulated in detail.

The calculation of the total ionization cross section for the primary particle and the single-differential one with respect to energy can be based on two different models, the Hansen-Kocbach-Stolterfoht (HKS) model (ICRU, 1996) or the one by Rudd (Rudd, 1992). The HKS model is based on an impact-parameter dependent semi-classical calculation

for each electron shell of the target molecule; the electrons are treated independently assuming a screened hydrogen-like wave function. The total cross section is then obtained by summing on the contribution from all shells.

The Rudd model is a semi-empirical parametrization based on the molecular promotion model at low energies and on the classical binary encounter approximation at higher energies, corrected to agree with the Bethe theory of ionization (Rudd, 1988). Since the model was originally developed only for proton impact, the cross section for a different ion of charge state $Z$ and kinetic energy $E/m$ is derived by scaling the proton cross section at the same specific energy by $Z^2$. In both cases, the secondary electron spectrum is assumed to be independent of $Z$. For the specific case of propane, since no set of parameters was derived in the original work by Rudd *et al.* (Rudd, 1992), the cross sections were derived from those for methane by scaling on the ratio of the number of valence-shell electrons for both molecules, as proposed by Wilson and Toburen (Wilson, 1975).

To determine the polar emission angle of the ejected electron, the double-differential cross section provided by the HKS model is used. Since the track is assumed to have cylindrical symmetry, the azimuthal angle is assumed to be uniformly distributed between 0 and $2\pi$.

For what concerns the transport and degradation of secondary electrons, elastic scattering, ionization and excitation processes are taken into account. The total cross section (which determines the mean free path) is then given by the sum of the partial cross sections for each of these processes, grouping under the label of "excitations" all non-ionizing processes. Since the medium is assumed to be homogeneous and unpolarised, the electrons are assumed to travel along straight lines between one interaction and the next. The electrons are transported as long as their energy exceeds 10 eV, a value somewhat lower than the ionization threshold, which is 11.1 eV for propane, 15.6 eV for nitrogen and 10.9 eV for liquid water. When their energy becomes less than 10 eV, the transport is stopped and the residual energy is assumed to be deposited locally.

Elastic scattering is treated by using the Rutherford differential cross section $\mathrm{d}\sigma_{\mathrm{el}}/\,\mathrm{d}\Omega$ with respect to angle, modified to take atomic screening into account. Its integration on the solid angle therefore gives the total elastic scattering cross section as a function of the incident electron energy. However, both the differential and the total cross sections depend on the atomic screening parameter $\eta$, which is affected by large uncertainties at low energies. An additional fitting of experimental data with a correction factor at energies below 30 eV was therefore used to obtain a third functional dependence for the total elastic scattering cross section $\sigma_{\mathrm{el}}$; in this way $\mathrm{d}\sigma_{\mathrm{el}}/\,\mathrm{d}\Omega$, $\sigma_{\mathrm{el}}$ and $\eta$ can be determined as a function of the incident electron energy. The azimuthal angle is again assumed to be uniformly distributed between 0 and $2\pi$.

Excitation processes are treated differently for different target media. For nitrogen and carbon dioxide, two different functional forms are considered, one for allowed transitions and Rydberg states, and another for forbidden transitions (Grosswendt, 2000). The parameters from which the cross sections depend are taken from (Porter, 1976) in the case of nitrogen and from (Jackman, 1977) in the case of carbon dioxide. In the case of propane, one integrated cross section for atomic excitation is used, derived by Chouki (Chouki, 1994) from a fit on experimental data. For all three gases, cross sections for a set of vibrational excitations, molecular dissociation and electron attachment are implemented, even

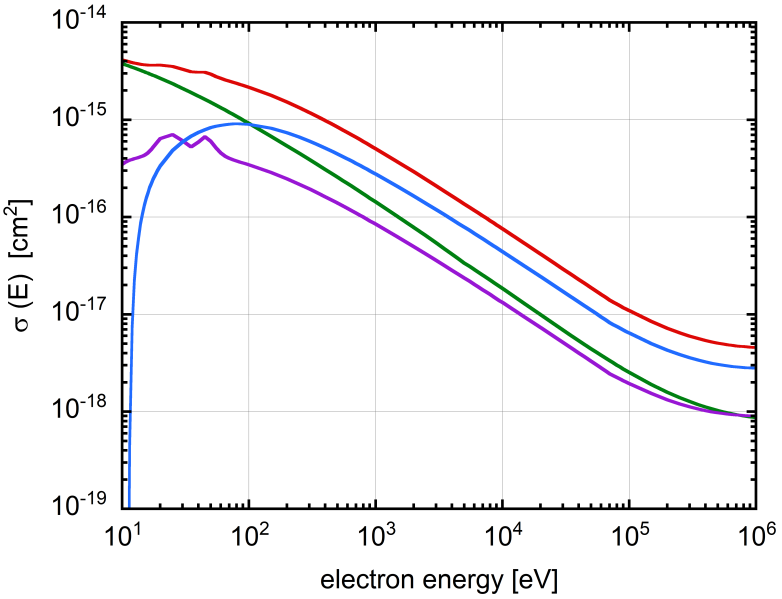


**Figure 2.10:** Electron-impact cross sections for propane implemented in the *MC-Startrack* code: total scattering cross section (red), cross section for elastic scattering (green), excitation processes (violet) and ionization (blue).

if their contribution is less relevant and can in some cases be neglected (De Nardo, 2002a). After an excitation process, the flight direction of the incident electron is assumed to be unchanged, and its energy is decreased by the amount lost to the target molecule. The excitation energy is assumed to be absorbed locally.

Both for propane and carbon dioxide, an integrated ionization cross section over all molecular subshells is considered, which is in both cases derived from (Chouki, 1994) in an analogous way as for propane excitations. For nitrogen, four different molecular subshells were considered, and for each one the cross section was derived from the binary-encounter-Bethe model (Kim, 1994) using the data of (Hwang, 1996) for the binding energies, kinetic energies and occupation numbers. The differential cross section with respect to energy was modelled by a Breit-Wigner curve, as proposed by (Green, 1972). Due to energy conservation, the maximum secondary electron energy was assumed to be $\varepsilon_{\max}(T) = \frac{1}{2}(T - I(T))$, where $T$ is the incident electron energy and $I(T)$ the ionization potential of the target molecule. The faster electron is assumed to be the primary one. The ionization potential $I(T)$ was assumed to depend on incident energy in order to take into account the contribution from inner shells; this dependence was obtained from a weighted mean of the binding energies, using the partial cross sections of each subshell (Hwang, 1996) as weighting factor.

After ionization, the polar angle of emission of the ejected electrons was calculated from the kinematic equations of Berger (Berger, 1970), including some corrections at energies lower than 200 eV to improve the agreement with experimental data; in particular, an isotropic distribution is used at energies below 50 eV. The azimuthal angles are uniformly distributed between 0 and $2\pi$, with the constraint $\varphi_2 = \pi - \varphi_1$, arising from momentum conservation.

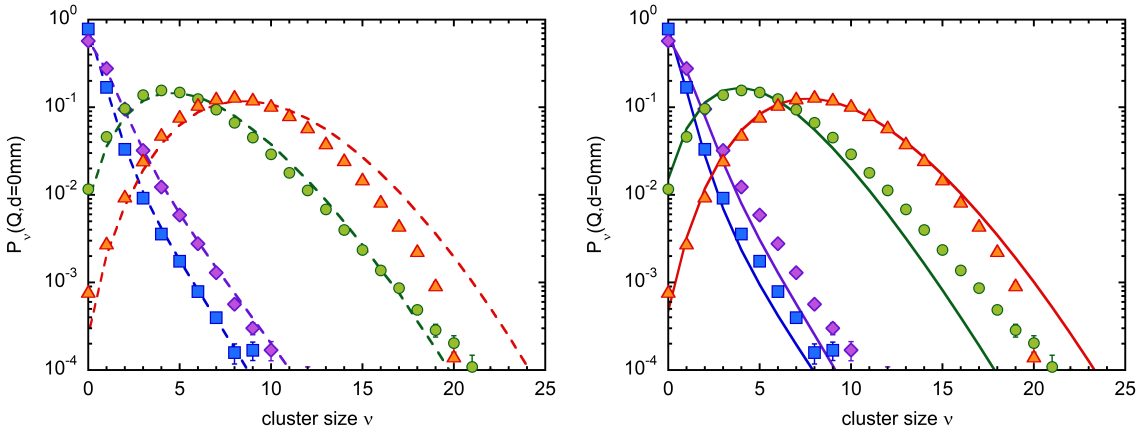


**(a)** HKS model **(b)** Rudd model

**Figure 2.11:** Comparison between experimental and simulated ionization cluster size distributions at impact parameter $d = 0\,\mathrm{mm}$ for different radiation qualities: 20-MeV protons (blue squares), 16-MeV deuterons (violet diamonds), 48-MeV $^6$Li ions (green circles) and 26.7-MeV $^7$Li ions (orange triangles). The simulations have been carried out using (a) the HKS (dashed lines) and (b) the Rudd model (continuous lines) for primary ionizations. For the experimental data, statistical uncertainties are plotted.

The trend of the electron-impact cross sections implemented in *MC-Startrack* is shown in Figure 2.10 for the case of propane. For a more detailed description of the cross section models, the reader is referred to (De Nardo, 2002a; Grosswendt, 2002b; Grosswendt, 2000).

### 2.4.2 Validation of the *MC-Startrack* code

The results of the *MC-Startrack* code were validated against the experimental ionization cluster size distributions measured with the Startrack counter, in order to assess which of the two primary ionization models, *i.e.*, the HKS or the Rudd one, leads to a better agreement with experimental nanodosimetric data (Grosswendt, 2014). To some extent, the response function of the counter was implemented in the code: in particular, the non-uniform detection efficiency, an additional amplification efficiency factor and the loss of resolution for bigger clusters due to insufficient time separation of the collected electrons were considered.

Figure 2.11 shows a comparison between some of the experimental data for impact parameter $d = 0\,\mathrm{mm}$ already presented in Figure 2.7 and Monte Carlo simulations, carried out either with the HKS or the Rudd model. For protons and deuterons, the HKS model seems to reproduce better the experimental data, however, the agreement is worse for densely ionizing particles such as low-energy $^7$Li ions. For the case of 48-MeV $^6$Li ions, both simulated distributions are slightly shifted with respect to the experimental one, the Rudd one at lower clusters and the HKS at higher ones. The agreement at high clusters is however much better with the HKS model.

If the penumbra region is considered, the agreement between measured and calculated distributions is definitely better with the Rudd model: the distributions simulated with the

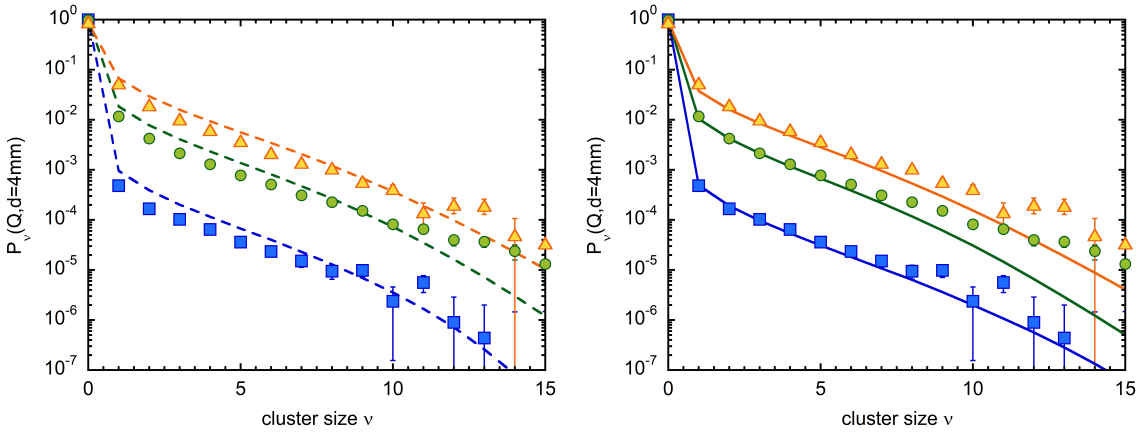


**(a)** HKS model **(b)** Rudd model

**Figure 2.12:** Comparison between experimental and simulated ionization cluster size distributions at impact parameter $d = 4\,\mathrm{mm}$ for different radiation qualities: 20-MeV protons (blue squares), 48-MeV $^{6}$Li ions (green circles) and 96 MeV carbon ions (yellow triangles). The simulations have been carried out using (a) the HKS (dashed lines) and (b) the Rudd model (continuous lines) for primary ionizations. For the experimental data, statistical uncertainties are plotted.

HKS model highly overestimate the cluster size distributions for all radiation qualities, as shown in Figure 2.12. This better agreement is related to the smaller number of secondary electrons set in motion when the Rudd model is used (Grosswendt, 2014). A similar better agreement is also found if the $M_1$ profile as a function of the impact parameter is considered.

The agreement between measured and simulated distributions is therefore better if the Rudd model is applied, in particular in the penumbra region, and for densely-ionizing particles also in the track-core. For sparsely-ionizing particles a reasonable agreement is also obtained with the Rudd model, even if not as good as with the HKS one. For these reasons, the Rudd model was used in all further simulations presented in this work, even if the HKS model has the advantage of having no adjustable parameter (as opposed to the 11 free parameters of the Rudd model) and being directly applicable to all ion types.

## 2.5 Stochastics of the ionization yield in different materials

Since the ionization cross section and particle transport properties depend on target material, it can be expected that the ionization yield in nanometric target volumes will change if different target materials are considered. This is not a problem for a computational study of track structure, as long as a database of relevant cross sections is available for the material of interest. However, an experimental study of track structure is not feasible in all materials, especially in the condensed phase.

Due to this limitation, the question arises if the ionization yield measured or calculated in one material can be related to that in a different one, and in particular to liquid water, which is commonly assumed as a substitute for biological tissue. In order to investigate

this point, the stochastics of the ionization yield is discussed in the following in greater detail; a possible procedure to relate cluster size distributions measured or calculated in different materials is then presented.

### 2.5.1 The compound Poisson process

If a travelling length of the order of the nanometre is considered, the energy loss of the primary particle can be neglected, and a constant ionization cross section can be assumed along the particle path. Since each interaction occurs independently of the previous ones, the number of primary ionizations along such a track segment will depend only on the ratio between the considered track length $D$ and the mean free path for primary ionizations $\lambda_{\mathrm{ion}}$; in particular, it will be given by a Poisson distribution of parameter $\overline{\kappa}(Q,D) = D/\lambda_{\mathrm{ion}}$, where the overbar stresses the fact that it corresponds to the average number of primary ionizations.

If the secondary electron contribution is considered, each primary ionization can (at least in principle) give rise to a secondary electron track, and the probability distribution of the number of ionizations inside a volume of size $D$ whose centre is located at a distance $d \geq 0\,\mathrm{mm}$ from the particle track is given by a compound Poisson process (De Nardo, 2002a):

$$P_\nu(Q,d,D) = \sum_{\kappa=0}^{\infty} \frac{[\overline{\kappa}(Q,D)]^\kappa \, \mathrm{e}^{-\overline{\kappa}(Q,D)}}{\kappa!} \cdot p_\nu^{(\kappa)}(Q,d,D) \tag{2.5}$$

In the above equation, the first term in the summation is the Poisson probability of producing exactly $\kappa$ primary ionizations along the track segment, given a mean number $\overline{\kappa}$ of ionizations. The second term represents the probability that, given a number $\kappa$ of primary ionizations, a cluster size $\nu$ is produced inside the target volume. Since primary ionization events are statistically independent, this probability is given by the $\kappa$-fold convolution of the probability distribution $p_\nu^{(1)}(Q,d,D)$ for single primary ionizations ($\kappa = 1$):

$$p_\nu^{(\kappa)}(Q,d,D) = p_\nu^{(1)}(Q,d,D) * p_\nu^{(1)}(Q,d,D) * \ldots * p_\nu^{(1)}(Q,d,D) \tag{2.6}$$

The convolution operation, indicated by the asterisk, is performed $\kappa$ times ($\kappa$-fold convolution), and is defined for two discrete functions $f_\nu$ and $g_\nu$ as $(f*g)_\nu = \sum_{\mu=0}^{\nu} f_{\nu-\mu} g_\mu$.

The probability distribution $p_\nu^{(1)}(Q,d,D)$ is independent of the stochastics of primary ionizations, but depends only on the properties of secondary electron ejection and degradation in the material. Because of this, it depends only on the specific energy of the primary particle; as opposed to $\overline{\kappa}$ which depends both on its charge state and specific energy.

The moments of the $p_\nu^{(1)}(Q,d,D)$ can also be defined:

$$m_\xi = \sum_{\nu=0}^{\infty} \nu^\xi \, p_\nu^{(1)}(Q,d,D) \tag{2.7}$$

Using the formalism of characteristic functions, it can be shown (De Nardo, 2002a) that the moments $m_\xi$ are related to the moments $M_\xi$ of the full probability distribution $P_\nu(Q,d,D)$. This can be understood given the strong relation between the corresponding probability distributions implied in the compound Poisson process. In particular, the moments $m_\xi$ are

related to the cumulants[(1)] $C_\xi$ of the $P_\nu$ distribution through the mean number of primary ionizations $\overline{\kappa}(Q,D)$:

$$C_\xi(Q,d,D) = \overline{\kappa}(Q,D) \cdot m_\xi(Q,d,D) \tag{2.8}$$

Since the first cumulant is the mean value of the distribution and the second is the variance, for the specific cases of $\xi = 1$ and 2 it can be obtained that

$$\begin{aligned} M_1(Q,d,D) &= \overline{\kappa}(Q,D) \cdot m_1(Q,d,D) \\ M_2(Q,d,D) - [M_1(Q,d,D)]^2 &= \overline{\kappa}(Q,D) \cdot m_2(Q,d,D) \end{aligned} \tag{2.9}$$

The ratio of the second to the first moment of the $p_\nu^{(1)}(Q,d,D)$ distribution is therefore independent of $\overline{\kappa}(Q,D)$ and can be obtained from the ratio of the variance and the mean of the full $P_\nu(Q,d,D)$ distribution.

### 2.5.2 Material equivalence

The problem of a possible correspondence between ionization yields measured or calculated in different materials has been analysed by Grosswendt *et al.* (Grosswendt, 2004a; Grosswendt, 2004b), considering in particular the filling gases used in experimental nanodosimetry, namely propane and nitrogen, compared to liquid water. Their analysis starts from the consideration, supported by some experimental evidence (Wilson, 1975), that the energy distribution of secondary electrons depends only weakly on the chemical structure of the target molecule. This can be explained by the fact that ionizing interactions usually take place with electrons of the external molecular shells, which have a low binding energy, and the energy transfer is not limited to well-defined quanta as in the case of excitations. It should therefore be possible to derive a scaling procedure to relate ionization cluster-size distributions in different materials.

A first requirement is that the two distributions have the same mean cluster size $M_1$. Using Eq. 2.8 and the fact that $\overline{\kappa}(Q,D) = D/\lambda_{\text{ion}}$, it can be obtained in terms of mass per area:

$$(D\rho)^{\text{H}_2\text{O}} = (D\rho)^{\text{gas}} \times \frac{(\lambda\rho)_{\text{ion}}^{\text{H}_2\text{O}}}{(\lambda\rho)_{\text{ion}}^{\text{gas}}} \times \frac{m_1^{\text{gas}}(Q,d,D)}{m_1^{\text{H}_2\text{O}}(Q,d,D)} \tag{2.10}$$

where $\rho$ is the target density. Apart from a density scaling, the first fractional term is related to the ionization cross section for the primary particle and the second one to the

[(1)] The cumulants of a probability distribution can be obtained from the natural logarithm of the characteristic function $\Phi(\omega)$:

$$C_\xi = i^{-n} \frac{\mathrm{d}^{(n)} \ln[\Phi(\omega)]}{\mathrm{d}\omega}$$

This is analogous to the way the moments of the distribution can be obtained from the characteristic function itself:

$$M_\xi = i^{-n} \frac{\mathrm{d}^{(n)} \Phi(\omega)}{\mathrm{d}\omega}$$

The cumulants of a probability distribution are related to its moments and vice versa. In particular, the $n^{\text{th}}$-cumulant is an $n^{\text{th}}$-order polynomial function of the first $n$ moments. For the first two cumulants, the following relations are valid:

$$C_1 = M_1 \qquad C_2 = M_2 - M_1$$

*i.e.*, the first cumulant is the mean value of the distribution, while the second is the variance.

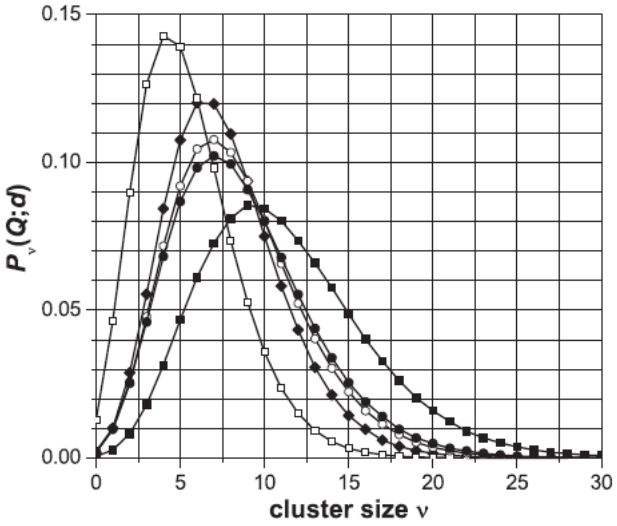


**Figure 2.13:** Comparison between cluster size distributions obtained by Monte Carlo simulations for 4.6-MeV $\alpha$ particles at an impact parameter $d = 0\,\mathrm{mm}$, with varying target sizes in different materials: $(D\rho) = 0.4\,\mu\mathrm{g/cm^2}$ in nitrogen (empty squares), propane (full squares) and liquid water (diamonds); corresponding distributions for target dimensions scaled according to Eq. 2.11: $(D\rho) = 0.578\,\mu\mathrm{g/cm^2}$ for nitrogen (empty circles), $(D\rho) = 0.321\,\mu\mathrm{g/cm^2}$ for propane (full circles). From (Grosswendt, 2004b).

transport and degradation of secondary electrons. An analogous requirement can be made for all the higher order cumulants $C_\xi$, giving rise to a set of equations identical to Eq. 2.10 apart from the substitution of $m_1$ with $m_\xi$ in the last term. An exact correspondence between target sizes in different materials seems therefore possible only if the ratio of the same-order moments of the probability distribution $p_\nu^{(1)}$ in both materials is constant.

An approximate scaling procedure can however be derived by assuming that secondary electron production and transport are similar in the two materials. In this case $m_\xi^{\mathrm{gas}} \approx m_\xi^{\mathrm{H_2O}}$, and the last term in Eq. 2.10 can be set equal to 1 for all values of $\xi$, regardless of radiation quality, target size and impact parameter. The water-equivalent size can therefore be obtained by scaling on the ratio between the mean free paths for primary ionizations in the two media:

$$(D\rho)^{\mathrm{H_2O}} = (D\rho)^{\mathrm{gas}} \, \frac{(\lambda\rho)_{\mathrm{ion}}^{\mathrm{H_2O}}}{(\lambda\rho)_{\mathrm{ion}}^{\mathrm{gas}}} \tag{2.11}$$

This scaling is in particular valid for all those cases where the secondary electron contribution is negligible (for instance, low-velocity primary particles, target crossed along its central axis and/or small target size). An example of the results of this approximate scaling procedure is reported in Figure 2.13, for cluster-size distributions obtained by Monte Carlo simulations.

The general validity of this approximate scaling procedure has been verified by Grosswendt *et al.* (Grosswendt, 2004a) for low-energy (approximately 5 MeV) $\alpha$ particles in target volumes filled with propane or nitrogen, both for central crossing of the primary beam and in the penumbra region of particle tracks. A very good agreement was found between the cluster size distributions measured and simulated in the gaseous medium and

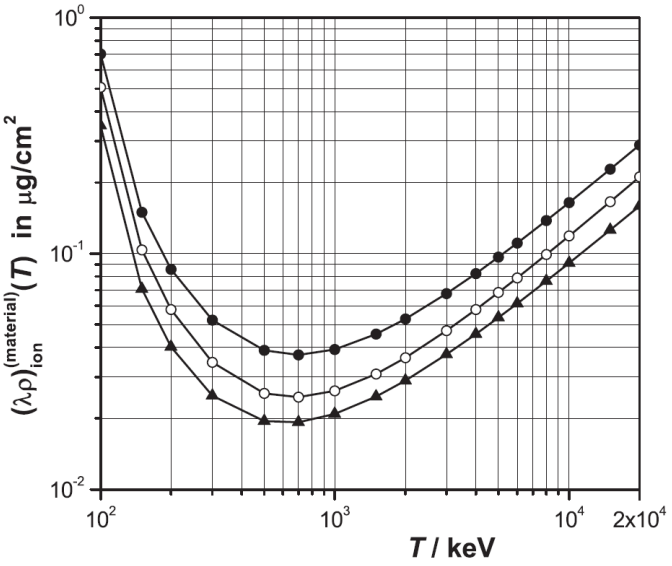


**Figure 2.14:** Mean free path for primary ionization for $\alpha$ particles as a function of the specific energy, in nitrogen (solid circles), propane (solid triangles) and liquid water (empty circles). From (Grosswendt, 2004b).

the simulated ones in liquid water, if the target sizes are scaled according to Eq. 2.11. Moreover, the trend of the mean free path for primary ionizations as a function of the specific energy is very similar in the three materials which were considered (see Figure 2.14). Their ratio depends therefore only weakly on primary particle energy, and since the ionization cross section also scales with the square of the charge state of the incident ion, a unique scaling factor can be applied for all types and energies of the primary particles. This factor is equal to 1.24 for propane and to 0.693 for nitrogen.

## 2.6 Nanodosimetric descriptors of radiation quality

As discussed in Chapter 1, LET has been traditionally used as a physical descriptor of radiation quality, even if its correlation with radiobiological effects is not straightforward. This can be traced back to two main shortcomings of LET: namely, it does not take into account the stochastic nature of particle track structure and it is not easily measurable in unknown radiation fields. On the other hand, nanodosimetric quantities derived from ionization cluster size distributions are measurable and intrinsically suited for a stochastic description of the radiation quality. They could therefore be ideal candidates for the development of a possible correlation between measurable physical quantities and radiobiological effects. The complementary cumulative distribution functions $F_k$, which represent the probability of measuring a cluster of $k$ or more electrons within the sensitive volume, are particularly suited for this purpose, since they are intuitively linked to damage complexity: if a primary particle hits a DNA strand, the degree of clustering of the initial ionization yield within nanometric distance is likely to be correlated to the probability of late damage (Goodhead, 1994).

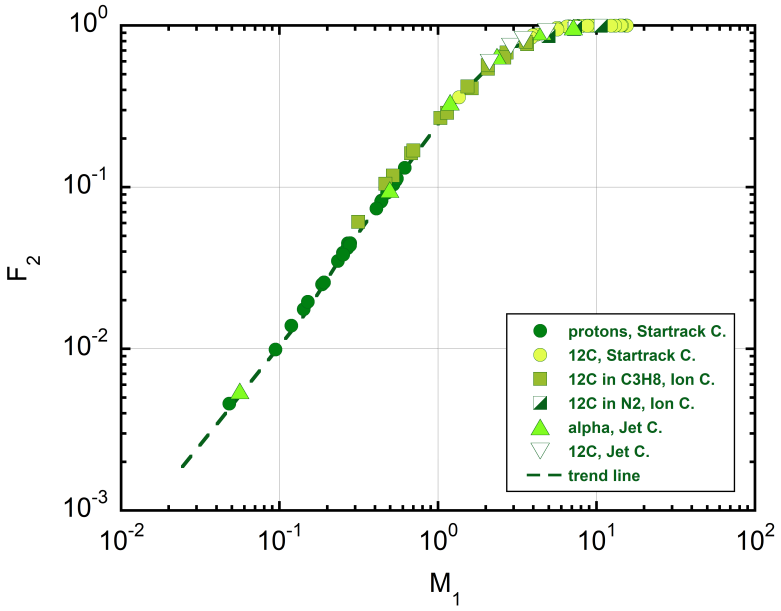


**Figure 2.15:** Synopsis of the $F_2$ values as a function of $M_1$, measured with the three nanodosimetric counters in propane and nitrogen, for different incident radiation qualities.

In the framework of the BioQuaRT[(2)] project, extensive measurement campaigns were carried out with the three nanodosimeters, in order to compare their response in various operating conditions. This comparison gave rise to a very interesting result which is shown in Figure 2.15: if the track core region is considered, the cumulative probability $F_2$ of measuring at least two ionizations in the sensitive volume describes a unique curve when plotted as a function of the mean ionization yield $M_1$, regardless of the incident radiation quality, the target size and chemical composition, the detection efficiency and in general the specific response function of each nanodosimeter, even if the ICSD will change according to these parameters.

A similar result is obtained also for $F_1$ and $F_3$, as shown in Figure 2.16 for measurements carried out with the Startrack counter: all values lie on unique curves that depend only on the $k$ value, regardless of the specific radiation quality. If the type or the energy of the primary particle is changed, the $M_1$ value will change, but the corresponding $F_k$ move along the same curves according to these unique relations. The $F_k$ values for $k = 1$, 2, and 3 are thus uniquely determined by $M_1$, regardless of the incident radiation quality and target parameters.

The behaviour of the cumulative probabilities $F_k$ can be explained starting from the compound Poisson process discussed in Section 2.5.1: considering the case of central passage and a 100% detection efficiency, if $\kappa$ primary ionizations are produced, a cluster of $\nu \geq \kappa$ ionizations will be measured by the counter. Therefore $p_\nu^{(\kappa)}(Q, D) = 0$ for $\nu < \kappa$;

[(2)] https://www.ptb.de/emrp/bioquart-home.html

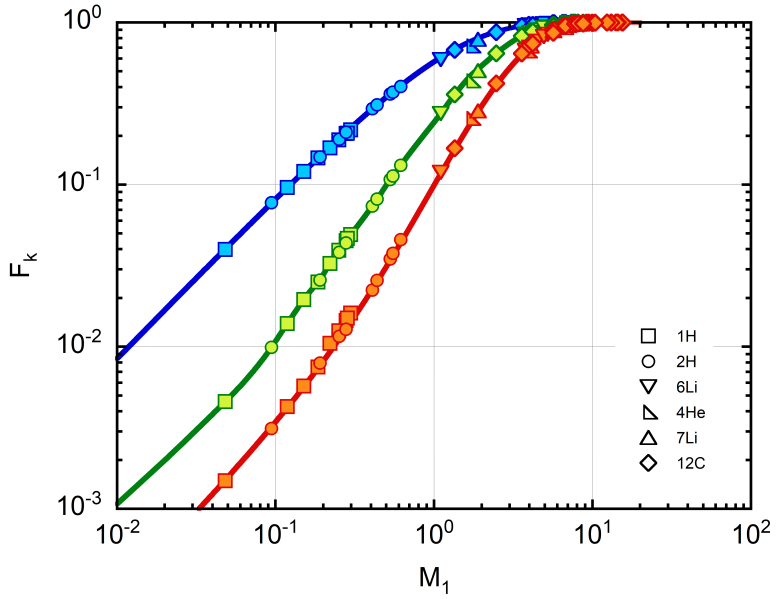


**Figure 2.16:** Complementary cumulative distributions $F_k$ for $k = 1$ (blue), $k = 2$ (green) and $k = 3$ as a function of the mean cluster size $M_1$, measured by the Startrack counter for different incident radiation qualities. Symbols correspond to experimental data, solid lines are an interpolation of the data points.

and the summation on $\kappa$ in Eq. 2.5 does not extend to infinity but is limited to $\kappa \leq \nu$:

$$P_\nu(Q,D) = \sum_{\kappa=0}^{\nu} \frac{[\overline{\kappa}(Q,D)]^\kappa \, \mathrm{e}^{-\overline{\kappa}(Q,D)}}{\kappa!} \cdot p_\nu^{(\kappa)}(Q,D) \tag{2.12}$$

The probabilities $P_0$, $P_1$ and $P_2$ can be calculated taking into account that $p_\nu^{(0)} = \delta_{0\nu}$:

$$\begin{aligned} P_0(Q,D) &= \mathrm{e}^{-\overline{\kappa}(Q,D)} \\ P_1(Q,D) &= \overline{\kappa}(Q,D)\, p_1^{(1)}(Q,D)\, \mathrm{e}^{-\overline{\kappa}(Q,D)} \\ P_2(Q,D) &= \overline{\kappa}(Q,D)\, p_2^{(1)}(Q,D)\, \mathrm{e}^{-\overline{\kappa}(Q,D)} + \frac{1}{2}\,[\overline{\kappa}(Q,D)]^2\,[p_1^{(1)}(Q,D)]^2\,\mathrm{e}^{-\overline{\kappa}(Q,D)} \end{aligned} \tag{2.13}$$

Taking into account that $M_1(Q,D) = \overline{\kappa}(Q,D)\, m_1(Q,D)$, the unique curves found for $F_1$, $F_2$ and $F_3$ confirm that the single-electron probability distribution $p_\nu^{(1)}(Q,D)$ depends only weakly on radiation quality and site size. The weak dependence on particle type and energy is more easily understandable given the similar shape of the low-energy part of the secondary electron spectrum at different specific energies of the primary ion. The weak dependence on target size $D$ is however more difficult to explain, since the site size for the three nanodosimeters differs by one order of magnitude (25 nm for the Startrack counter, $2 - 20$ nm for the Jet counter and $1 - 4$ nm for the Ion counter, depending on gas type and pressure). Part of the explanation could lie in the large fraction of secondary electrons which are emitted with an energy below the ionization threshold; however, the invariance with the site size is probably valid only for a limited range of target dimensions.

# Chapter 3

# The Startrack counter

The Startrack counter was developed with the aim of studying the ionization component of particle tracks for light ions of medical interest, in sensitive volumes about 20 nm in size. It is based on single-electron counting techniques and is installed at the Tandem-ALPI accelerator facility of INFN-LNL.

This Chapter describes in detail its structure and working principles, its response function (in particular, its efficiency and time resolution), and the data analysis procedure. Finally, the concept of "effective" target size is introduced, in order to take into account the role of the detection efficiency in the description of track structure properties.

## 3.1 The single-electron counter

The Startrack counter is installed on the +50° beam line at the Tandem-ALPI accelerator complex of Legnaro National Laboratories. This complex is composed of a two-stage Van-der-Graaff accelerator optionally followed by a superconductive resonant-cavities linear accelerator; ions from protons to gold can be accelerated up to a maximum energy of about 35 MeV times the ion charge state. For this study, the ions of interest are protons and other light ions up to carbon, which can be accelerated up to an energy of 20 MeV/u.

As discussed in Chapter 2, the design of the counter is based on the physical separation between the interaction region and the amplification one. This is done by means of an electron collector and a drift column in which the electrons diffuse so that they reach the multiplication stage well separated in time. Each recorded pulse is therefore assumed to be produced by a single primary electron, regardless of its amplitude, removing the fluctuations due to avalanche statistics.

The single-electron counter is therefore composed of four main parts:

- A sensitive volume, where the interaction of the beam with the filling gas takes place;
- An electron collector, which extracts the electrons from the sensitive volume and guides them to the transfer stage;
- A drift column, which separates in space and time the collected electrons, allowing to count them separately;
- A multi-step avalanche chamber (MSAC), which performs the amplification stage.

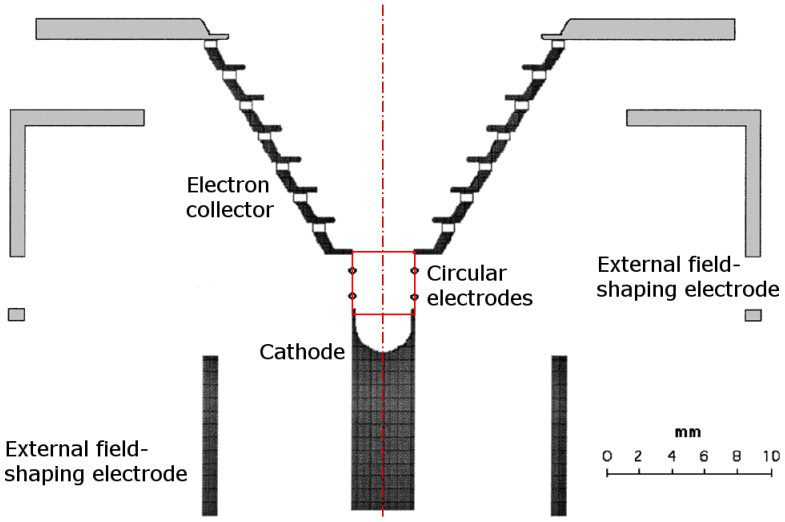


**Figure 3.1:** Details of the electrodes defining the sensitive volume and the electron collector. The top grey layer represents the base of the connector to the drift column. The thin red square shows the nominal sensitive volume 3.7 mm in diameter and height. The nominal position of the primary beam is along a diameter on its median plane. The dash-dotted line shows the axis of rotational symmetry. Modified from (De Nardo, 2002b).

Each of these four sections is described in the following.

### 3.1.1 The sensitive volume and the electron collector

The nominal sensitive volume is an almost wall-less cylinder 3.7 mm in diameter and height. Since it must be transparent to the primary beam and to fast electrons emerging from particle tracks, it has no physical boundaries (which would absorb secondary electrons and attenuate and possibly fragment the primary beam), but its border is defined by an electrostatic "wall" which keeps inside the volume the low-energy electrons generated inside it and repels the ones produced outside. This means that the electric field inside the volume must have a strong vertical component in order to suck the low-energy electrons into the collector, while outside it a strong radial component must be present in order to give rise to the repulsion effect.

A schematic cross-sectional drawing of the sensitive volume and the electron collector is shown in Figure 3.1. It can be seen that the nominal sensitive volume is defined by means of four electrodes: the cathode which defines the bottom of the cylinder, the first circular electrode of the collector which defines the upper surface, and two circular rings for the lateral one. The spacing between the two rings is equal to the one between the first ring and the collecting hole and the second ring and the cathode.

The shape of all electrodes and support structures was designed with the aim of reducing electron absorption and secondary emission from their surface as much as possible and of improving electric field uniformity in the sensitive volume area (De Nardo, 1998). In particular, the cathode has a cavity on its top face to reduce absorption of electrons which may be scattered towards it, the two rings are only 0.1 mm-thick to reduce field perturbations and the surface of the first electrode of the collector which looks towards the

sensitive volume has been reduced to a minimum. Two external field-shaping electrodes are also present in order to improve the repulsion effect of the transversal component outside the nominal volume: a cylinder coaxial to the cathode and another one around the electron collector, which has a hole to allow the passage of the ion beam. All the electrodes have rounded edges to avoid high electric fields which may cause discharges.

The electrodes are biased with negative voltages, which decrease in absolute value going from the cathode to the electron collector in order to provide the vertical component of the electric field. The exact voltage values have been chosen in order to maximise the electron collection efficiency.

The sensitive volume is joined to the drift column by means of the electron collector, which is composed of eight 1.5 mm-thick circular electrodes forming an upside-down cone, to minimize electron absorption. The electrodes are made of a conductive tissue equivalent plastic (A150) and separated by insulators. They are biased with decreasing negative voltages and form an electrostatic lens which guides the electrons to the base of the drift column. A detailed description of the design choices for the electrodes defining the sensitive volume and the collector can be found in (De Nardo,2002b; De Nardo, 1998).

As pointed out before, the physical size of the detecting volume is 3.7 mm in both diameter and height. The equivalent volume size is defined by the density of the filling gas, which varies with the type of gas and its pressure. The Startrack counter is filled with pure propane, with a pressure in the range $150 - 300$ Pa. The equivalent volume size scaled at unit density is therefore between 10 nm and 25 nm.

### 3.1.2 The drift column: drift and diffusion of the electron cluster

The electron collector is connected to the base of the drift column by means of another truncated cone, defined by six circular aluminium electrodes biased independently. Its purpose is to match the relatively strong (30 V/cm) electric field at the top of the electron collector to the much lower one of the drift column. The initial electron cluster is defocused by this electrostatic lens, which causes some electron losses on the drift column walls, which are kept to a minimum by the accurate selection of the electrodes voltages. However, this defocusing effect also improves the time resolution of the detector, due to the different length of the trajectories of the surviving electrons.

The drift column is composed by a stack of 2 mm-thick stainless steel discs, which are equally spaced at a distance of 3 mm by insulating rings and connected by a high-precision resistor chain which acts as a voltage divider. Their internal diameter is 90 mm and the total drift column length is 17 cm. A scheme of the detector showing the connector and the drift column is shown in Figure 3.2.

Inside the column, the combined effect of the low electric field and the frequent collisions with gas molecules induces a drift motion of the electron cluster superposed to a thermal diffusion both transversally and longitudinally with respect to the electric field lines. The arrival time of the electrons is Gaussian distributed, with a mean value $\bar{t} = L/v_d$ (where $L$ is the drift column length and $v_d$ is the drift velocity) and a standard deviation $\sigma_t$ which can be expresses as the ratio of the spatial dispersion $\sigma_L$ and the drift velocity $\sigma_t = \sigma_L/v_d$.

The drift velocity can be calculated considering the fact that in order to reach an equilibrium condition, in each collision with the gas molecules the electrons lose all the

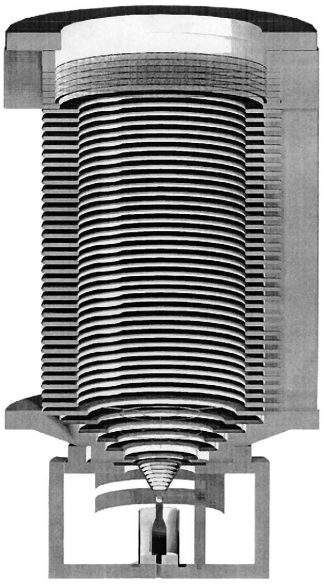

**Figure 3.2:** Details of the connector, the drift column and the multi-step avalanche chamber, showing the six connector electrodes, the rings composing the drift column and the MSAC meshes.

energy they gained between one collision and the next:

$$v_d = \frac{eE}{m}\tau = \mu^- E \tag{3.1}$$

where $e$ and $m$ are the electron charge and mass, respectively, $E$ is the value of the electric field and $\tau$ is the mean time between collisions. The factor $\mu^-$ multiplying the electric field is called *mobility* of the electrons and is inversely proportional to the gas pressure.

Assuming that all electrons start their drift and diffusion motion from the same spatial position, the spatial dispersion $\sigma_L$ of the cluster at the end of the drift column can be calculated as

$$\sigma_L = \sqrt{2D\bar{t}} = \sqrt{2D\,\frac{L}{v_d}} \tag{3.2}$$

where $D$ is the diffusion coefficient, which can be calculated from the kinetic theory of gases. However, the presence of the electric field changes the mean kinetic energy of the electrons, which cannot be expresses simply by the pure thermal limit $\varepsilon = \frac{3}{2}k_B T$. A phenomenological quantity, the so-called *characteristic energy* $\varepsilon_k$, is therefore introduced in order to take this fact into account (Peisert, 1984): for a given type of gas, it depends only on the reduced electric field $E/P$. The diffusion coefficient can then be expressed as

$$D = \frac{\varepsilon_k}{eE}\,v_d = \frac{\varepsilon_k}{e}\,\mu^- \tag{3.3}$$

and the spatial dispersion $\sigma_L$ takes the form

$$\sigma_L\left(L, \frac{E}{P}, E\right) = \sqrt{\frac{2\varepsilon_k}{e}\cdot\frac{L}{E}} = \sigma\left(\frac{E}{P}\right)\sqrt{\frac{L}{E}} \tag{3.4}$$

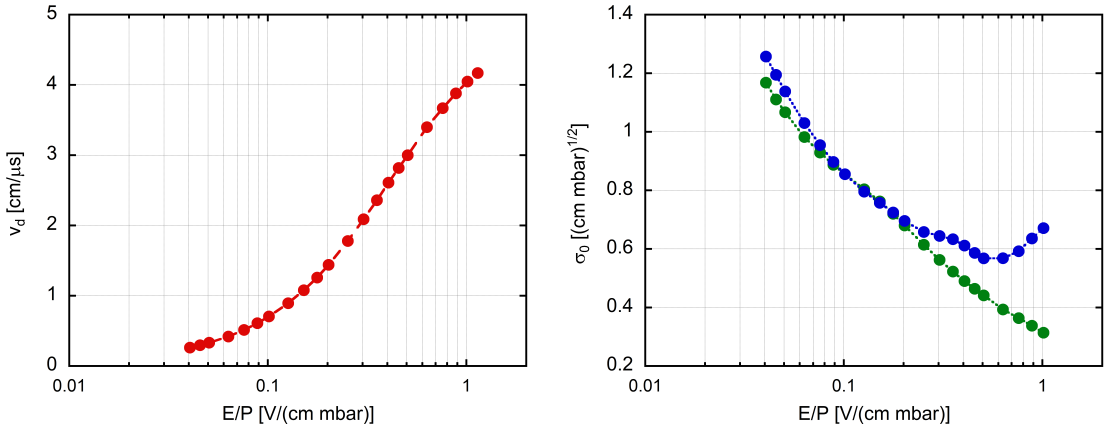


**(a)** Drift velocity **(b)** Spatial dispersion

**Figure 3.3:** (a) Drift velocity $v_d$ of electrons (red) as a function of the reduced electric field. (b) Transverse (blue) and longitudinal (green) normalized spatial dispersion $\sigma_0$ as a function of $E/P$. The increasing difference with increasing reduced electric field is visible. The data are calculated for a temperature of 20°C. Experimental data from (Schmidt, 1992).

Since the operating pressure is usually fixed by the equivalent volume size under analysis, Eq. 3.4 can be rewritten as a function of $E/P$ and $P$ instead of $E$:

$$\sigma_L\left(L, \frac{E}{P}, P\right) = \sqrt{\frac{2\varepsilon_k}{eE/P} \cdot \frac{L}{P}} = \sigma_0\left(\frac{E}{P}\right)\sqrt{\frac{L}{P}} \tag{3.5}$$

From the above equations it can be seen that both the drift velocity and the spatial dispersion depend on the reduced field value $E/P$; however, for a given $E/P$ value the spatial dispersion depends also from the absolute value of $E$ (or equivalently, of the pressure $P$). Another issue to be taken into account is that the approximation of the spatial dispersion being the same in directions parallel and orthogonal to the electric field is acceptable only if the $E/P$ value is not too high: two different diffusion coefficients $D_L$ and $D_T$ must be considered for the longitudinal and transverse directions if this is not the case.

The dependence of the drift velocity $v_d$ and of the longitudinal and transverse normalized spatial dispersion $\sigma_0$ on the reduced electric field are shown in Figure 3.3. In order to count independently each of the electrons belonging to the initial cluster, it is necessary that they arrive at the end of the drift column separated by a time interval greater that the signal formation time. From the above equations, it can be seen that this requires a small drift velocity and a large longitudinal diffusion, *i.e.*, a low reduced electric field. However, reducing $E/P$ implies also an increase in transversal diffusion, giving rise to absorption losses on the column electrodes. A good compromise could be found for values between 0.1 and 0.2 V/(cm mbar), for which the longitudinal diffusion is approximately equal to the transverse one. However, since the MSAC is a fast detector, the requirement of minimization of absorption losses is stricter than the one of sufficient time separation. The best compromise for the reduced electric field value is therefore around $0.25 - 0.3$ V/(cm mbar).

As a final remark, it should be noted that in a rigorous analysis the reduced electric field should be expressed not as $E/P$ but as $E/N$, where $N$ is the number density of the gas, *i.e.*, the number of molecules per unit volume. The latter is a quantity which is more directly related to the microscopic description of the kinetic theory, and depends on both pressure and temperature. However, $E/P$ is easier to measure, and for any given temperature value the two quantities are proportional to each other. In order to remove the effect of ambient temperature variations, temperature-controlled gauges have been used to monitor the gas pressure inside the counter.

### 3.1.3 The multi-step avalanche chamber: amplification stage

To obtain a reliable estimation of the number of electrons belonging to the initial cluster, the detector performing signal amplification must provide high gain and fast timing properties. For this reason, a multi-step avalanche chamber was selected: using more amplification stages allows to work at lower pressure, reach a higher gas gain (of the order of $10^7 - 10^8$) and at a given gain to reduce the onset of secondary avalanches. An additional advantage is that the ions produced in the ionization process are swept away very fast because of the high electric field, preventing charge build-up. These properties make the MSAC much more suited for single-electron counting than other types of single-stage proportional counters, such as parallel-plate avalanche counters or multi-wire proportional chambers (Breskin, 1984).

The multi-step avalanche chamber of the Startrack detector is composed by five stainless steel meshes separated by a 3 mm gap. The wires of the meshes have a diameter of 120 $\mu$m and a pitch of 500 $\mu$m. The signal of the chamber is read by a fast current amplifier. Since its rise time is of the order of 10 ns, two electrons separated by 20 ns or more are counted as separate.

The total gain $G$ of the MSAC is given by the product of the gains $G_i$ of each stage, multiplied by the transfer efficiency $t_{ij}$ from one stage to the next. Since in this case four stages are present, the total gain can be expressed as $G_{\text{tot}} = G_1\, t_{12}\, G_2\, t_{23}\, G_3\, t_{34}\, G_4$. It reaches a value of $2 \cdot 10^7$.

The transfer efficiency from one stage to the next depends not only on the optical transparency of the mesh, but also on the ratio of the electric field values in the stages before and after each mesh. In particular, an efficient transfer from a stage with high electric field to another with a lower one can only take place if the initial avalanche has a lateral spread greater than the pitch of the wires: this can be understood given the shape of the electric field lines, most of which end on the wire surface in this case.

The development of the avalanche inside the detector can be described by the so-called *first Townsend coefficient* $\alpha$, defined as the number of secondary electrons produced by a single primary one per unit path length along the direction of the electric field. The increase $\mathrm{d}n$ of the number $n$ of electrons in the avalanche along the path length $\mathrm{d}x$ can then be expressed as:

$$\mathrm{d}n(x) = \alpha(x)\, n(x)\, \mathrm{d}x \tag{3.6}$$

The integration of this expression along a path from one electrode to the following one gives the total gain of a single stage, which corresponds to the ratio between the final and

the initial number of electrons:

$$\ln G = \int_{x_i}^{x_f} \alpha(x)\,\mathrm{d}x \tag{3.7}$$

It is usually assumed that the Townsend coefficient $\alpha$ is a function of the reduced electric field $E/N$ only; however, various functional forms for this dependence exist (Aoyama,1985). Townsend proposed the following relation for the case of uniform electric field (Mitev, 2005):

$$\frac{\alpha}{N} = A\mathrm{e}^{-\frac{B}{E/N}} \tag{3.8}$$

where $A$ and $B$ are gas-dependent parameters. This expression has been experimentally verified for parallel-plate geometries and moderate electric field strengths. However, it was shown (Mitev, 2005) that if the electric field is not uniform $\alpha/N$ is not a unique function of $E/N$, but depends also on the gradient of the electric field and on the geometry of the detector in use. This dependence arises from the presence of non-equilibrium[(1)] between the electron swarm and the electric field; on the contrary, in the equilibrium case $\alpha/N$ is a function of $E/N$ only. In any case, for a complete characterization of the avalanche process a microscopic description by means of the Boltzmann equation must be used: for the equilibrium case, this can be done by iterative numerical methods, while Monte Carlo techniques are needed for non-equilibrium ones (Mitev, 2005).

The Townsend coefficient $\alpha/N$ and the gain $G$ are non-stochastic magnitudes which describe the mean value of the pulse-height spectrum. However, the avalanche process is intrinsically a stochastic one, and large fluctuation in the number of final electrons can take place. Various theoretical analyses have been carried out in order to understand the shape of the pulse-height spectrum originated by single-electron avalanches in proportional counters. The first one was carried out by Snyder (Snyder, 1947), who based the analysis on the assumption that the ionization probability for each electron depends only on the electric field value, regardless of the distance between one collision and the next: in other words, the ionization probability does not depend on electron energy. With this assumption, if the average gain is sufficiently high ($G > 100$), an exponential distribution for the pulse-height spectrum is obtained.

In practical cases, however, an exponential pulse-height spectrum is observed only for low and uniform electric fields (Alkhazov, 1970). This can be explained by the fact that the electrons lose nearly all their energy in collisions with the gas molecules, and they need to travel some distance in order to gain enough energy before another ionizing collision can take place. This distance is equal to $I/E$, where $I$ is the ionization potential of the gas molecule and $E$ the value of the electric field. Therefore, a constant ionization probability makes sense only if the mean free path for ionizing collisions $\lambda_{\mathrm{ion}}$ is much greater than $I/E$: in this case, the electrons reach an equilibrium distribution by means of non-ionizing collisions before further ionizations can take place.

If this assumption is not valid and $\lambda_{\mathrm{ion}} \approx I/E$, the pulse-height spectrum has a definite maximum and a lower variance. In this case, the ionization probability depends not only

[(1)] The term *equilibrium* describes a situation in which the distribution function of the electrons belonging to the avalanche does not depend on spatial position. This requires the presence of a uniform electric field (Mitev, 2005).

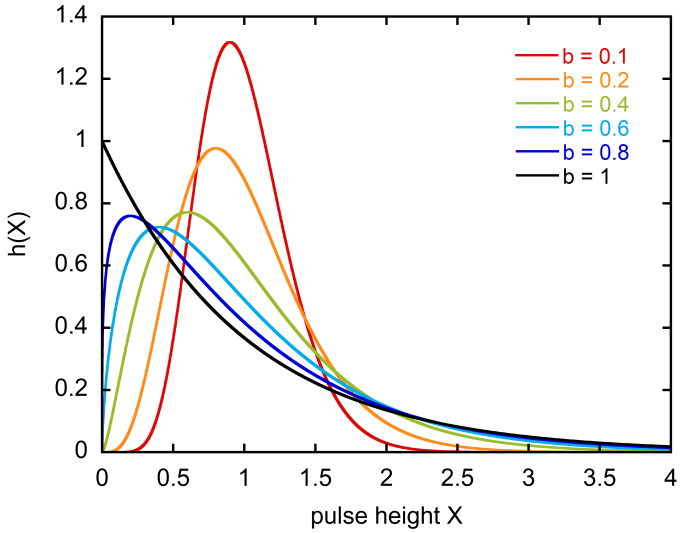


**Figure 3.4:** Examples of normalized Polya distributions with mean value $X_m = 1$ and different variance $b$. Modified from (Ferretti, 2006).

on the strength of the electric field, but also on the previous interactions undergone by the electron. In particular, by assuming that the probability of further ionizations depends on the number of electrons already present in the avalanche, a Polya distribution is obtained (Byrne, 1969; Alkhazov, 1970):

$$h(X) = C \left( \frac{X}{X_m\, b} \right)^{\frac{1}{b}-1} \mathrm{e}^{-\frac{X}{X_m\, b}} \tag{3.9}$$

$X_m$ is the mean value of the distribution (*i.e.*, the average pulse height), $b$ is the variance and $C$ is a normalization constant, equal to $1/(b\,\Gamma(1/b))$ (where $\Gamma(x)$ represents the Gamma function). No definite theoretical framework exists to predict the value of the parameter $b$ in different configurations, and its determination is carried out experimentally. Some examples of Polya distribution with $X_m = 1$ and different values of $b$ are shown in Figure 3.4: it can be noted that for $b = 1$ an exponential distribution is obtained.

In conditions of high gain and low pressure, secondary electron avalanches can occur in the detector, giving rise to spurious signals. In particular, two different mechanisms can trigger this process: UV emission by excited gas molecules and ion neutralization at the cathode. In both cases, the secondary emission occurs at the electrodes unless the gas is a mixture of components with different ionization potentials, since these UV photons are produced by excitation processes in the gas molecules and have an energy lower than the ionization threshold. In particular, electrons can be extracted by photoelectric processes or by the energy liberated when an ion reaches the cathode and is neutralized: the latter process has however a low efficiency since this energy can be dissipated by other processes in the cathode itself. An additional advantage of a multi-step amplification detector is that secondary emission is relevant only if it happens in the first stage: in all other cases, the electrons do not go through the full amplification process and the resulting lower signal

can be more easily discriminated by the electronic chain.

Extensive studies have been carried out on the probability of secondary avalanches in the MSAC of the Startrack detector (De Nardo, 1995; Dalla Pellegrina, 1998). They pointed out the fact that at a given pressure value secondary emission increases with increasing amplification, and it is higher the lower the pressure. This gives rise to a limit to the maximum gain: for pure propane, the gain must be kept to values around $10^7$ for the probability of secondary avalanches to be less than 3% (De Nardo, 1995). Concerning this, the possibility to introduce a *transfer region* (*i.e.*, a region with low electric field and no multiplication) has also been studied; the purpose was to increase the lateral spread of the avalanche due to diffusion, reducing space charge and increasing the maximum gain. However, this possibility was later discarded, due to the superior performance of a four-stage amplification configuration in terms of timing properties (Dalla Pellegrina, 1998).

A final consideration should be done about the neutralization of ions produced in the avalanche process, which can either dissociate in smaller molecules or form larger ones. These by-products can be deposited on the wires (in particular the larger ones) and lead to a degradation of the performance (*ageing*). This is particularly critical for the case of organic gases, which can form $(CH_2)_n$ polymers. To minimize these effects, materials with high chemical affinity to these type of ions must be avoided. Moreover, the gas must be kept as pure as possible, and wires with large diameter must be used in order to reduce the electric field in their immediate neighbourhood.

## 3.2 The measuring setup

The counter previously described is inserted in a vacuum chamber, which ensures the stability of the working pressure and the purity of the gas by means of a gas-flow system. This chamber also contains the trigger detector and a $^{244}$Cm $\alpha$ calibration source. Another vacuum chamber is located before the one which contains the detector, and houses the beam diagnostics. The two chambers are separated by a Mylar window 1.5 $\mu$m thick, allowing the passage of the primary beam. A photo of the measuring chambers is shown in Figure 3.5.

For a complete collection of the electron cluster produced by a primary particle, about 20 $\mu$s are necessary. To minimize pile-up effects, the counting rate of the detector must be kept below 1 kHz, while the minimum beam current produced by the Tandem accelerator is about 1 nA ($10^9$ particles per second). The primary beam is therefore defocused by means of the quadrupole magnets of the beam line, in order to lower further its intensity. However, this gives rise to a divergent beam, which must be cleaned before reaching the counter.

The arrangement of the measuring setup is shown in Figure 3.6. The first chamber is kept in vacuum, at a pressure of about $10^{-4}$ Pa, and houses two niobium collimators and two different detectors which can be alternatively moved into the beam path, by means of step motors. The first is a Faraday cup, which can measure up to a beam intensity of 1 MHz. For lower intensities, the second beam monitor is used, which is a stack of two micro-channel plates (MCP), able to measure the 2D profile of the beam in order to verify its centring and uniformity. The two MCPs are connected in series in order to reach a gain of $10^8$. The spatial resolution is given by the area of the reading anode pads which is 1 mm$^2$; the pads are read sequentially and the charge signal of each one is integrated for

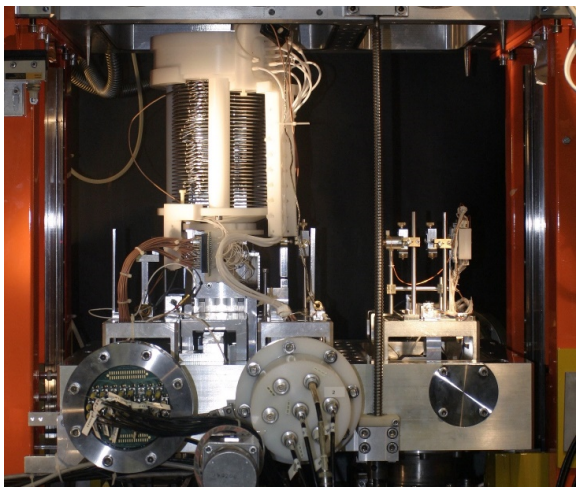

**Figure 3.5:** Photo of the Startrack apparatus: on the left side, the measuring chamber in which the drift column and the MSAC of the counter are visible. On the right side, the beam diagnostic chamber with two collimators, the micro-channel plates and the Faraday cup.

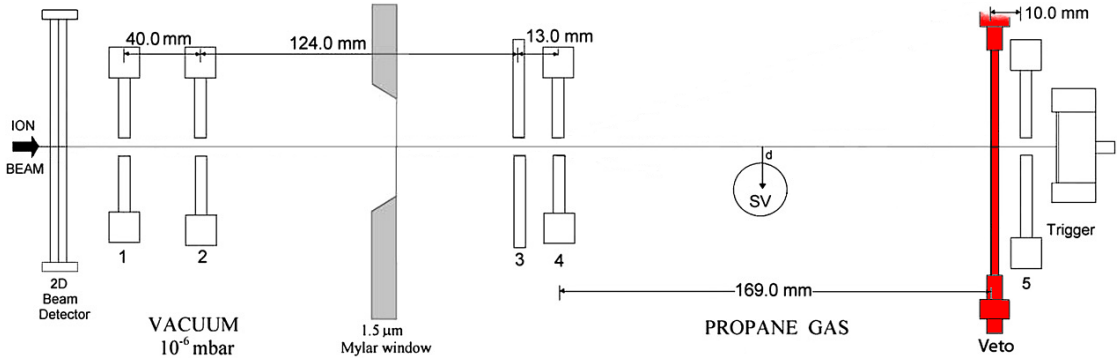


**Figure 3.6:** Graphical representation of the arrangement of beam monitors and shapers along the nominal beam path. Numbers from 1 to 5 represent the different collimators; SV is the nominal sensitive volume. The Veto detector (shown in red) has been removed from the beam line. Figure modified from (Conte, 2010).

1 ms before being processed by the electronic chain. For their operation, the MCPs require a high vacuum level of about $10^{-4}$ Pa. That is the reason why the diagnostic chamber must be kept in vacuum.

The second chamber houses the single-electron counter, the trigger detector, additional collimators and the alpha calibration source. Both the counter and the alpha source can be moved orthogonally to the nominal beam axis by means of step motors, up to a maximum distance of 10 mm from it, with a position accuracy better than 0.1 mm. Behind the last collimator, the beam diameter is 0.8 mm. The trigger is a solid state silicon detector, which is quite fast (signal formation time of about 10 ns) and has a very high efficiency for the detection of positive ions. It is reverse biased at $-50$ V, and the thickness of the depletion region is 100 $\mu$m. To reduce further pile-up effects, an additional silicon detector with a large active area (shown in red in Figure 3.6) was used as veto. This option was later

discarded because it was shown that the rejection procedure did not change significantly the resulting cluster-size distributions.

The measuring chamber is filled with propane at a pressure between 150 and 300 Pa. This gas was chosen because it allows to reach higher gas gains while keeping the probability of secondary emission to reasonable values (3%); moreover, it ensures a wide lateral spread of the avalanche (Breskin, 1983). Tests were carried out also with tissue equivalent propane (propane-TE) and dimethyl ether, which is also almost tissue equivalent (Dalla Pellegrina, 1998; De Nardo, 1995). However, in propane-TE the onset of secondary avalanches started already at a gain of $10^6$, probably because of the presence of nitrogen (De Nardo, 1995) which has a high cross section for the production of UV photons. Dimethyl ether was selected because it is a low diffusion gas, which allows a better definition of the sensitive volume; however, secondary emission has found to be too high also at the lowest gains (Dalla Pellegrina, 1998). Methane and methane-TE were discarded because of their low self-absorption of UV light, leading again to secondary avalanches (De Nardo, 1998). Instead, bigger polyatomic molecules like propane are more efficient in absorbing photons, and allow the dissipation of excess energy in collisions or dissociations.

In order to ensure the purity of the gas and the stability of detector gain over time, fresh propane is continuously flowed in the measuring chamber, at a flow rate of 1.8 sccm[(2)]. The fresh gas is inserted near the MSAC, which is the most critical region due to the gas degradation induced by the avalanche. A feedback pumping system maintains the pressure constant inside the measuring chamber, by means of an electric valve controlled by a pressure gauge. An additional line allows to flow argon inside the chambers before opening the vacuum vessel, in order to minimize adsorption of ambient electronegative gases by the walls.

## 3.3 Detection efficiency and time resolution

The total counting efficiency of the Startrack counter is the product of three factors: the collection efficiency of low-energy electrons in the sensitive volume, the transfer efficiency in the drift column (*i.e.* the fraction of electrons which are not absorbed by its electrodes) and the multiplication efficiency of the multi-step avalanche chamber, *i.e.*, the fraction of incoming electrons which give rise to detectable pulses (assuming a constant gas gain). In short, $\varepsilon_{\mathrm{tot}} = \varepsilon_{\mathrm{SV}} \cdot \varepsilon_{\mathrm{drift}} \cdot \varepsilon_{\mathrm{MSAC}}$.

The amplification efficiency of the MSAC can be estimated by fitting the single-electron gain distribution with a Polya function and calculating the percentage of counts above the experimental threshold, as described by (Ferretti, 2006). The efficiency estimated with this procedure is usually between 80% and 90%, but depends of course both on the reduced electric field in the MSAC stages and on the noise level.

The collection efficiency inside the sensitive volume depends on the actual point of production of the electron, *i.e.* on the local reduced electric field and its gradient; but also on the absolute gas pressure. The spatial dependence of the product $\varepsilon_{\mathrm{SV}} \cdot \varepsilon_{\mathrm{drift}}$ was calculated by means of a dedicated Monte Carlo code, simulating microscopically the electron transport from the point of production to the first mesh of the MSAC, taking into account

[(2)] The Standard Cubic Centimetre per Minute (sccm) is a unit of measurement for the mass flow, and corresponds to a flow of $1.67 \cdot 10^{-2}\,\mathrm{cm}^3/\mathrm{s}$ of a gas at standard temperature and pressure (101 325 Pa, 0°C).

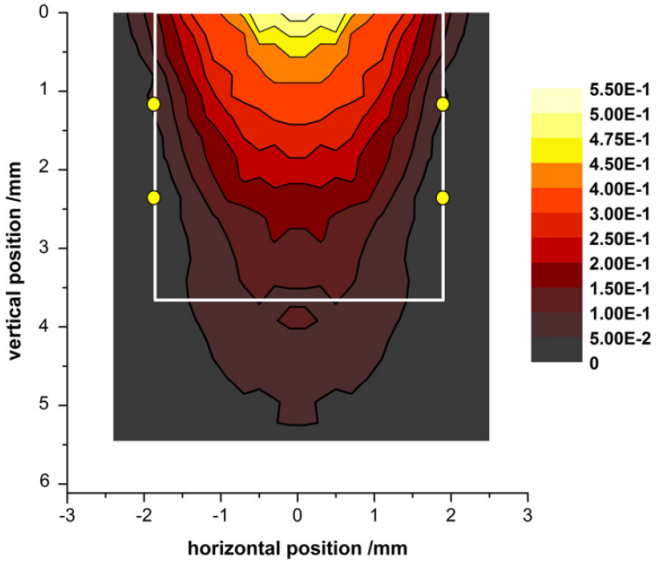


**Figure 3.7:** Colour-coded plot of the efficiency map $\varepsilon_{\mathrm{SV}} \cdot \varepsilon_{\mathrm{drift}}$ at a gas pressure of 300 Pa and a temperaure of 20°C. The white square represents the nominal sensitive volume; the four yellow circles show the position of the two ring electrodes that help to define the sensitive volume wall. Figure taken from (Conte, 2012).

non-equilibrium phenomena (De Nardo, 2002b). Figure 3.7 shows the resulting efficiency map for the standard gas pressure of 300 Pa: it can be seen that the efficiency has a radial symmetry and is of course higher for electrons produced near the collector, decreasing strongly while going towards the cathode. For a given vertical position, the efficiency is higher on the central axis, reaching a maximum value of 60% at the centre of the collector hole. The selectivity of the sensitive volume electrostatic wall was also calculated: it was found that about 90% of the collected electrons are originated within the nominal sensitive volume, while only 10% from outside (De Nardo, 2002b).

At a gas pressure of 300 Pa, the average value of the product $\varepsilon_{\mathrm{SV}} \cdot \varepsilon_{\mathrm{drift}}$ is 23%; the total detection efficiency is therefore about 20%. Since the interaction mean free paths scale with the gas pressure, it is expected that the shape of the efficiency map is maintained if the pressure is changed, and the absolute efficiency values are only scaled by a constant factor. This point will be further discussed in Chapter 4.

To check the consistency of the efficiency map, measurements of the efficiency inside the sensitive volume were also carried out, by adding a contaminant with low ionization potential inside the gas and scanning the volume with a laser. Even if the experimental data were found to be higher than the results of corresponding Monte Carlo calculations, they suggest that the shape of the efficiency map is realistic (De Nardo, 2002b).

The response function of the Startrack counter depends not only on its collection efficiency for a single electron, but also on the size of the cluster. This is because for big clusters the probability increases that two electrons reach the MSAC separated by less than 20 ns, giving rise to overlapping signals. This probability can be calculated by numerical methods (Grosswendt, priv. comm.), taking into account the Gaussian arrival time

distribution of the electrons $G(t)$ and the width of the single impulse $\Delta t$:

$$\eta_2 = \int_0^{\Delta t} \mathrm{d}t\, G(t) \int_t^{t+\Delta t} \mathrm{d}t'\, G(t') \tag{3.10}$$

where $t \in [0, \Delta T]$ is the arrival time of the first electron and $t' \in [t, t + \Delta t]$ is the arrival time of the second one. This equation assumes that the distribution $G(t)$ is truncated and renormalized in the time window $[0, \Delta T]$ in which the acquisition is active after each trigger signal. The probability for the two electrons to be counted separately is therefore $1 - \eta_2$.

If a cluster of $\mu$ electrons is considered, the probability that the time distance between two successive electrons is greater than $\Delta t$ is again $1-\eta_2$. The probability to count them as $\mu$ separate pulses is therefore given by $(1-\eta_2)^{\mu-1}$; while the probability to count them all as a single pulse is $(\eta_2)^{\mu-1}$. The probability of counting $\nu$ electrons out of an initial number of $\mu$ is therefore described by the binomial distribution $B(N, k)$, with parameters $N = \mu - 1$ (corresponding to the total number of time intervals) and $k = \mu - \nu$ (corresponding to the number of time intervals which are smaller than $\Delta t$, *i.e.*, the number of undetected electrons):

$$\varepsilon_{\nu,\mu} = \binom{\mu-1}{\mu-\nu} (\eta_2)^{\mu-\nu} (1-\eta_2)^{\nu-1} \tag{3.11}$$

A matrix can therefore be built, describing the probability of counting $\nu$ electrons from an initial number of $\mu$:

$$E_{\nu,\mu} = \begin{pmatrix} 1 & 0 & 0 & 0 & 0 & \dots \\ 0 & 1 & \varepsilon_{1,2} & \varepsilon_{1,3} & \varepsilon_{1,4} & \dots \\ 0 & 0 & 0 & \varepsilon_{2,3} & \varepsilon_{3,4} & \dots \\ 0 & 0 & 0 & 0 & \varepsilon_{4,4} & \dots \\ \vdots & \vdots & \vdots & \vdots & \vdots & \ddots \end{pmatrix} \tag{3.12}$$

$\nu$ is the row index in the matrix, while $\mu$ is the column index. Due to its definition as a probability, a normalization condition on each column applies: $\sum_{\nu=0}^{\mu} \varepsilon_{\nu,\mu} = 1$. Since the counting of zero electrons is possible only if the initial cluster size is zero, $\varepsilon_{0,\mu} = \delta_{0\mu}$.

The measured cluster size distribution $P_\nu$ is the result of the multiplication of matrix $E_{\nu,\mu}$ and the distribution $P_\mu$ which corresponds to the ideal case of infinite time resolution:

$$P_\nu = \sum_{\mu=0}^{\infty} E_{\nu,\mu}\, P_\mu \tag{3.13}$$

This equation is usually applied to cluster size distribution obtained by Monte Carlo simulation in order to compare them with the experimental ones. It has been seen that the change is relevant for cluster sizes greater than 15; however, a dependence of this value on the gas pressure is expected due to the variation of the longitudinal diffusion.

## 3.4 Data analysis procedure

After each trigger signal, a PCI analogue to digital acquisition board acquires a waveform of 16 $\mu$s in length at a rate of $5 \cdot 10^8\,\mathrm{s}^{-1}$ (500 MHz), which is then stored for off-line processing.

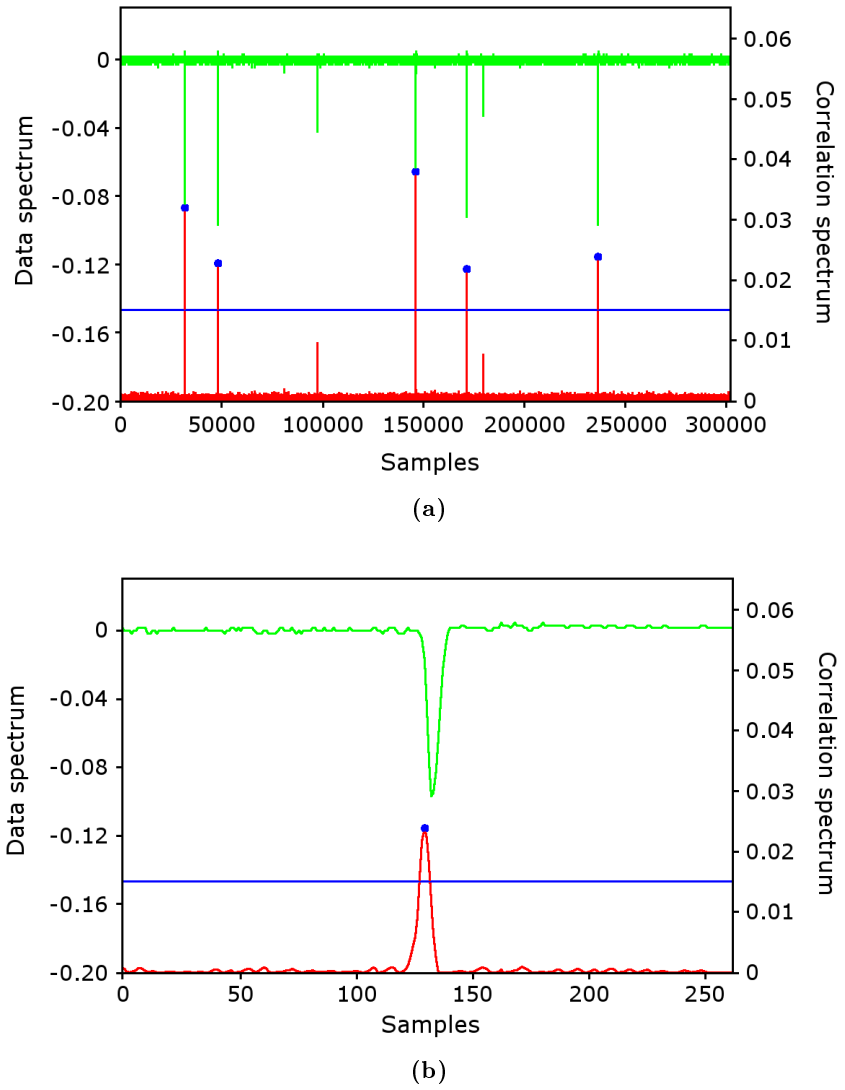


**Figure 3.8:** Example of waveforms sampled by the acquisition system (green) and the corresponding correlation spectrum (red). The blue line represents the selected threshold level, each blue dot an accepted pulse. (a) Complete waveform, (b) zoom on a single pulse.

Each waveform correspond therefore to one primary particle. To enhance the signal-to-noise ratio and help discriminating pulses in rapid succession, correlation techniques are applied to the acquired spectrum: in particular, the correlation function between the measured waveform and a test impulse selected from the real measured ones is calculated by means of a dedicated software. From this correlation spectrum of each waveform, the number of peaks above a pre-defined threshold is computed and stored in a file for further analysis, together with the height and arrival time of each pulse. An example of a raw waveform and the corresponding correlation one is reported in Figure 3.8.

The following analysis steps are shown in Figure 3.9: firstly, the time and gain dis-

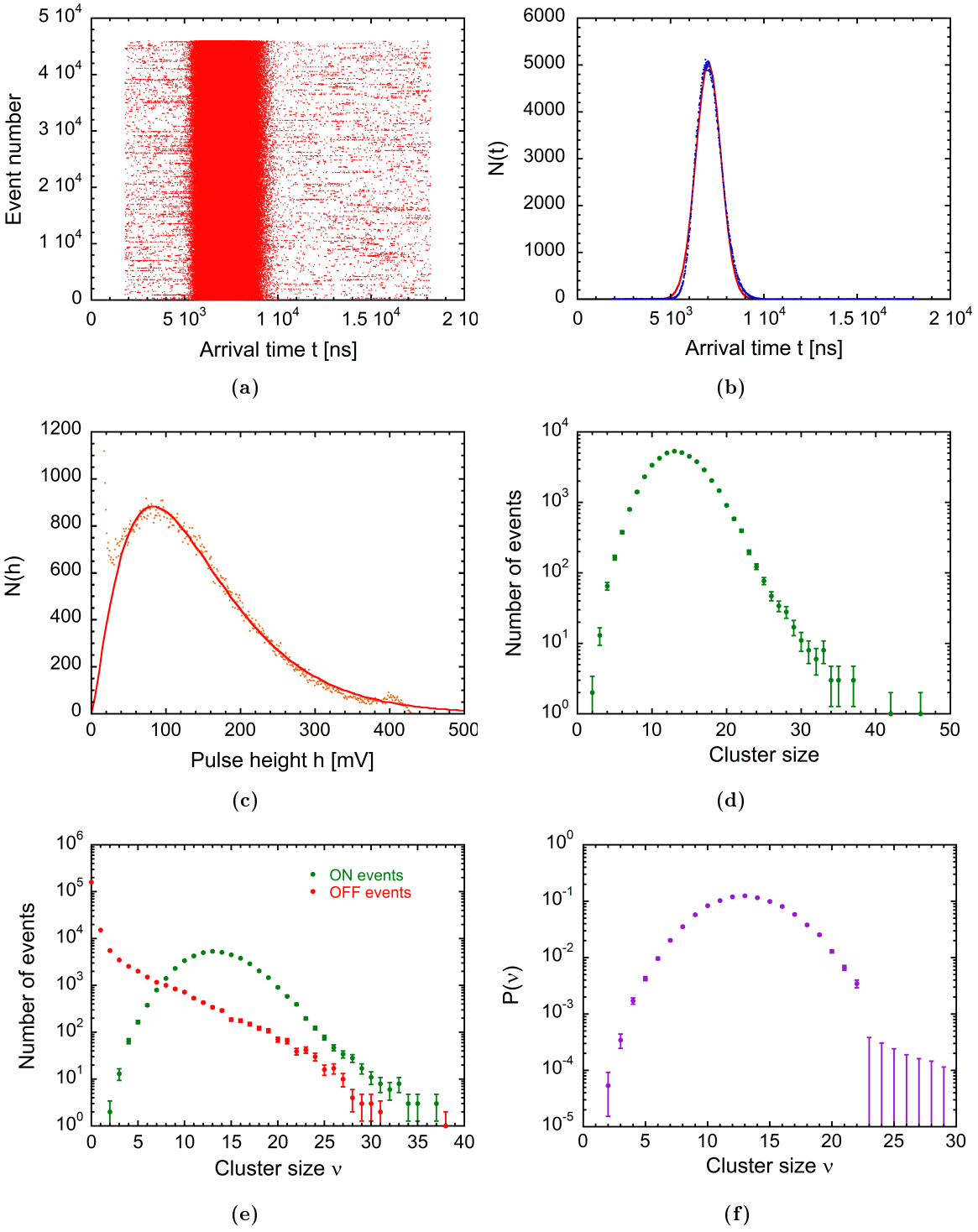


**Figure 3.9:** Steps of the data analysis procedure: (a) scatter plot of the arrival time of the pulses (x axis) after each trigger signal (y axis); (b) time distribution of the pulses (blue dots) and Gaussian fit (red curve); (c) gain distribution (orange dots) and Polya fitting function (red curve); (d) resulting cluster distribution after applying a time window and a lower gain threshold; (e) comparison between ON and corresponding OFF measurement; (f) final cluster size distribution after the deconvolution procedure. The data are shown for 72-MeV carbon ions at impact parameter $d = 0\,\mathrm{mm}$, at a gas pressure of 300 Pa. In the cluster size distributions, statistical uncertainties are plotted.

tributions of the accepted pulses are plotted, in order to check that they are consistent with the expected distributions. A fit is performed by means of a least-squares algorithm, using a Polya function for the pulse-height spectrum and a Gaussian superposed with a uniform background for the time-of-arrival one. This uniform background is due to random coincidences (for instance due to cosmic rays) and spurious pulses due to electronic noise.

In order to eliminate such events, a filter both in time and in gain is then applied: if a signal has an amplitude below the given gain threshold, it is discarded and the number of electrons in the cluster is reduced by one. If a signal has arrived outside the expected time window, the entire event is discarded and the total number of valid events (*i.e.*, primary ions) is decreased by one. This is because such an event has a very high probability of being due to a random coincidence. The final cluster size distribution is then obtained by counting the number of remaining electrons for each primary particle and normalizing the resulting distribution on the number of valid events.

The cluster size distribution obtained with this procedure is shown in Figure 3.9(d) for incident 72-MeV carbon ions: it has a maximum at cluster 13 and a long tail up to cluster 40. The latter is due to delta rays emitted by the primary particle which enter in the drift column through the electron collector hole: the ionizations induced in the propane gas inside the column are therefore detected with high efficiency (Conte, 2010). Since these events are induced by the primary particle, they are correlated with it and most of them are not eliminated by the filtering with a time window. This effect is of course more relevant for small impact parameters, due to the higher solid angle under which the electron collector hole is seen by the incident particle.

In order to compensate for this effect, after each measurement a second acquisition is always performed, in which the electric field inside the sensitive volume is reversed (the so-called OFF measurements). In this way the electrons produced inside the sensitive volume are driven to the cathode, and only those produced inside the drift column are detected. Since in both cases the voltage gap between the cathode and the first electrode of the electron collector is only a few electronvolts, the secondary electron spectrum is not altered significantly by the field reversion. The total measured ON distribution (*i.e.*, the one with the electric field shaped so to collect electrons from the sensitive volume) is the result of a convolution of the "real" ionization cluster size distribution in the sensitive volume and the OFF distribution (Conte, 2010):

$$P_\nu^{(\mathrm{ON})} = \sum_{j=0}^{\nu} P_{\nu-j}^{*}\, P_j^{(\mathrm{OFF})} \tag{3.14}$$

An unfolding procedure is therefore applied to reconstruct the distribution of the number of ionizations inside the sensitive volume only:

$$P_0^{*} = \frac{P_0^{(\mathrm{ON})}}{P_0^{(\mathrm{OFF})}}\,; \qquad P_\nu^{*} = \frac{P_\nu^{(\mathrm{ON})} - \sum_{j=1}^{\nu} P_{\nu-j}^{*}\, P_j^{(\mathrm{OFF})}}{P_0^{(\mathrm{OFF})}} \tag{3.15}$$

## 3.5 Determination of the effective site size

The physical size of the cylindrical sensitive volume of the Startrack counter is 3.7 mm in both height and diameter. Since the counter is filled with pure propane at a pressure of

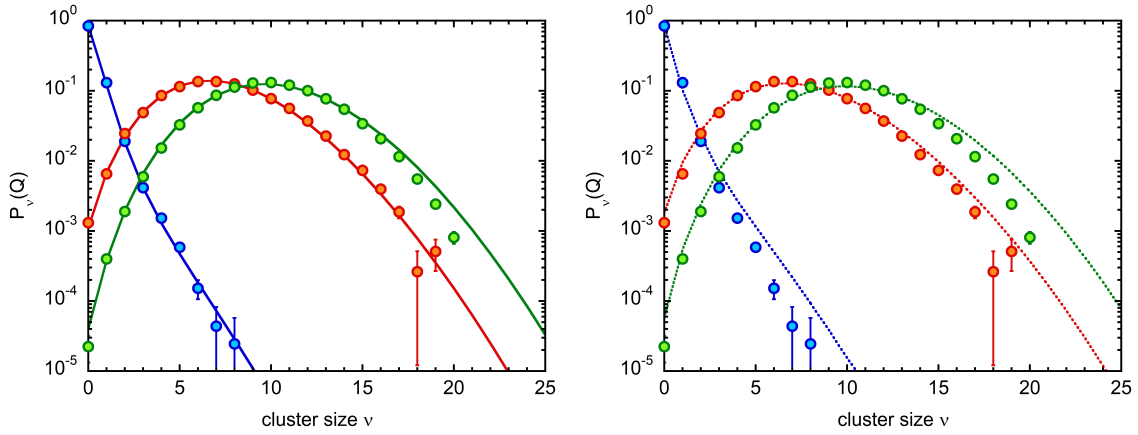


**Figure 3.10:** (a) Ionization cluster size distributions measured with the Startrack counter at impact parameter $d = 0\,\text{mm}$, for 25-MeV protons (blue), 5.8-MeV $\alpha$ particles (orange) and 16.4-MeV $^7$Li ions (green), compared with Monte Carlo simulation with the *MC-Startrack* code taking into account the efficiency map. (b) The same experimental distributions compared with simulations at 100% detection efficiency, considering a sensitive volume of 4 nm in propane (equivalent to 5 nm in water).

300 Pa ($\rho = 5.47\,\mu\text{g/cm}^3$ at a temperature of 25°C), this corresponds to a size of about 20 nm after scaling at unit density. Pure propane is not tissue-equivalent, however, according to the approximate scaling procedure discussed in Section 2.5.2, the ionization cluster size distributions measured in a propane volume of size $D_p$ are the same as those in a liquid water volume of size $D_w = 1.24\,D_p$. The water-equivalent size of the sensitive volume of the Startrack counter is therefore 25 nm. In this volume, the average experimental detection efficiency is 20%.

However, the response function of the counter influences strongly the resulting ionization cluster size distributions. In particular, the non-uniform detection efficiency reduces the number of collected electrons, shifting the distributions to lower clusters. A deconvolution of the response function of the detector from the measured data should therefore be carried out in order to derive the original cluster distribution in the target volume (De Nardo, 2002a). Such a procedure is however very complex and prone to errors, moreover, it requires that both the measured ICSD and the response function of the detector are known with an accuracy which is much beyond the one presently attainable in experiments. A different analysis has therefore been carried out, based on the definition of an *effective* target size $D_{\text{eff}}$, in which the ICSD measured at 100% detection efficiency are the same as those measured in a bigger volume at a lower and possibly non-uniform detection efficiency.

The possibility to define such an effective target size and its eventual determination in the case of the sensitive volume of the Startrack counter at 300 Pa of gas pressure were investigated by comparison with Monte Carlo simulations carried out with the *MC-Startrack* code. A first set of simulations was carried out taking into account the response function of the detector, in order to validate the code against experimental data: in particular, the spatially-dependent efficiency map, the time resolution and an additional uniform detec-

tion efficiency factor (representing, for instance, the MSAC amplification efficiency) were included in the simulations. An example of such a validation is reported in Figure 3.10(a), but also in Section 2.4.2.

Then, another set of simulations for the same radiation qualities was carried out at 100% detection efficiency, in order to estimate $D_{\text{eff}}$. A first guess is that it is equal to the physical size of the detecting volume (scaled at unit density) multiplied by the average detection efficiency:

$$(D\rho)_{\text{eff}} = (D\rho)_{\text{phys}} \cdot \overline{\varepsilon} \tag{3.16}$$

This is supported by the transmission properties of the binomial distribution (De Nardo, 2002a), from which it follows that $M_1^{\text{exp}}(Q, d, D, \varepsilon) = \overline{\varepsilon}\, M_1(Q, d, D)$; and by the result of the comparison between ionization cluster size distribution measured with the Ion Counter and the Jet Counter, measured during the BioQuaRT experiment.

The comparison of the experimental cluster size distributions with the simulations at 100% detection efficiency in an effective volume 5 nm in size is reported in Figure 3.10(b): the agreement between the distributions is generally quite good, even if some differences are present. The 25 nm sensitive volume of the Startrack counter, which has an average detection efficiency of 20%, can therefore be considered approximately equivalent to an effective water target 5 nm in size, in which the detection efficiency is 100%.

However, a complete correspondence cannot be expected: in the case of a 5 nm volume at 100% detection efficiency, the fraction of secondary electrons which are able to escape the target volume is about 20%, while it decreases to about 3% in the case of a volume 25 nm in size. The degradation of secondary electrons is therefore very different in the two volumes. The information on the spatial structure of the tracks is partially lost by the smoothing produced by the bigger volume and low detection efficiency, however, some level of invariance of the ionization yield seems to be present in the immediate vicinity of primary particle tracks, allowing the definition of an effective target size.

# Chapter 4

# Reduction of the target size

The Startrack counter has successfully investigated the stochastics of the ionization yield of different radiation qualities in target volumes of nanometric size. From these measurements, it has been found that the cumulative distributions $F_1$, $F_2$ and $F_3$ are uniquely determined by the mean ionization yield $M_1$, regardless of the specific radiation quality under analysis. Moreover, measurements carried out with other nanodosimetric counters also lie on this unique curve, confirming its general validity regardless of the detection efficiency, the type of counting gas, and the sensitive volume size. From this, it could be expected that also for the Startrack counter, changing the target size (by changing the gas pressure) or the detection efficiency will cause a shift in the $M_1$ value, but the corresponding $F_k$ should move along the same curves accordingly.

In order to test this assumption, tests were carried out at different gas pressures, corresponding to varying equivalent sizes of the target volume. In particular, the pressure range below 300 Pa has been investigated, in order to reach effective sensitive volume dimensions of about 1 nm. At the standard propane pressure of 300 Pa, it has been found that an "effective" target size can be defined, by scaling the water-equivalent size with the average detection efficiency, which is about 20% at this pressure. The sensitive volume of the Startrack counter is therefore equivalent to an effective water volume about 5 nm in size. If the gas density is further reduced, an effective target size of about $1 - 2$ nm could be achieved.

However, the reduction of gas pressure will produce a decrease in the detection efficiency, due to the change in the electron transport parameters due to the variation of the reduced electric field. The effective target size reduction could therefore be stronger than what would be expected from the decrease in the gas pressure alone. Moreover, the very definition of an effective target size could be problematic at a lower gas pressure: it could be that the site size at which the measured cluster size distributions are equivalent to those at 100% detection efficiency changes with the radiation quality, due to the differences in the secondary electron spectrum.

This Chapter discusses some preliminary tests which have been carried out in order to characterize the response function of the Startrack counter at a pressure lower than the standard one of 300 Pa, in order to measure nanodosimetric magnitudes in a volume about 1 nm in size. First results for a pressure of 200 Pa and an impact parameter $d = 0$ mm are presented, which show that the response of the counter is consistent in these condi-

tions. The possibility to define an effective target size at this pressure is then discussed. Afterwards, results at other gas pressures are presented and discussed, together with the variation of nanodosimetric magnitudes with the site size. Finally, preliminary results for other impact parameters are presented.

## 4.1 Measurements at a gas pressure of 200 Pa

At a gas pressure of 200 Pa, the physical size of 3.7 mm of the sensitive volume of the Startrack counter corresponds to a length in mass per area of 1.35 $\mu$g/cm$^2$, which is equivalent to a site size of 13.5 nm when scaled at unit density. The detection efficiency will also change as a consequence of the reduction of gas pressure, because of the variation of electron transport parameters due to the change in the reduced electric field. However, these parameters are not a function of the $E/P$ value only: even if the voltage gaps between the various stages are scaled in order to keep the $E/P$ ratio constant, the strong non-uniformity of the electric field gives rise to non-equilibrium phenomena which can significantly alter the transport parameters (Mitev, 2004).

This problem is particularly critical for the sensitive volume and the electron collector, due to their small size and the strong inhomogeneity of the electric fields in this area. The secondary electrons generated by ionizing events are emitted randomly, and must travel some distance before they reach equilibrium with the electric field. This so-called relaxation length depends critically on the number of inelastic collisions undergone by the electron, and therefore on the gas density. It is therefore expected that the detection efficiency and the selectivity of the sensitive volume are significantly worsened by this effect.

Monte Carlo simulations of the electron transport inside the sensitive volume and the connector should therefore be carried out in order to determine the voltage values that optimize the detection efficiency and the selectivity of the electrostatic walls. An experimental determination of the detection efficiency such as that carried out at a pressure of 300 Pa (described in Section 3.3) should also be made in order to check the consistency of the detection efficiency profile, given the large uncertainties in the electron impact cross sections at low energy.

For these first tests, the absolute values of the voltage biases have been kept constant on all the electrodes defining the sensitive volume and the electron collector, so that the reduced electric field is scaled by a constant factor in each spatial point of the interaction region. It has then be assumed as a first approximation that the detection efficiency scales linearly with the reduced electric field. This means that the shape of the efficiency map presented in Figure 3.7 is maintained if only the gas pressure is changed, while the absolute value of the detection efficiency at each point is scaled by a constant factor which is independent of spatial position.

This assumption has been checked by comparison between experimental measurements with the $^{244}$Cm $\alpha$-source and Monte Carlo simulations carried out with the *MC-Startrack* code. Figure 4.1 presents a comparison between the experimental ionization cluster size distributions at 200 Pa and at 300 Pa of gas pressure, compared with simulation results. The simulated distribution at 200 Pa includes the same efficiency map used for the simulations at 300 Pa of gas pressure and an additional efficiency factor of 24%, in order to take into account the postulated uniform reduction of the average detection efficiency with

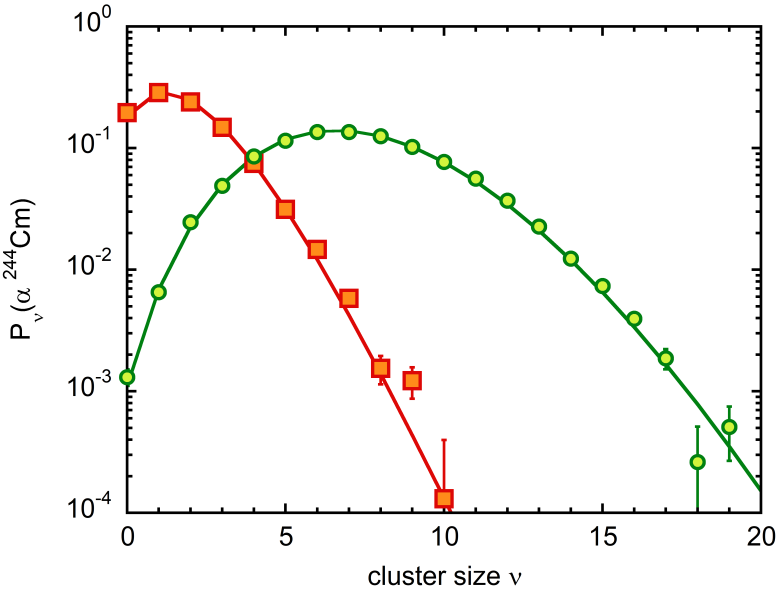


**Figure 4.1:** Comparison between measured and simulated ICSD for $\alpha$ particles from a $^{244}$Cm source, at a gas pressure of 300 Pa (green circles) and 200 Pa (orange squares). Symbols represent experimental data, lines correspond to Monte Carlo simulations. For the experimental data, the statistical uncertainties are plotted.

| **Ion type** | $E$ **[MeV]** | $D/\lambda_{\mathbf{ion}}$ | $\bar{\varepsilon}_{\mathbf{MSAC}}$ | **Add eff MC** | $M_1$ **exp** | $\frac{M_1}{\kappa(Q)}$ **corr** |
|---|---|---|---|---|---|---|
| $^1$H | 25 | 0.542 | 78% | 21% | 0.0371 | 0.079 |
| $^7$Li | 16.4 | 35.4 | 99% | 27% | 3.16 | 0.081 |
| $^{12}$C | 96 | 51.7 | 90% | 24% | 3.87 | 0.075 |
| $^{12}$C | 72 | 65.9 | 90% | 24% | 4.90 | 0.074 |
| $\alpha$ source | 5.8 | 23.0 | 90% | 24% | 1.82 | 0.079 |

**Table 4.1:** Summary of the radiation qualities used for the study at 200 Pa of propane pressure. The $M_1/\kappa(Q)$ values in the last column have been corrected for a MSAC efficiency of 90%.

decreasing gas pressure. At 300 Pa, this factor was set to 70%. The amplification efficiency of the MSAC, estimated from Polya fits of the gain distributions, is approximately 90% for both experimental measurements.

The agreement between the experimental and the simulated ICSD at 200 Pa is very good, confirming the validity of the above-mentioned approximation. The $M_1$ values are 1.8 at 200 Pa and 7.3 at 300 Pa; from their ratio, the detection efficiency at 200 Pa can be estimated to be about 7%, assuming that the $M_1$ values at 100% detection efficiency scale approximately with the size in mass per area of the sensitive volume. This approximation can be justified given the low specific energy (1.44 MeV/u) of $\alpha$ particles from the calibration source.

The investigation has then been extended to other radiation qualities, namely, 25-MeV protons, 16.4-MeV $^7$Li ions, and carbon ions of 96 MeV and 72 MeV. Since these measure-

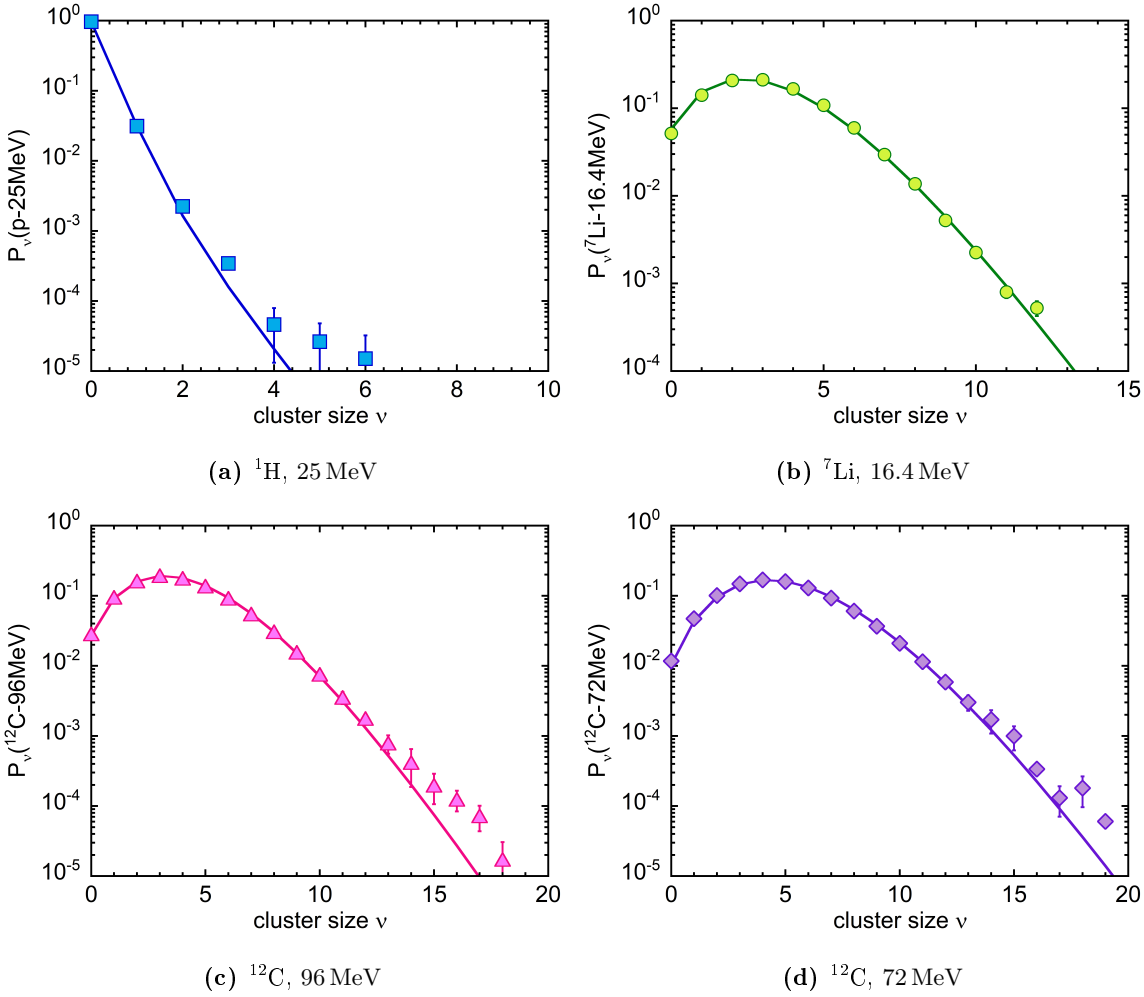


**(a)** $^{1}$H, 25 MeV **(b)** $^{7}$Li, 16.4 MeV

**(c)** $^{12}$C, 96 MeV **(d)** $^{12}$C, 72 MeV

**Figure 4.2:** Comparison between measured and simulated ICSD for different radiation qualities, at a gas pressure of 200 Pa and impact parameter $d = 0$ mm: (a) 25-MeV protons, (b) 16.4-MeV $^{7}$Li ions, (c) 96-MeV carbon ions, (d) 72-MeV carbon ions. Symbols represent experimental data, lines correspond to Monte Carlo simulations.

ments were carried out in different shifts and in different operating conditions, the MSAC amplification efficiency can vary: for each measurement, it has been estimated from the fit of the pulse-height distribution with a Polya function. Table 4.1 reports, for these radiation qualities, the value of $D/\lambda_{\text{ion}}$ at 200 Pa of propane pressure, the estimated value of the MSAC efficiency, the experimental mean cluster size distribution $M_1$ and the additional efficiency factor included in the Monte Carlo simulations. The result of the comparison between measured and simulated distributions is shown in Figure 4.2. The additional efficiency factor included in the MC calculations has been estimated by scaling the one used for alpha particles by the ratio of the MSAC amplification efficiency in the two cases.

The agreement between measured and simulated distributions is very good for all the radiation qualities which have been considered. The small differences which are present

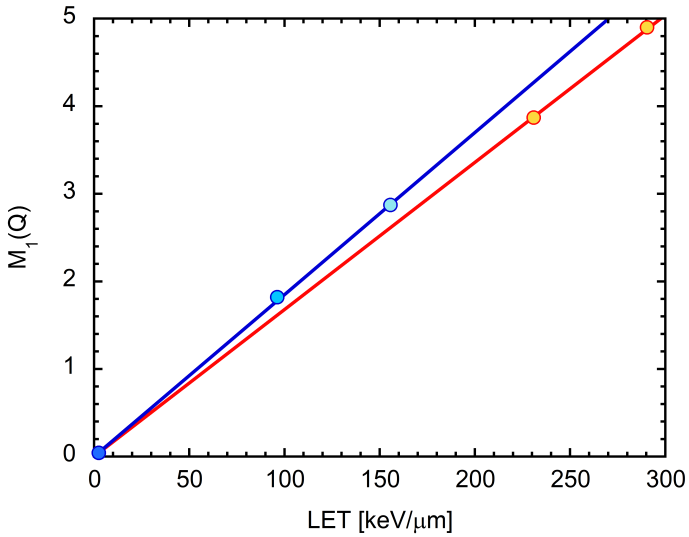


**Figure 4.3:** Mean ionization cluster size $M_1$ as a function of LET in propane, for a gas pressure of 200 Pa and primary particles of different charge state: $Z \leq 3$ (blue), and $Z = 6$ (red). Symbols correspond to experimental data, lines are the best fit with a straight line through zero $y = mx$.

at higher cluster sizes are probably due to incomplete background subtraction (especially in the case of carbon ions) or small variations in the operating conditions during measurements. For what concerns the $M_1$ values, it can be seen in Table 4.1 that they scale approximately with $D/\lambda_{\text{ion}}$, after a correction for the ratio of the specific MSAC efficiency with that of the measurement with the alpha calibration source. However, for carbon ions this ratio is lower than for ions which have a lower charge state, due to the contribution of secondary electrons to the total $M_1$: in fact,

$$M_1(Q, D, \varepsilon) = \overline{\varepsilon}\, M_1(Q, D, \varepsilon = 1) = \overline{\varepsilon}\, \overline{\kappa}(Q, D)\, m_1(Q, D, \varepsilon = 1) \tag{4.1}$$

(where $\overline{\varepsilon}$ is the average value of the total detection efficiency), and the contribution of secondary electrons can change the value of $M_1$ substantially. This point is further stressed in Figure 4.3, which shows the corrected values of $M_1$ as a function of LET in propane at unit density for the incident ion. The proportionality factor between $M_1$ and LET is lower for carbon ions than for particles of lower charge state, due to their higher velocity for a given LET value, which gives rise to a broader track.

### 4.1.1 Estimation of the effective volume size

At 200 Pa of gas pressure, the physical size in mass per area of the sensitive volume of the Startrack counter is 1.35 $\mu$g/cm$^2$, which is equivalent to 13.5 nm when scaled at unit density. This is equivalent to a volume size of about 17 nm in liquid water. As for the case of 300 Pa of gas pressure, the question arises if this physical dimension can be related to an effective target size which takes into account the average detection efficiency, which in this case is about 7%, independently of the specific radiation quality under analysis.

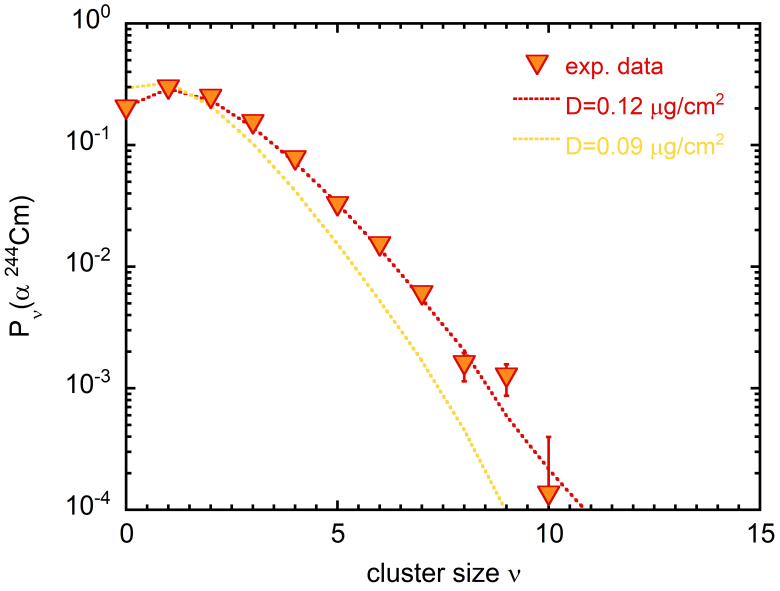


**Figure 4.4:** Comparison between measured ICSD for $\alpha$ particles from a $^{244}$Cm source, and simulations at 100% detection efficiency in a volume of $0.12\,\mu g/cm^2$ of mass per area. The simulated ICSD in a volume of the "expected" $D_{\rm eff} = \bar{\varepsilon}\, D_{\rm phys}$ is also reported for comparison. For the experimental data, statistical uncertainties are plotted.

| Ion type | Energy | $\bar{\varepsilon}_{\rm MSAC}$ | $(D\rho)_{\rm phys}$ $C_3H_8$ MC | $D_{\rm eff}$ $H_2O$ corr |
|---|---|---|---|---|
| $^{1}$H | 25 MeV | 78% | $0.10\,\mu g/cm^2$ | 1.5 nm |
| $^{7}$Li | 16.4 MeV | 99% | $0.13\,\mu g/cm^2$ | 1.5 nm |
| $^{12}$C | 96 MeV | 90% | $0.12\,\mu g/cm^2$ | 1.5 nm |
| $^{12}$C | 72 MeV | 90% | $0.12\,\mu g/cm^2$ | 1.5 nm |
| $\alpha$ source | 5.8 MeV | 90% | $0.12\,\mu g/cm^2$ | 1.5 nm |

**Table 4.2:** Effective volume size obtained for different radiation qualities by comparison with Monte Carlo simulation with 100% detection efficiency. The $D_{\rm eff}$ values in the last column have been corrected for a MSAC efficiency of 90%.

The possibility to define an effective target size has been investigated again with Monte Carlo simulations carried out with the *MC-Startrack* code. For the case of a gas pressure of 300 Pa, this can indeed be done, and it is found that $D_{\rm eff} = \bar{\varepsilon}\, D_{\rm phys}$. If an analogous estimation is carried out for the case of 200 Pa, an effective target size of 1.2 nm in liquid water would be expected. This is however not the case: the comparison with Monte Carlo simulations shows that the effective target size is bigger.

Figure 4.4 shows the result of the comparison in the case of $\alpha$ particles from the $^{244}$Cm calibration source: the simulated distribution for a target 1.2 nm in size is peaked at a cluster size much lower than the experimental one. More simulations were therefore carried out increasing the size of the propane target with steps of 0.4 nm, in order to find the value of $D$ which gives the closest $M_1$ value to the experimental one. The latter was

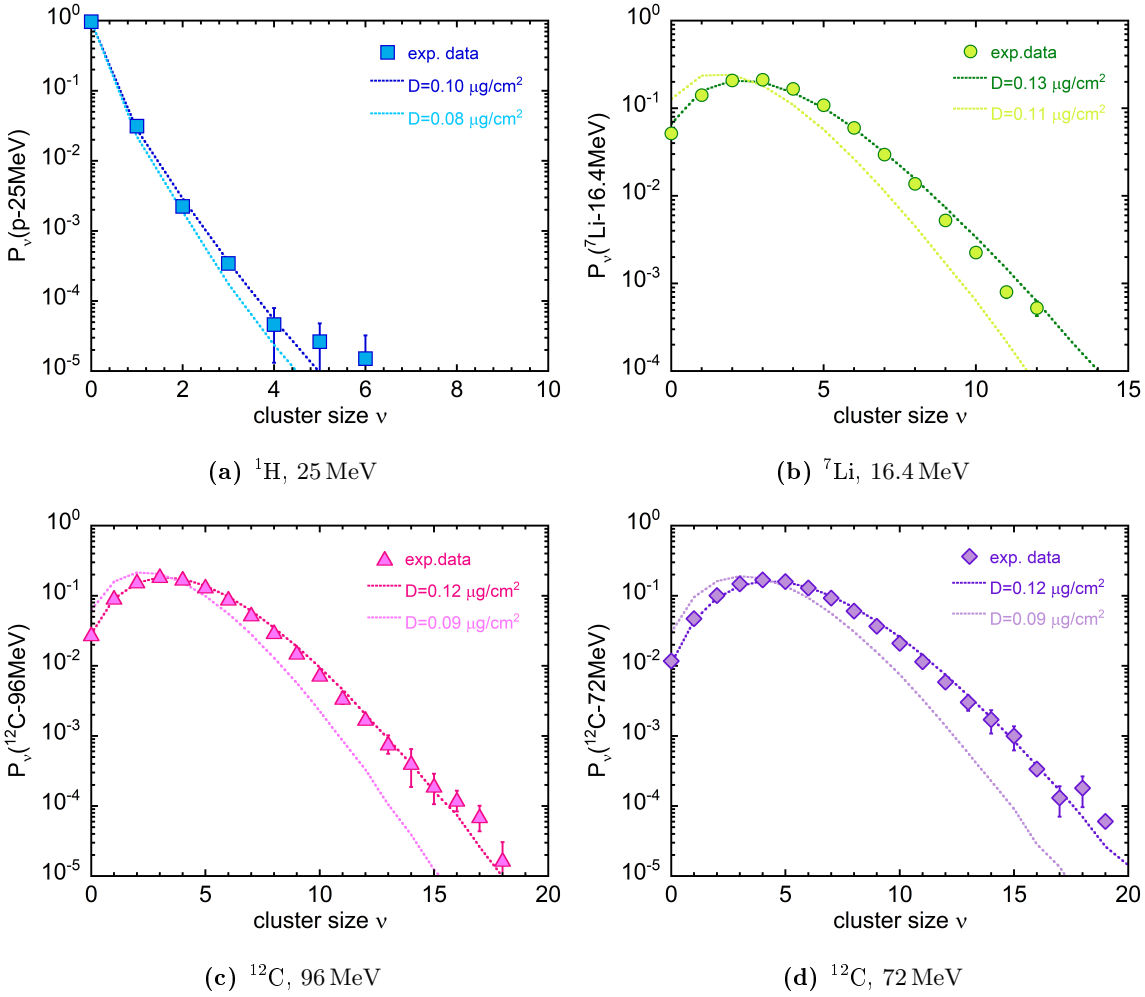


**(a)** $^{1}$H, 25 MeV **(b)** $^{7}$Li, 16.4 MeV

**(c)** $^{12}$C, 96 MeV **(d)** $^{12}$C, 72 MeV

**Figure 4.5:** Comparison between measured ICSD for different radiation qualities and simulations at 100% detection efficiency. The volume sizes considered in the simulations have been scaled for the ratio of the MSAC efficiency for each specific radiation quality to that for $\alpha$ particles. The simulated ICSD in a volume of the "expected" $D_{\mathrm{eff}} = \bar{\varepsilon}\, D_{\mathrm{phys}}$ is also reported for comparison. (a) 25-MeV protons, (b) 16.4-MeV $^{7}$Li ions, (c) 96-MeV carbon ions, (d) 72-MeV carbon ions.

found for a sensitive target size of 1.5 nm in liquid water, and in this case, the calculated ICSD reproduces very well the trend of experimental data.

This value for the effective target size is confirmed by the comparison for other radiation qualities, shown in Figure 4.5: if the amplification efficiency of the MSAC is the same as that for the measurement with the $\alpha$ source, the agreement between the experimental ICSD and the simulated one in a target of 1.5 nm is very good. In the case of protons and lithium ions, the MSAC efficiency is different, so the distribution at 1.5 nm do not show the same trend as the experimental data. However, if the target size of the simulation is scaled with the ratio of the MSAC efficiency with that of the measurement with alpha particles, a very good agreement is again found (see Table 4.2 for further details). At 200 Pa of

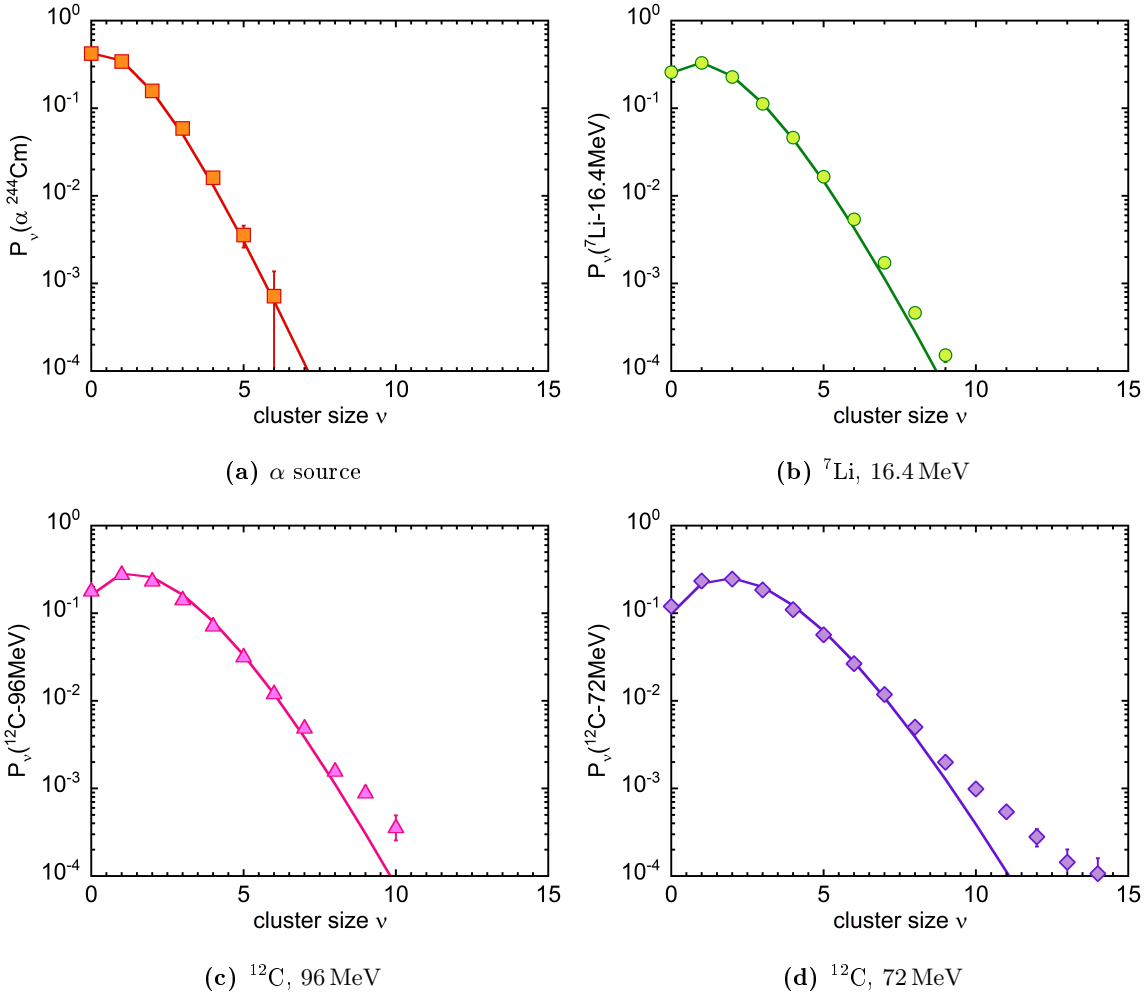


**(a)** $\alpha$ source **(b)** $^{7}$Li, 16.4 MeV

**(c)** $^{12}$C, 96 MeV **(d)** $^{12}$C, 72 MeV

**Figure 4.6:** Comparison between measured and simulated ICSD for different radiation qualities, at a gas pressure of 170 Pa and impact parameter $d = 0$ mm: (a) 5.8-MeV $\alpha$ particles from the $^{244}$Cm calibration source, (b) 16.4-MeV $^{7}$Li ions, (c) 96-MeV carbon ions, (d) 72-MeV carbon ions. Symbols represent experimental data, lines correspond to Monte Carlo simulations.

propane pressure, the sensitive volume of the Startrack counter is therefore equivalent to an effective target of 1.5 nm in liquid water.

## 4.2 Measurements at a gas pressure of 170 Pa

Other preliminary tests have been carried out at a gas pressure of 170 Pa. At this pressure, the physical size in mass per area of the sensitive volume is 1.15 $\mu$g/cm$^2$, corresponding to 11.5 nm if scaled at unit density. Also in this case, the voltage biases on all electrodes of the interaction region and the electron collector have been kept constant, and it has been assumed that the detection efficiency scales linearly with the reduced electric field.

This assumption has been checked again by comparison between experimental mea-

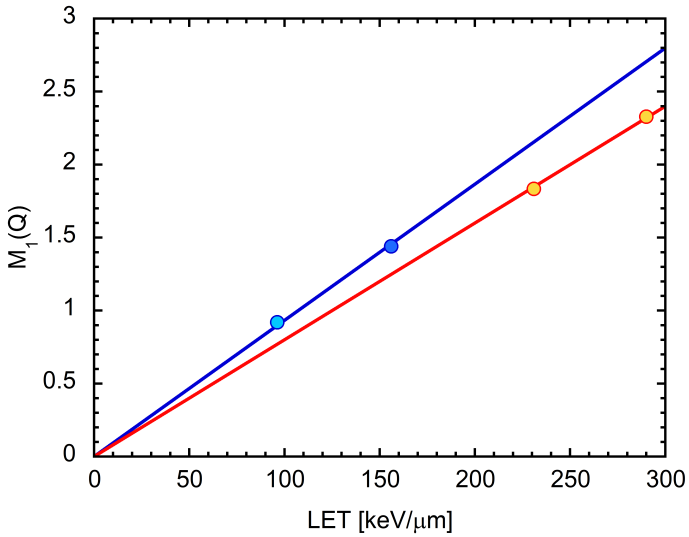


**Figure 4.7:** Mean ionization cluster size $M_1$ as a function of LET in propane, for a gas pressure of 170 Pa and primary particles of different charge state: $Z \leq 3$ (blue), and $Z = 6$ (red). Symbols correspond to experimental data, lines are the best fit with a straight line through zero $y = mx$.

| Ion type | $E$ [MeV] | $D/\lambda_{\text{ion}}$ | $\bar{\varepsilon}_{\text{MSAC}}$ | Add eff MC | $M_1$ exp | $\frac{M_1}{\kappa(Q)}$ corr |
|---|---|---|---|---|---|---|
| $^{7}$Li | 16.4 | 30.0 | 90% | 14% | 1.44 | 0.048 |
| $^{12}$C | 96 | 44.0 | 91% | 14% | 1.83 | 0.042 |
| $^{12}$C | 72 | 56.0 | 90% | 14% | 2.33 | 0.042 |
| $\alpha$ source | 5.8 | 19.6 | 90% | 14% | 0.921 | 0.047 |

**Table 4.3:** Summary of the radiation qualities used for the study at 170 Pa of propane pressure.

surements with the $\alpha$ particle source and Monte Carlo simulations. The result of this comparison is presented in Figure 4.6(a): if an additional efficiency factor of 14% is considered in the simulation, the calculated ICSD reproduces very well the trend of experimental data at 170 Pa of propane pressure. This is confirmed also by a similar analysis carried out for other radiation qualities, reported in Figure 4.6: since the MSAC efficiency, estimated from a Polya fit on the pulse-height distributions, is about 90% for all of them, the same factor of 14% has been considered in all simulations. A good agreement is generally found between the measured and the simulated ICSD, even if at such a low gas pressure the measured distributions exhibit a longer tail at higher clusters, especially in the case of carbon ions, which is probably due to incomplete background subtraction. The approximation of linear scaling of the detection efficiency with the reduced electric field seems therefore to hold also for a propane pressure of 170 Pa. In this case, the approximate value of the detection efficiency, estimated from the ratio of $M_1$ values at 170 Pa and at 300 Pa, is 4%.

The value of $D/\lambda_{\text{ion}}$, the experimental $M_1$ value and the ratio of the two are reported in Table 4.3. At 170 Pa of pressure, $M_1$ still scales approximately with $D/\lambda_{\text{ion}}$, however, a difference of about 13% is found in the ratio $M_1/\kappa(Q)$ for carbon ions with respect to

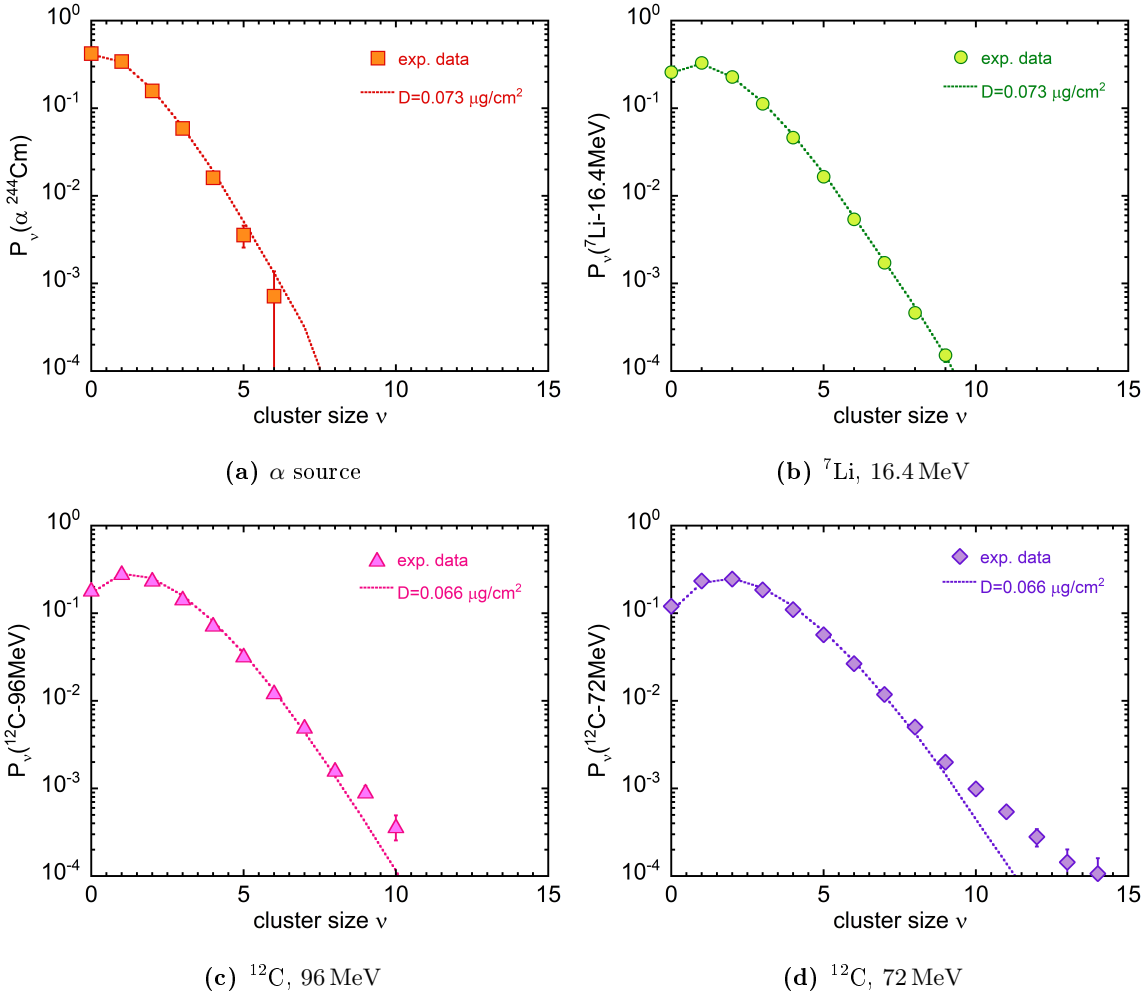


**(a)** $\alpha$ source **(b)** $^{7}$Li, 16.4 MeV

**(c)** $^{12}$C, 96 MeV **(d)** $^{12}$C, 72 MeV

**Figure 4.8:** Comparison between measured ICSD at a gas pressure of 170 Pa for different radiation qualities, and simulations at 100% detection efficiency: (a) 5.8-MeV $\alpha$ particles from the $^{244}$Cm calibration source, (b) 16.4-MeV $^{7}$Li ions, (c) 96-MeV carbon ions, (d) 72-MeV carbon ions. Symbols represent experimental data, dotted lines correspond to Monte Carlo simulations.

ions of lower charge state. In the case of 200 Pa, the latter was 9%: this seems therefore to indicate an increasing difference in the contribution of secondary electrons to the total $M_1$ for smaller volume sizes. This is also confirmed by the trend of $M_1$ as a function of LET in propane reported in Figure 4.7: the difference between the slope of the best fit line between carbon ions and particles of lower charge state is 15%, while it is 10% at a gas pressure of 200 Pa.

### 4.2.1 Estimation of the effective volume size

The possibility to define an effective target size, in which the cluster size distributions at 100% detection efficiency are the same as the measured ones, has also been investigated

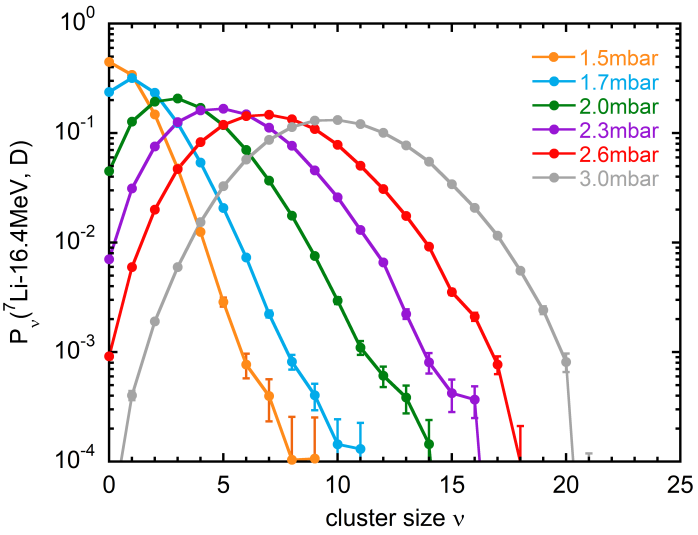


**Figure 4.9:** Measured ICSD for 16.4-MeV $^7$Li ions, at an impact parameter $d = 0\,\mathrm{mm}$, varying the propane pressure inside the sensitive volume of the Startrack counter.

for a propane pressure of 170 Pa. In this case, the size in mass per area of the sensitive volume is $1.15\,\mu\mathrm{g/cm^2}$, which is equivalent to 14 nm in liquid water, and the detection efficiency is about 4%. Given the fact that the definition of $D_{\mathrm{eff}}$ as the product of the physical water-equivalent size and the average detection efficiency does not hold already at a gas pressure of 200 Pa, the value of $D_{\mathrm{eff}}$ has been investigated by carrying out many simulations varying the propane target size with steps of 0.4 nm, and then choosing for each radiation quality the one for which the resulting $M_1$ value was closer to that of the experimental ICSD. The results of this study are reported in Figure 4.8.

It can be seen that for lithium ions and alpha particles the target size which gives the best agreement with the experimental distribution is $D = 0.73\,\mathrm{nm}$ (corresponding to 0.91 nm in liquid water), while for carbon ions it is $D = 0.66\,\mathrm{nm}$ (0.83 nm in liquid water). The two values differ by about 10%, implying that the concept of an effective target size seems to fail for small site sizes. However, further measurements with other radiation qualities and gas pressures are needed in order to confirm this finding.

## 4.3 Measurements at other gas pressures

Further tests have been carried out by varying the propane pressure inside the counter in the range $150 - 300\,\mathrm{Pa}$, with a step of 10 Pa, in order to investigate the operational limits of the Startrack counter and the variations of nanodosimetric magnitudes with the size in mass per area of the sensitive volume. This investigation was carried out with $^7$Li ions at an energy of 16.4 MeV, considering only the case of central passage (impact parameter $d = 0\,\mathrm{mm}$). In all cases, the voltage biases to all the electrodes of the sensitive volume and the electron collector have been kept constant, and a linear scaling of the efficiency with the reduced electric field has been assumed. At a propane pressure of 150 Pa, the size of

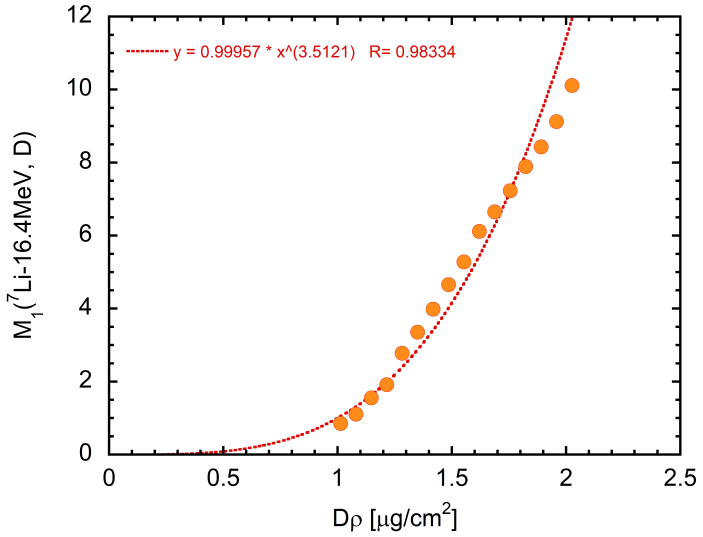


**Figure 4.10:** Mean values of the ICSD measured for 16.4-MeV $^7$Li ions for different gas pressures, as a function of the sensitive volume size in mass per area. Symbols represent experimental data, the dotted curve is a best fit with a power function $y = mx^c$.

the sensitive volume is about 10 nm when scaled at unit density.

The measured ionization cluster size distributions are reported in Figure 4.9, for different propane pressures. As expected, their maximum is shifted to lower clusters with decreasing volume dimensions, however, this shift is not linear with the target size in mass per area, due to the combined effect of the strong reduction of the detection efficiency with decreasing gas pressure and the change in the secondary electron contribution to the total ionization yield. This point is further stressed in Figure 4.10, which shows the trend of $M_1$ as a function of the sensitive volume size: the increase of $M_1$ with increasing $D\rho$ is supra linear and, as a first very rough approximation, can be modelled with a power function of exponent 3.5.

## 4.4 Complementary cumulative distribution functions

For the standard gas pressure of 300 Pa, it was found that the values of the complementary cumulative distributions $F_1$, $F_2$ and $F_3$ define a unique curve when plotted as a function of the mean ionization yield $M_1$, regardless of the specific radiation quality under analysis. Moreover, measurements obtained with other nanodosimetric counters also lie on the same curves, regardless of the specific sensitive volume size, type of filling gas and detection efficiency. It is therefore interesting to see if this invariance holds also for the measurements with different volume size discussed in this Chapter.

Figure 4.11 presents the values of $F_2$ obtained with the Startrack counter for the radiation qualities previously discussed, for propane pressure of 200 Pa and 170 Pa, superposed with the unique curve of $F_2$ as a function of $M_1$ for the three different nanodosimetric counters presented Figure 2.15. Some additional experimental data at 300 Pa of propane

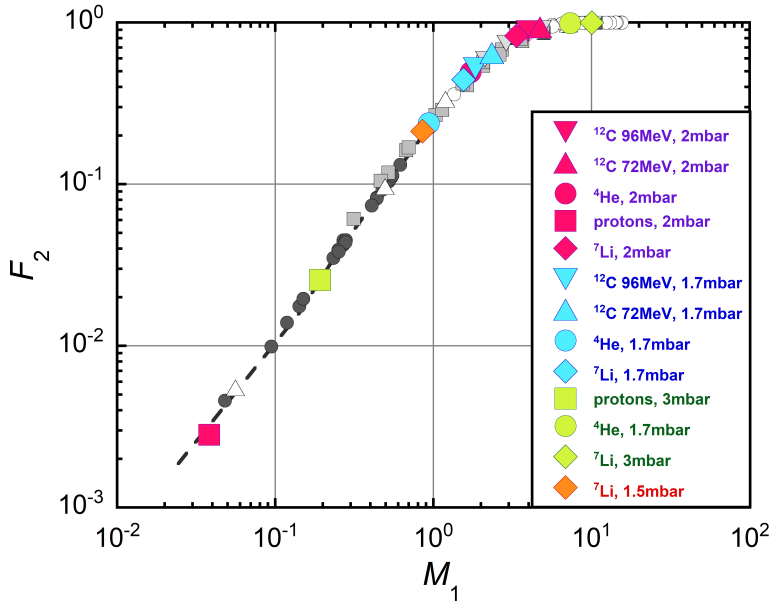


**Figure 4.11:** $F_2$ values plotted as a function of $M_1$ for the measurements carried out with the Startrack counter at a propane pressure lower than the standard one of 300 Pa, compared with the unique curve of Figure 2.15 obtained from measurements with different nanodosimetric counters.

pressure are also shown. The agreement between the new data points and the curve defined by previous measurements is very good, confirming that the relation between $F_2$ and $M_1$ is independent of all specific measuring conditions. This is also confirmed by the analysis of the data obtained with 16.4-MeV $^7$Li ions in sensitive volumes of varying mass thickness, reported in Figure 4.12.

The general validity of the unique relations between the $F_k$ values and the mean ionization yield $M_1$ is confirmed also by the analysis of $F_1$ and $F_3$, reported in Figure 4.13. Given these unique relations, which are valid regardless of the type and energy of the particles composing the radiation field and the specific operating conditions of the nanodosimeters, the complementary cumulative distribution functions appear as promising candidates to correlate the nanodosimetric track structure description to the biological likelihood of late damage.

## 4.5 Preliminary results for other impact parameters

In the case of carbon ions at an energy of 96 MeV and 72 MeV, a preliminary investigation of the variation of the ICSD with the impact parameter has been carried out at a propane pressure of 200 Pa. An impact parameter range between 0 and 5 mm was considered, which corresponds to a range in mass per area up to about 1.8 $\mu$g/cm$^2$. The resulting ionization cluster size distributions are reported in Figure 4.14 for the case of 72 MeV carbon ions: as expected, the maximum of the distribution moves to lower cluster sizes if the impact parameter increases. Moreover, the two distributions at $d = 4$ mm and $d = 5$ mm are

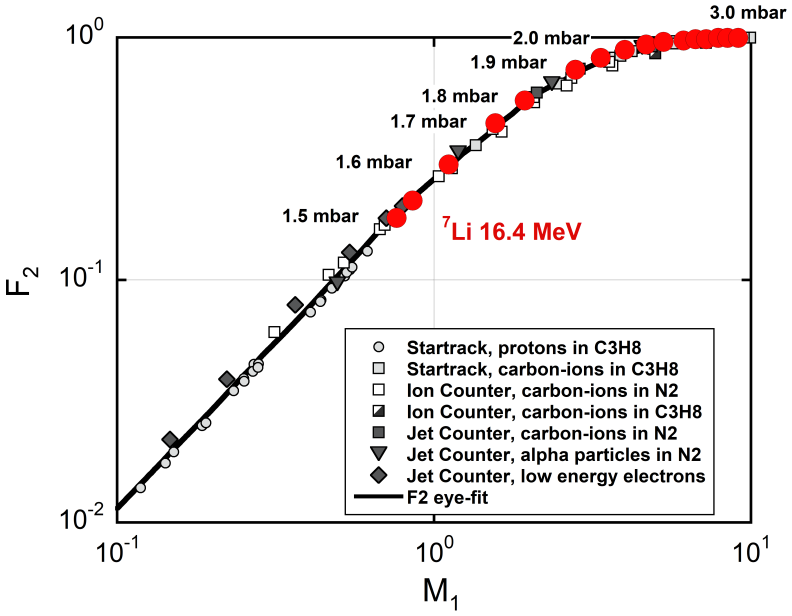


**Figure 4.12:** $F_2$ values plotted as a function of $M_1$ for 16.4-MeV $^7$Li ions from measurements carried out with the Startrack counter in sensitive volumes of varying mass thickness, compared with the unique curve of Figure 2.15 obtained with different nanodosimetric counters.

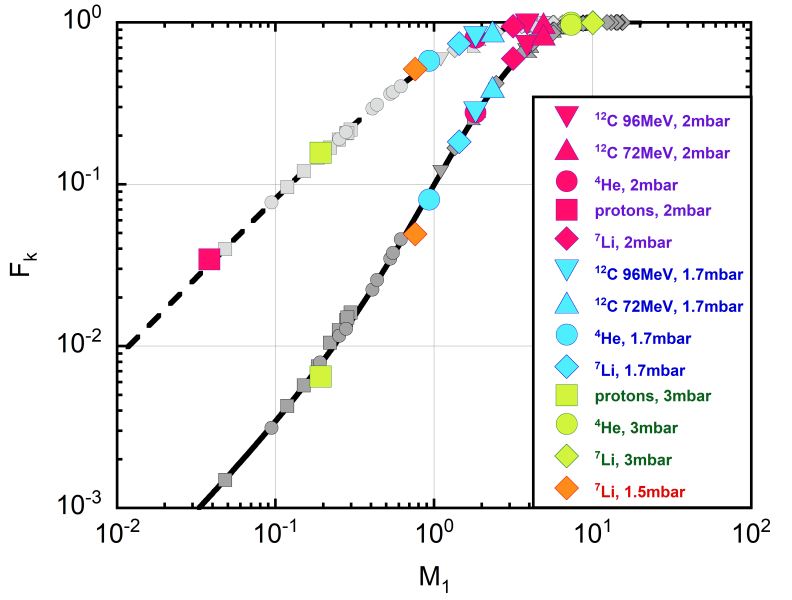


**Figure 4.13:** Values of $F_1$ and $F_3$ plotted as a function of $M_1$ for the same measurements carried out with the Startrack counter presented in Figure 4.12, compared with the unique curves of Figure 2.16 obtained from measurements at a propane pressure of 300 Pa.

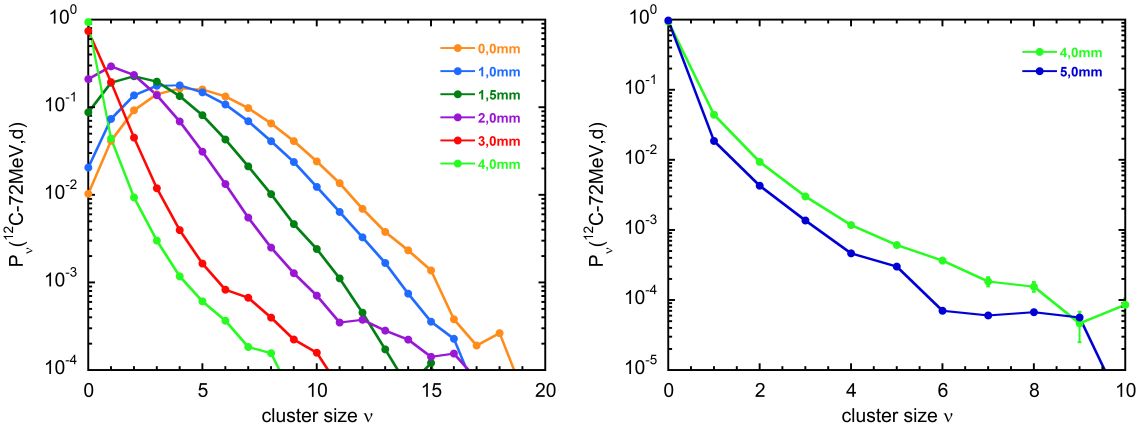


**(a)** Track core **(b)** Penumbra

**Figure 4.14:** Experimental ionization cluster size distributions for 72 MeV carbon ions measured at a propane pressure of 200 Pa, corresponding to a target size of 1.35 $\mu$g/cm$^2$, for different impact parameters in the range $0 - 5$ mm.

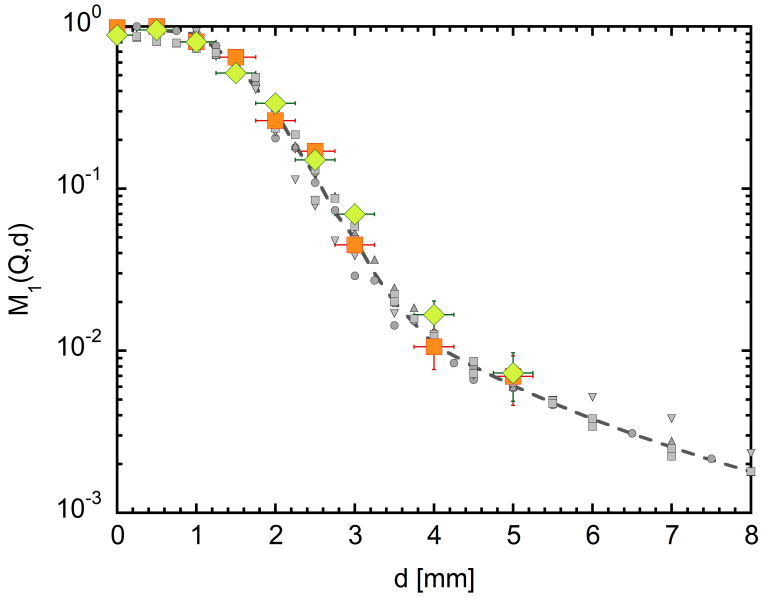


**Figure 4.15:** Mean ionization cluster size $M_1$ as a function the impact parameter $d$ at a gas pressure of 200 Pa, for carbon ions at 96 MeV (orange squares) and 72 MeV (green diamonds). The data at 300 Pa shown in Figure 2.9 are also plotted for comparison (gray symbols and dashed trend line). Uncertainties are plotted on both $M_1$ and $d$: the latter are estimated again as 2/3 of the beam radius, *i.e.* $\pm 0.25$ mm.

parallel to each other, as it was found for a gas pressure of 300 Pa. However, this behaviour of the distributions in the penumbra region is not confirmed by the analysis of the data at an energy of 96 MeV: in this case, the two distributions are not parallel to each other.

This could be an effect of incomplete or excessive background subtraction in one of the two cases.

The trend of the mean ionization yield as a function of the impact parameter is reported in Figure 4.15: the shape of the $M_1$ profile is approximately the same as that for the case of 300 Pa of propane pressure. This is somewhat surprising because at a pressure of 200 Pa each physical impact parameter corresponds to a smaller distance in mass per area from the primary particle track than in the case of 300 Pa: the electron degradation should therefore be different in the two cases. The invariance of the profile with gas density suggests therefore that $M_1$ is mainly determined by the solid angle under which the sensitive volume is seen from the primary particle track, which is the same at 200 Pa and 300 Pa, and that the differences in secondary electron degradation play only a minor role. However, further measurements are needed in order to clarify this point.

# Chapter 5

# Track structure and radiobiology

In the previous Chapters, an analysis of the stochastics of the ionization yield for different radiation qualities and in sensitive volumes of different size has been carried out. In particular, it has been shown that the complementary cumulative distribution functions $F_k$ are unique functions of the mean ionization yield $M_1$, regardless of the incident radiation quality, the target volume size, the type of interaction medium, and the detection efficiency of the counter. Now, the question arises whether the purely physical description of the track structure presented up to now can be correlated to different end-points of radiobiological damage.

Various studies have been carried out concerning this point, based on assumptions of different complexity (Grosswendt, 2004b; Garty, 2010) in order to relate the ionization yield in a target volume of nanometric size to the yield of SSB, DSB or clustered lesions. The latter are usually estimated from measurements carried out with plasmid DNA, or from simulations with track structure codes which implement also geometrical models of the DNA molecule. The predictions of these models are quite consistent with these estimations, however, further assumptions are needed in order to correlate DNA damage yields with effects at cellular level.

In this Chapter, a different analysis is presented, which correlates directly nanodosimetric quantities and radiobiological data of cell survival, obtained from the literature. It starts from the intuitive idea that the $F_k$ values are related to damage complexity, and from the fact that the shape of the curves defined by $F_k$ as a function of $M_1$ shows a saturation for high values of $M_1$, which is similar to the trend of inactivation cross sections as a function of LET.

In order to make a direct comparison between the physical and the radiobiological data, it would be necessary to make pairwise measurements of inactivation cross sections and nanodosimetric quantities. This has not been done yet, and the comparison is therefore necessarily based on literature data. Nevertheless, an astonishing correspondence can be drawn between the stochastics of the ionization yield in nanometric volumes and biological effects at cellular level.

The radiobiological data which have been used for this analysis have been taken from the literature sources listed in the PIDE database[(1)] (Friedrich, 2013). This is a database of about 800 cell survival experiments taken from a literature review including at present

[(1)] http://www.gsi.de/bio-pide

about 80 publications, from which RBE values can be calculated. A wide range of radiation qualities and cell lines is considered, allowing to study the influence of various physical and biological parameters.

## 5.1 Inactivation cross sections

The shape of cell survival curves is described mathematically by the so-called linear-quadratic dose-response model of cell survival, which expresses the functional dependence between surviving fraction and absorbed dose as a second order polynomial in the semi-logarithmic scale:

$$S(D) = \mathrm{e}^{-(\alpha D + \beta D^2)} \tag{5.1}$$

where $S(D)$ is the surviving fraction at dose $D$. The $\alpha$ parameter corresponds to the initial slope of the survival curve, while the $\beta$ parameter describes its shoulder and has been related to the influence of cellular repair mechanisms, which become saturated at high doses. The $\alpha$ and $\beta$ parameter are reported in the PIDE database for each survival experiment, together with the primary particle type, energy and LET of the incident beam.

In order to compare track structure quantities, which refer to single particle tracks, to radiobiological data, a fluence-related parameter must be defined to describe cell survival. Formally, the probability per unit fluence for a biological effect to occur is expressed by the *action cross section*. The inactivation cross section $\sigma$ is used to express the probability that the cell is inactivated by the passage of a single particle that hits the critical target. It is defined for a given survival level $l$ from the slope $s_l$ of the survival curve in the semi-logarithmic plot (Belloni, 2002):

$$\sigma_l \phi_l = s_l D_l \tag{5.2}$$

where $\phi_l$ is the fluence and $D_l$ is the dose corresponding to the survival level $l$. $s_l$ can be expressed as

$$s_l = -\frac{\mathrm{d} \ln S(D)}{\mathrm{d}D}\bigg|_{D=D_l} = \alpha + 2\beta D_l \tag{5.3}$$

and $D_l$ is related to $\alpha$, $\beta$ and $l$ by the linear-quadratic equation 5.1, which gives

$$-\ln l = \alpha D_l + \beta D_l^2 \tag{5.4}$$

Solving this equation for $D_l$ and taking into account that for monoenergetic beams dose and fluence are related by the relation

$$D = \frac{\mathrm{LET}}{\rho}\,\phi \tag{5.5}$$

the inactivation cross section for each survival level $l$ can be expressed as

$$\sigma_l = \frac{\mathrm{LET}}{\rho}\sqrt{\alpha^2 - 4\beta \ln l} \tag{5.6}$$

The inactivation cross section depends therefore on the observed biological end point and, on the physical side, on the specific radiation quality used to irradiate the biological sample. If each hit target is inactivated by a single particle traversal, $\sigma$ approaches the geometrical cross section of the sensitive structure.

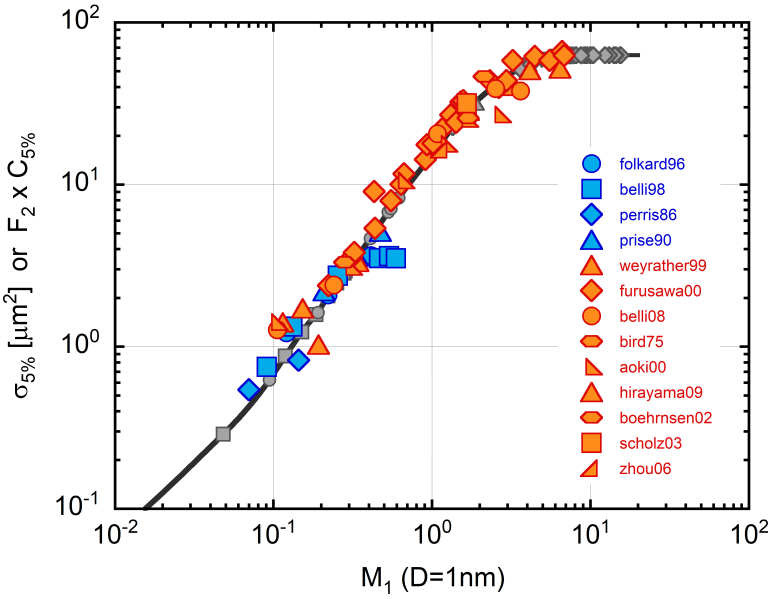


**Figure 5.1:** Comparison between $F_2$ and inactivation cross sections at 5% survival level for V79 cells, plotted as a function of the mean cluster size $M_1$ calculated in a volume of 1 nm. The grey symbols are the $F_2$ data reported in Figure 2.16 scaled by a constant factor, coloured symbols correspond to radiobiological data for irradiation with protons (blue) and carbon ions (orange). The literature sources for the biological data are listed in the Figure with the first author of the corresponding paper and the year of publication, as done in the PIDE database.

## 5.2 Comparison for the V79 cell line

In radiobiological modelling, the inactivation cross sections are generally plotted as a function of the incident LET. However, as discussed in the Introduction, LET is not descriptive of the fine structure of particle tracks: it would therefore be better to plot inactivation cross sections as a function of the mean ionization yield $M_1$ rather than LET. It is clear that $M_1$ depends both on radiation quality and on target size: the "relevant" size of the biological target must therefore be determined before significant nanodosimetric magnitudes can be measured. In other words, the track structure quantities become significant to characterize the biological effectiveness of ionizing particles only if they are measured in a volume of a well-defined size, determined as the one that offers the best correlation between physical $F_k$ and biological cross sections data. The quantitative determination of the relevant target size for each specific biological end point has been made by means of Monte Carlo simulations with the *MC-Startrack* code, calculating $M_1$ and $F_k$ in different site sizes for many radiation qualities, and then choosing the site size that optimized the correlation with biological effects.

For a first quantitative analysis of this correlation, the radio-resistant V79 cell line (Chinese hamster lung fibroblast) has been chosen, due to the huge amount of studies in which it was employed. The data were taken from the PIDE database, considering proton and carbon ion irradiation. Figure 5.1 presents a comparison between inactivation cross

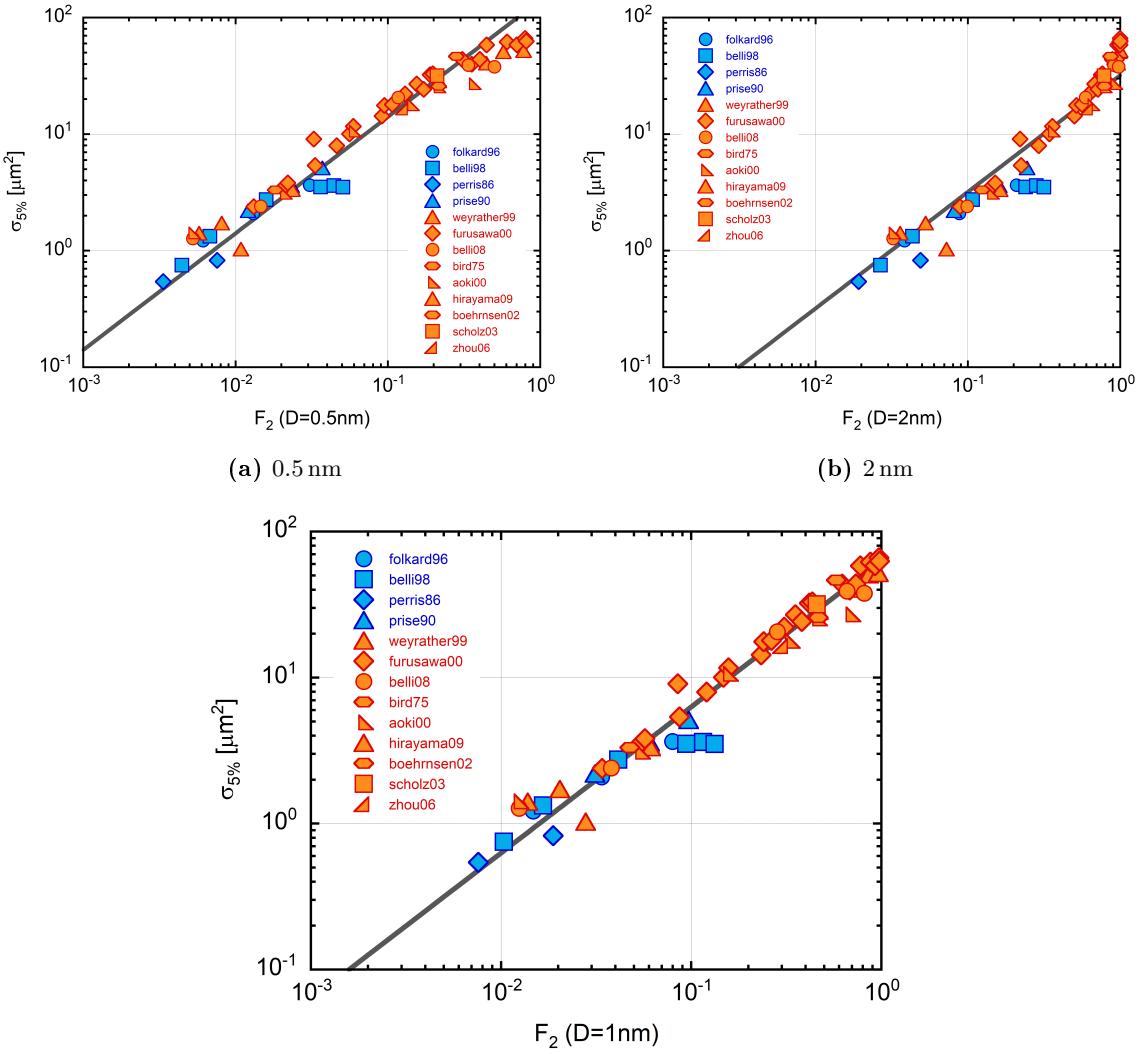


**(a)** 0.5 nm **(b)** 2 nm

**(c)** 1 nm

**Figure 5.2:** Inactivation cross sections at 5% survival level for V79 cells plotted as a function of $F_2$, calculated for volumes of different size: (a) 0.5 nm, (b) 2 nm, (c) 1 nm. Symbols correspond to radiobiological data for irradiation with protons (blue) and carbon ions (orange). The grey line is the best fit of the data points with a straight line through zero $y = mx$, carried out in the double-logarithmic representation. The literature sources for the biological data are listed in the Figure.

| $D$ [nm] | Prop. factor [$\mu$m$^2$] | Reduced $\chi^2$ | Pearson's $R$ |
|---|---|---|---|
| 0.5 | 141 ± 6 | 0.0221 | 0.9699 |
| 1.0 | 63 ± 2 | 0.0134 | 0.9819 |
| 2.0 | 32 ± 2 | 0.0291 | 0.9601 |

**Table 5.1:** Proportionality fit results of $\sigma_{5\%}$ as a function of $F_2$ for V79 cells, when $F_2$ is calculated in nanometric volumes of different size. The reduced $\chi^2$ and Pearson's correlation coefficients, calculated in the double-logarithmic representation, are also shown.

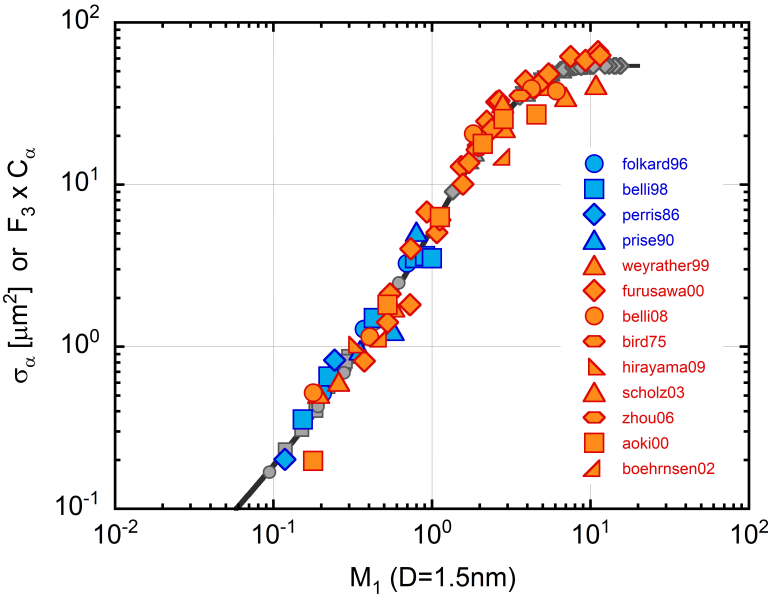


**Figure 5.3:** Comparison between $F_3$ and inactivation cross sections at initial survival level for V79 cells, plotted as a function of the mean cluster size $M_1$ in a volume of 1.5 nm. The grey symbols are the $F_3$ data reported in Figure 2.16 scaled by a constant factor; coloured symbols correspond to radiobiological data for irradiation with protons (blue) and carbon ions (orange). The cell survival experiments from which the biological data have been taken are the same as for the case of $\sigma_{5\%}$.

sections at 5% survival level for V79 cells and $F_2$ values, both plotted as a function of $M_1$ in a site size of 1 nm in liquid water. The $F_2$ values have been scaled by a constant factor $C_{5\%} = 63\,\mu m^2$, corresponding to the saturation level of the inactivation cross sections, which is related to the geometrical cross section of the nucleus of V79 cells. It can be seen that $F_2$ reproduces very well the trend of $\sigma_{5\%}$, if the site size in which $M_1$ is measured is equivalent to 1 nm in liquid water. For different site sizes the correlation worsens considerably, as shown in Figure 5.2 and Table 5.1[(2)]. At a site size of 1 nm, $\sigma_{5\%}$ and $F_2$ are instead proportional to each other.

In order to extend the study to a different biological end-point, Figure 5.3 presents a comparison between the inactivation cross section $\sigma_\alpha$ at low doses (100% survival) and $F_3$ values, again for V79 cells irradiated by protons or carbon ions. In this case, the correlation is optimized if $M_1$ is calculated in a volume of 1.5 nm, and the scaling factor applied to $F_3$ values is $C_\alpha = 54\,\mu m^2$. $F_3$ and $\sigma_\alpha$ are therefore proportional to each other if the site size in which $F_3$ is measured corresponds to 1.5 nm in liquid water. This is confirmed by the analysis of the correlation between $F_3$ and $\sigma_\alpha$ as a function of the site size, reported in Figure 5.4 and Table 5.2: maximum correlation is found for a sensitive volume size of 1.5 nm.

[(2)] The data reported in this Table and in the following ones are the results of unweighted least square fits carried out in the double-logarithmic representation. The reduced $\chi^2$ coincides therefore with the sum of square residuals divided by the number of degrees of freedom.

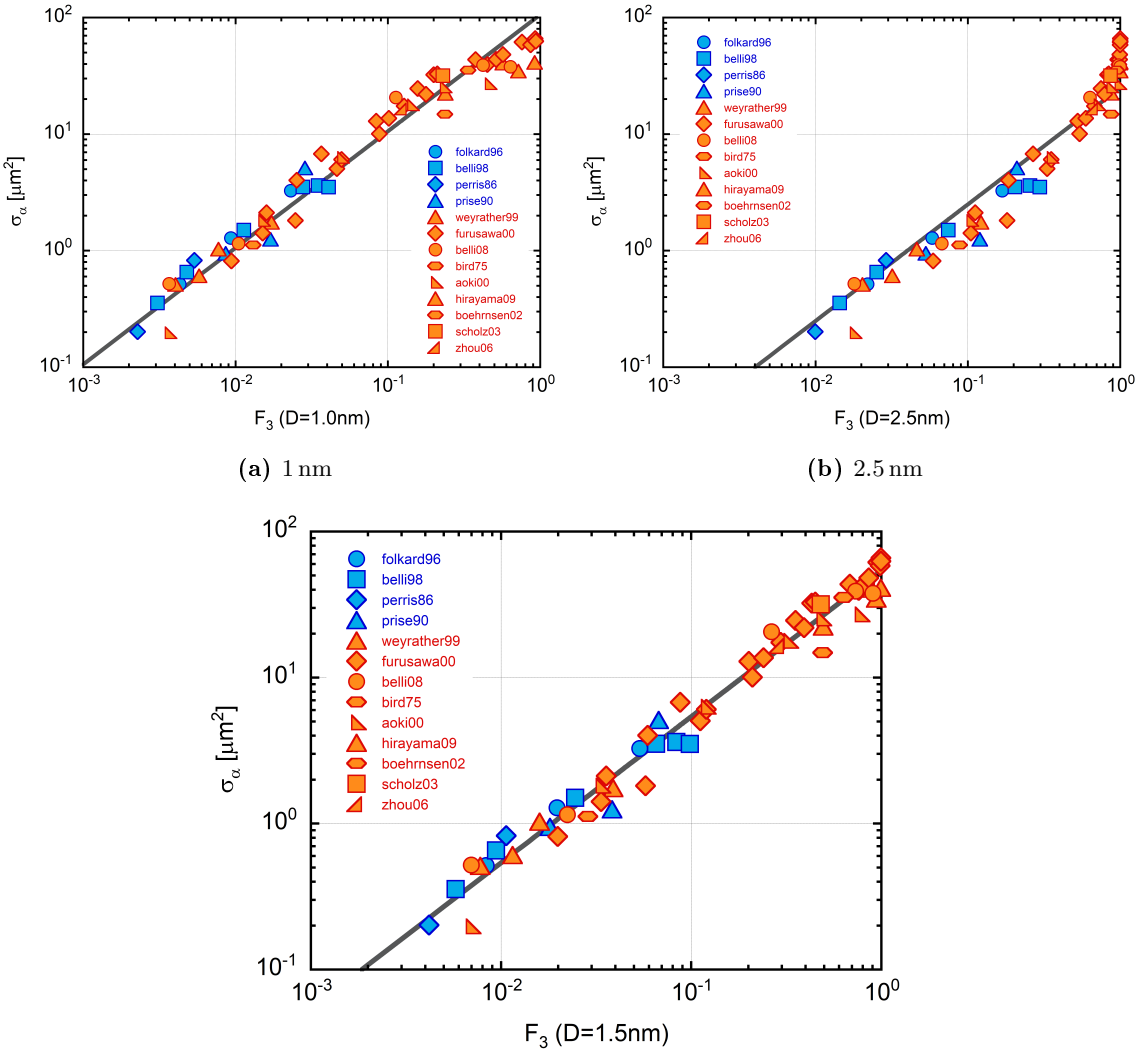


**(a)** 1 nm **(b)** 2.5 nm

**(c)** 1.5 nm

**Figure 5.4:** Inactivation cross sections at initial survival for V79 cells as a function of $F_3$, calculated for volumes of different size: (a) 1 nm, (b) 2.5 nm, (c) 1.5 nm. Symbols correspond to radiobiological data for irradiation with protons (blue) and carbon ions (orange). The grey line is the best fit of the data points with a straight line through zero $y = mx$, carried out in the double-logarithmic representation.

| $D$ [nm] | Prop. factor [$\mu$m$^2$] | Reduced $\chi^2$ | Pearson's $R$ |
|---|---|---|---|
| 1.0 | 106 ± 5 | 0.0214 | 0.9804 |
| 1.5 | 54 ± 2 | 0.0117 | 0.9894 |
| 2.5 | 25 ± 1 | 0.0398 | 0.9633 |

**Table 5.2:** Proportionality fit results of $\sigma_\alpha$ as a function of $F_3$ for V79 cells, when $F_3$ is calculated in nanometric volumes of different size. The reduced $\chi^2$ and Pearson's correlation coefficients, calculated in the double-logarithmic representation, are also shown.

## 5.3 Comparison for other cell lines

The study was then extended to other radio-resistant cell lines, in particular, the Chinese Hamster Ovary cells (CHO), the Human Salivary Gland cells (HSG) and the human T1 lymphoblast cells, under irradiation of protons and carbon ions, considering again the cases of 5% survival level (high doses) and initial survival (low doses). The results are reported in Figure 5.5: also for these cell lines the correlation is optimized if a site size of 1 nm is considered for $F_2$, and one of 1.5 nm for $F_3$, confirming the validity of the model independently of the specific cell line. The proportionality coefficients between $\sigma_{5\%}$ and $F_2$ and $\sigma_\alpha$ and $F_3$, which are reported in Table 5.3, are instead dependent on the type of cells, due to the different saturation level of the inactivation cross sections.

A strong correlation seems therefore to be present between radiobiological cross sections at different survival levels and nanodosimetric measurements in specific site sizes, if repair-proficient cell lines are considered. In particular, the probability $F_2$ of measuring two or more ionizations within a volume of 1 nm is proportional to the inactivation cross section at high doses, while $F_3$ measured in a volume of 1.5 nm is proportional to the inactivation probability at low doses. An intuitive first idea about a possible reason for this can be that in the latter case the repair mechanisms for DNA damage are still effective, while in the former they are saturated; a bigger ionization cluster is therefore needed in the first case to produce a non-repairable damage than in the second one.

The consistency of this idea is confirmed by the analysis of the inactivation cross section for the XRS5 cell line, a radio-sensitive mutant of the CHO cell line which shows a reduced repair capability for DNA double strand breaks. For these cells, the survival curve is a straight line in a semi-logarithmic plot and the inactivation cross section $\sigma$ is the same for all survival levels. The result of the comparison with nanodosimetric data is shown in Figure 5.6: it can be seen that $\sigma$ is proportional to $F_1$, measured in a volume of 0.3 nm. For this radio-sensitive cell line, a smaller ionization cluster seems therefore related to a non-repairable damage than for cells which are proficient in DNA repair, even if the number of radiobiological data points is small and does not allow a full validation of this hypothesis. The much smaller target size which optimizes the correlation is somewhat surprising; however, the concept of a characteristic distance between neighbouring ionizing events loses part of its meaning when a single ionization is enough to produce a non-repairable damage. The much higher proportionality coefficient ($C_{XRS5} = 190\,\mu\mathrm{m}^2$) is instead due to the higher probability of inactivation for the XRS5 cell line compared to other radio-resistant cells irradiated with the same radiation quality.

| **Cell line** | **5% survival** | | | **initial survival** | | |
|---|---|---|---|---|---|---|
| | $C_{5\%}$ | **Red.** $\chi^2$ | **Pearson's** $R$ | $C_\alpha$ | **Red.** $\chi^2$ | **Pearson's** $R$ |
| CHO | 74 ± 4 | 0.0152 | 0.9796 | 68 ± 4 | 0.0179 | 0.9797 |
| HSG | 92 ± 3 | 0.00301 | 0.9926 | 72 ± 5 | 0.0160 | 0.9817 |
| T1 | 92 ± 5 | 0.0116 | 0.9793 | 49 ± 4 | 0.0351 | 0.9551 |

**Table 5.3:** Proportionality coefficients between $\sigma_{5\%}$ and $F_2$ and $\sigma_\alpha$ and $F_3$ for the CHO, HSG and T1 cell lines, considering a target size of 1 nm for the case of $\sigma_{5\%}$ and of 1.5 nm for $\sigma_\alpha$. The reduced $\chi^2$ and Pearson's correlation coefficients, calculated in the double-logarithmic representation, are also shown.

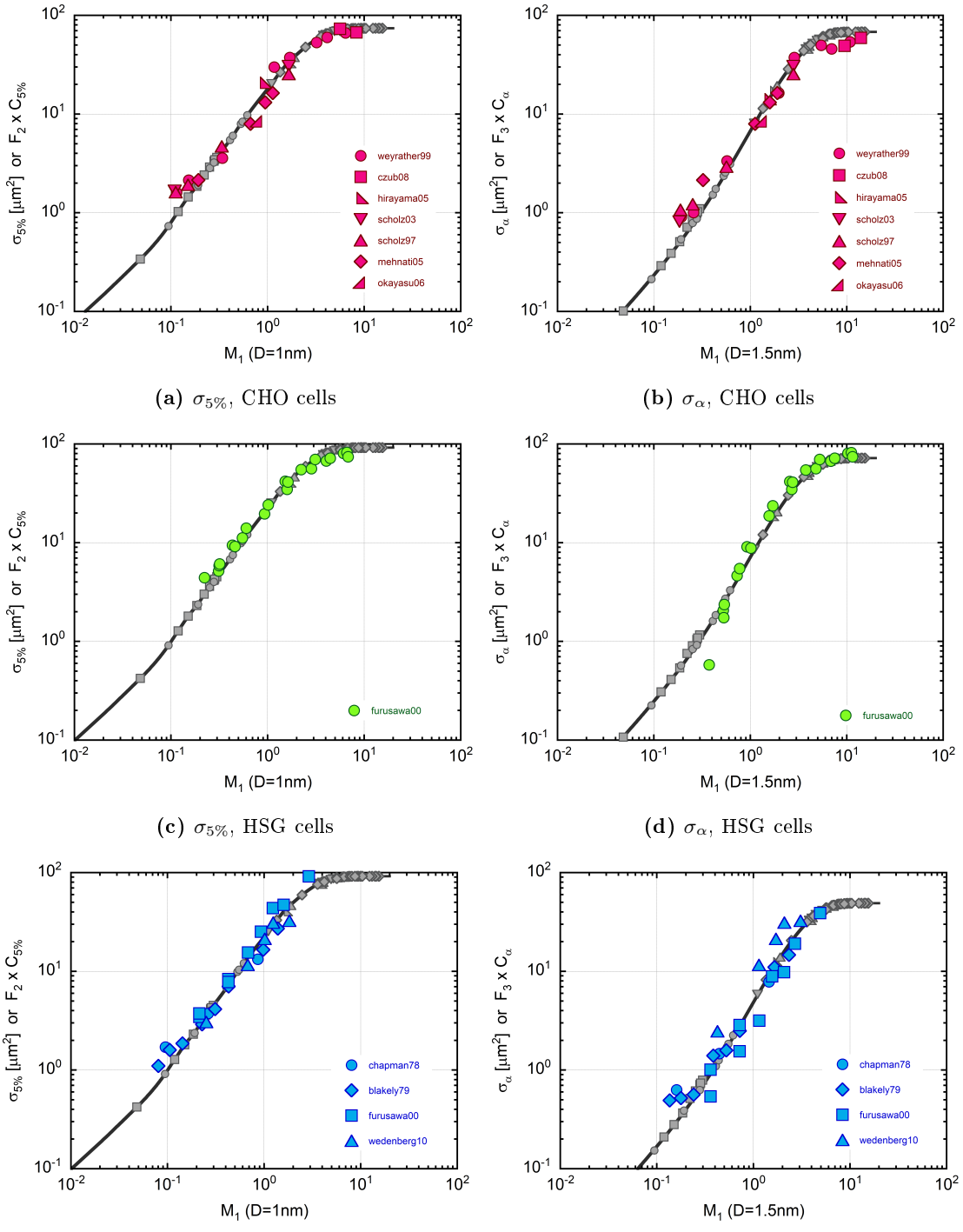


**(a)** $\sigma_{5\%}$, CHO cells

**(b)** $\sigma_{\alpha}$, CHO cells

**(c)** $\sigma_{5\%}$, HSG cells

**(d)** $\sigma_{\alpha}$, HSG cells

**(e)** $\sigma_{5\%}$, T1 cells

**(f)** $\sigma_{\alpha}$, T1 cells

**Figure 5.5:** Comparison between inactivation cross sections at 5% and initial survival level and experimental values of $F_2$ and $F_3$, for different cell lines: (a) CHO cells, 5% survival, (b) CHO cells, initial survival, (c) HSG cells, 5% survival, (d) HSG cells, initial survival, (e) T1 cells, 5% survival, (f) T1 cells, initial survival. The grey symbols are the $F_2$ or $F_3$ data reported in Figure 2.16 scaled by a constant factor; coloured symbols correspond to inactivation cross sections calculated in a volume 1 nm in size for the case of 5% survival, and 1.5 nm in size for the case of initial survival. The literature sources for each cell line are given in the Figure.

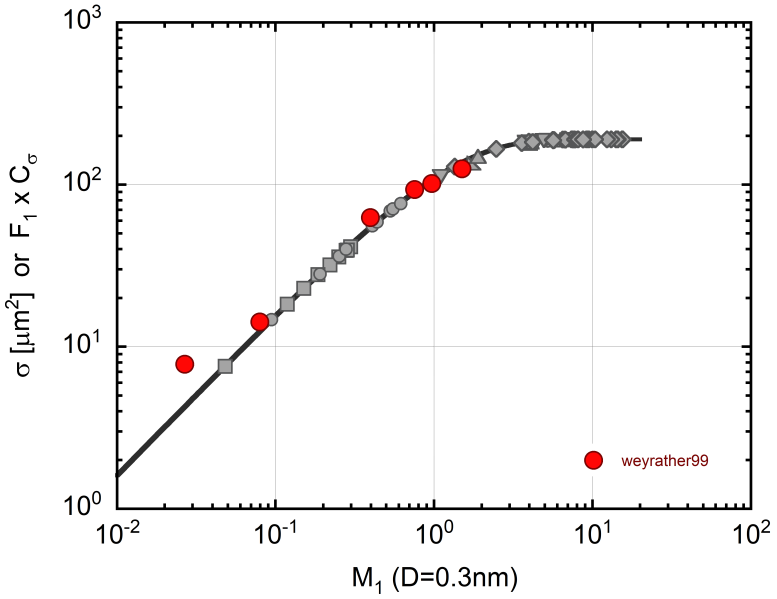


**Figure 5.6:** Comparison between inactivation cross sections for the radio-sensitive cell line XRS5 and the values of $F_1$, plotted as a function of the mean cluster size $M_1$ in a volume of 0.3 nm. The grey symbols are the $F_1$ data reported in Figure 2.16 scaled by a constant factor; red symbols correspond to inactivation cross sections. The literature source for these data is given in the Figure.

## 5.4 Nanodosimetric modelling of cell survival curves

The direct proportionality between $F_2$ and $\sigma_{5\%}$ and $F_3$ and $\sigma_\alpha$ allows to calculate the $\alpha$ and $\beta$ parameters of the linear-quadratic dose response model, through the following equations, which follow directly from the definitions of $\sigma_{5\%}$ and $\sigma_\alpha$:

$$\begin{aligned} \alpha(Q) &= C_\alpha F_3(Q)\frac{\phi}{D} \\ \beta(Q) &= \frac{[C_\alpha F_3(Q)]^2 - [C_{5\%} F_2(Q)]^2}{4\ln 0.05}\left(\frac{\phi}{D}\right)^2 \end{aligned} \tag{5.7}$$

Here, $\phi$ is the particle fluence and $D$ is the corresponding absorbed dose. To determine the values of the proportionality factors $C_\alpha$ and $C_{5\%}$ for any given biological system, a precise and reproducible calibration procedure should be defined.

In radiobiological campaigns reference measurement are generally carried out by exposing cells to photon fields. Although there is evidence that nominally low-LET radiations have different effects on cells (Hunter, 2009) both 250 kV X-rays and $^{60}$Co $\gamma$-rays are alternatively used as reference radiation, assuming an RBE value of 1 for X-rays, $\gamma$-rays and high-energy electrons. On the other hand, the RBE of carbon ions used in radiotherapy increases to about 3.

In order to calibrate nanodosimetric measurements on radiobiological ones, the parameters of the linear-quadratic fit of the survival curve obtained for the reference photon field can be used to calculate $C_\alpha$ and $C_{5\%}$; after this calibration, the values of $F_2$ and $F_3$ mea-

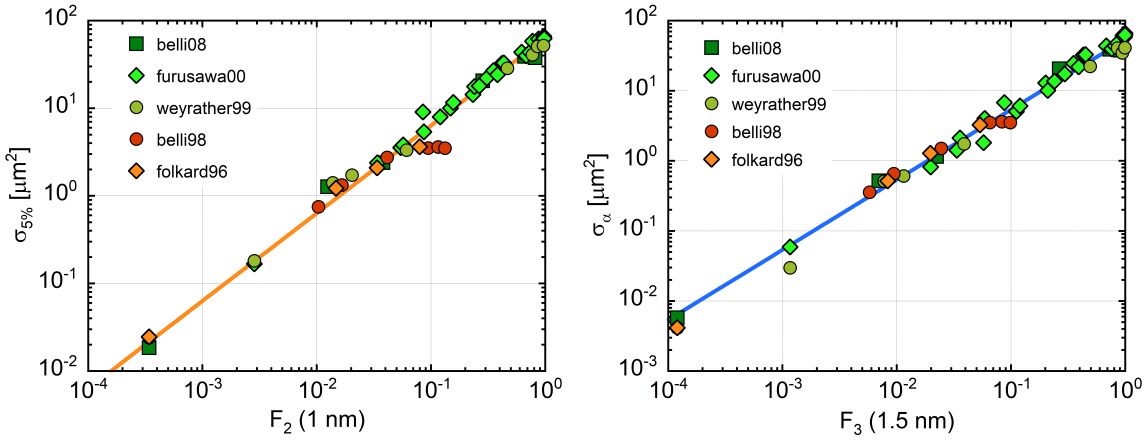


**(a)** 5% survival **(b)** initial survival

**Figure 5.7:** Calibration of the nanodosimetric data on radiobiological ones for photon reference fields, in order to determine the corresponding $F_k$ values: (a) inactivation cross sections at 5% survival level as a function of $F_2$ in a volume of 1 nm, giving a calibration factor $C_{5\%} = 63\,\mu\text{m}^2$ (orange line), (b) inactivation cross section at initial survival as a function of $F_3$ in a volume of 1.5 nm, giving a calibration factor $C_\alpha = 54\,\mu\text{m}^2$ (blue line). The corresponding photon $F_k$ data are reported in Table 5.4; the literature sources for the biological data are given in the Figure.

| **Radiation field** | **LET [keV/$\mu$m$^2$]** | $F_2(D = 1\,\text{nm})$ | $F_3(D = 1.5\,\text{nm})$ |
|---|---|---|---|
| $^{60}$Co $\gamma$-rays | 0.2 | 0.00034091 | 0.00012000 |
| 250 kV X-rays | 2 | 0.0028500 | 0.0011672 |

**Table 5.4:** Values of $F_2$ and $F_3$ recommended for the calibration of nanodosimetric data on radiobiological ones, for two common reference radiation fields: $^{60}$Co $\gamma$-rays and 250 kV X-rays.

sured in different radiation fields allow the calculation of the $\alpha$ and $\beta$ parameters of the linear quadratic model for the cell line under analysis by means of Eq. 5.7, and therefore the prediction of cell survival curves for any radiation quality.

The two photon fields commonly used as reference radiation correspond to LET values of approximately 2 keV/$\mu$m for 250 kV X-rays, and 0.2 keV/$\mu$m for $^{60}$Co $\gamma$-rays (ICRU, 1970). From a comparison of the radiobiological and the nanodosimetric data for a limited set of literature references (reported in Figure 5.7), the values reported in Table 5.4 are recommended for calibration on $\gamma$-rays or 250 kV X-rays.

However it should be observed that survival data for exposure to photon fields are often affected by large uncertainties. As an example, Figure 5.8 shows the inactivation cross sections for V79 cells irradiated by protons at different energies, measured by different groups (Belli, 1998; Folkard, 1996). In this case, the linear-quadratic fitting of the survival curve for reference radiation ($\gamma$-rays from a $^{60}$Co source) resulted in an almost identical inactivation cross section, and the calibration of nanodosimetric data on the cross section for photon irradiation gives a factor $C_{5\%} = \sigma_{5\%}/F_2 = 71\,\mu\text{m}^2$. The function $C_{5\%}F_2$ is represented by the grey line in Figure 5.8. The data from Belli on the right side of the Figure

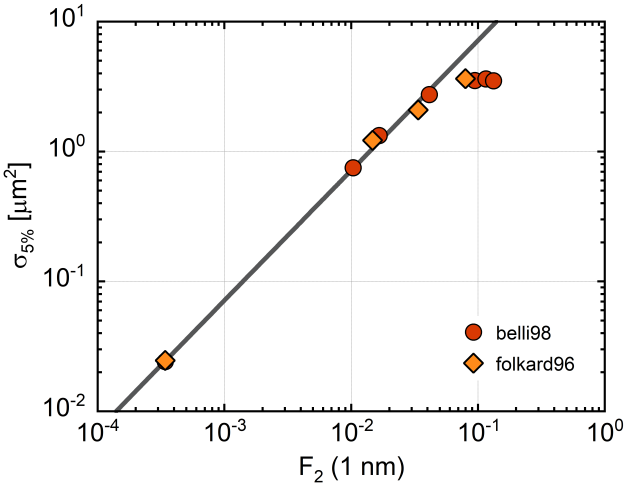


**Figure 5.8:** Calibration of the nanodosimetric data on radiobiological ones for photon reference fields, considering the data of Belli (Belli, 1998) and Folkard (Folkard, 1996).

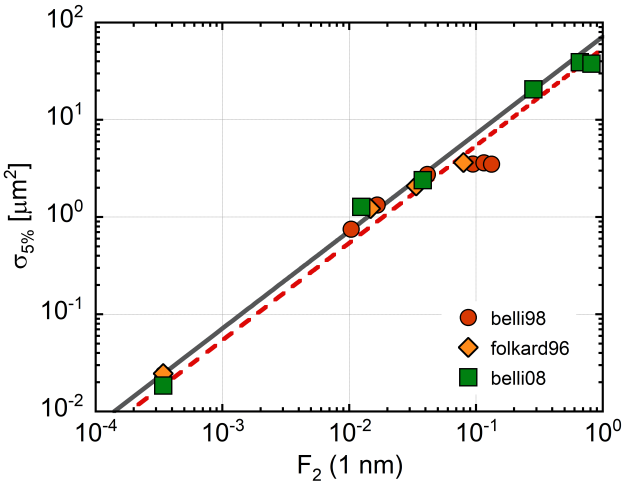


**Figure 5.9:** Comparison between the calibration factor obtained from the photon reference data of Belli (Belli, 1998) and Folkard (Folkard, 1996) during proton irradiation campaigns (grey continuous line), and that obtained from the reference data of Belli (Belli, 2008) in a different measurement campaign with carbon ions (red dashed line).

are significantly lower than the corresponding values predicted by nanodosimetry, but they were not confirmed by other authors (see Figure 5.1). However, apart from data measured for very slow protons, which are critical themselves and affected by large uncertainties, the effectiveness of higher-energy protons is generally well predicted by nanodosimetry, after calibration on the reference $^{60}$Co gamma field.

Unfortunately this is not always the case. In Figure 5.9 the inactivation cross sections for the same V79 cell line irradiated with carbon ions are also shown, together with the result for the reference field. In this case the cross section for $^{60}$Co irradiation was smaller

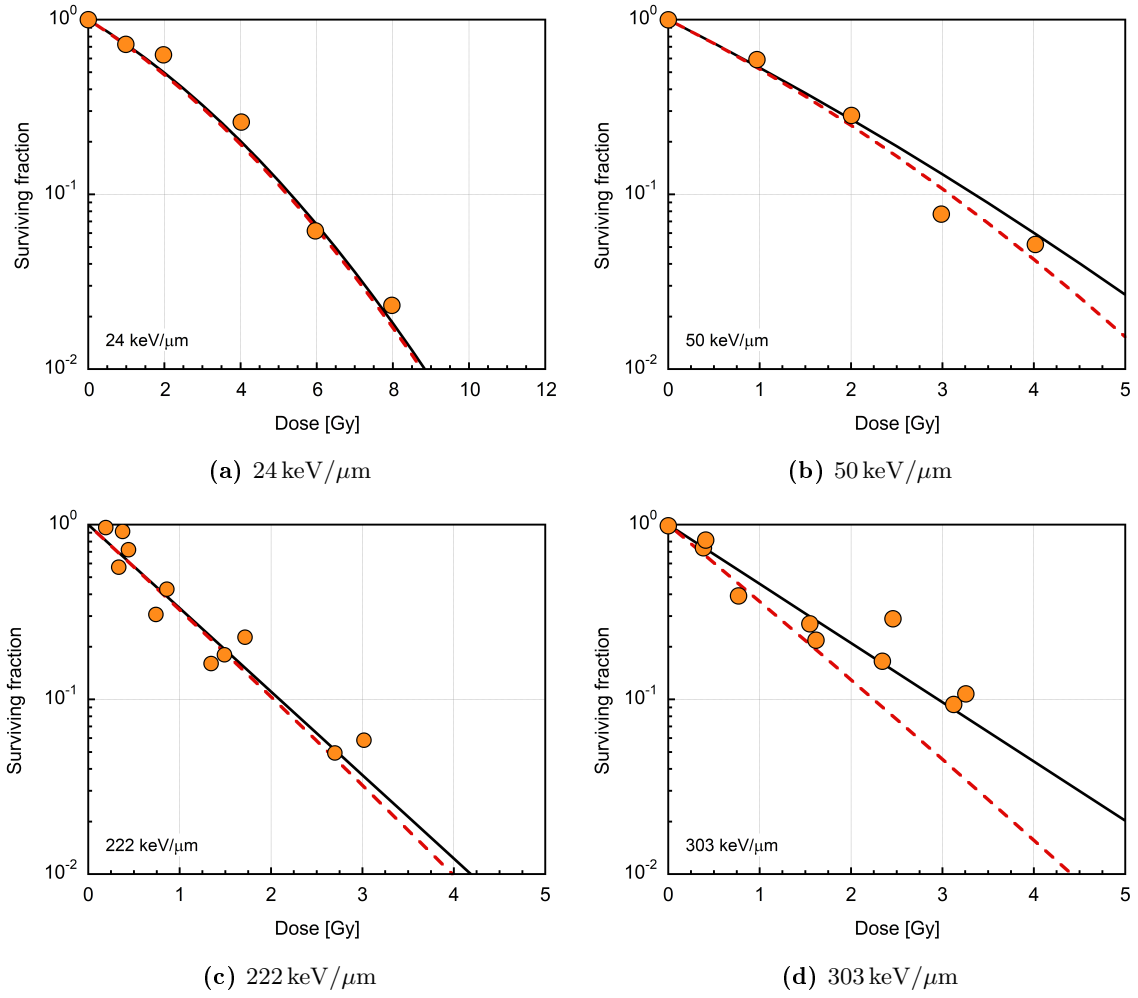


**(a)** 24 keV/$\mu$m **(b)** 50 keV/$\mu$m

**(c)** 222 keV/$\mu$m **(d)** 303 keV/$\mu$m

**Figure 5.10:** Comparison between cell survival curves derived from radiobiological experiments (Belli, 2008) and those calculated from nanodosimetric values of $F_2$ and $F_3$, considering carbon ions of different LET.

than in the case of the proton measurement campaign. However, the data for carbon ion irradiation lie almost on the same curve as the proton ones, without a significant shift to lower values. If the nanodosimetric quantity $F_2$ is calibrated on the cross section for photon irradiation obtained in the measurement campaign with carbon ions, the predicted nanodosimetric values lie on the red dashed line of Figure 5.9 ($C_{5\%} = 54\,\mu\text{m}^2$). It is clear that the choice of the calibration value is critical and should be performed carefully.

To give an example of the application of the suggested procedure and its limits, Figure 5.10 shows a comparison between survival curves derived from radiobiological experiments and calculated from nanodosimetric magnitudes, for V79 cells irradiated with carbon ions at four different incident LET values. Nanodosimetric survival curves were calculated with $C_{5\%} = 63\,\mu\text{m}^2$ and $C_\alpha = 54\,\mu\text{m}^2$, *i.e.* the best-fit values obtained in Section 5.2. It can be observed that, at least in these cases, the agreement between radiobiological sur-

vival curves (obtained by best fitting of the linear-quadratic equation) and nanodosimetric survival curves (uniquely determined by $F_2$ and $F_3$ after proper calibration on photons reference fields) is very satisfactory in most cases.

This preliminary study needs to be further extended to other radiation qualities and cell lines, in order to assess its reliability for the determination of survival curves. However, if these findings are confirmed, they could be the basis for a new definition of the radiation quality by means of nanodosimetric measurements.

# Chapter 6

# Towards a portable nanodosimeter

In the previous Chapters, it has been shown that specific track structure descriptors can be derived from measurements of the ionization yield in volumes of equivalent nanometric size, which are closely related to biological effects at cellular level. In particular, unique relations are found between the values of the complementary cumulative distribution function $F_k$ and the mean ionization yield $M_1$, regardless of the specific radiation quality, the sensitive volume size and the specific operating conditions of the nanodosimeter. Moreover, it has been found that the values of $F_k$ for different values of $k$ are directly proportional to inactivation cross sections for different biological end-points: if radio-resistant cell lines are considered, the cross section for 5% survival at high doses is proportional to $F_2$, while that for initial survival at low doses is proportional to $F_3$. For repair-deficient cells, the cross section is the same for all survival levels and is proportional to $F_1$.

After the nanodosimetric data are calibrated on the specific cell line under analysis using a reference radiation quality, the response of the cell in different radiation fields can be predicted from measurements of $F_2$ and $F_3$, which are directly proportional to $\sigma_{5\%}$ and $\sigma_\alpha$. The $\alpha$ and $\beta$ parameters of the linear-quadratic model can then be calculated, allowing the reconstruction of the cell survival curve.

The nanodosimetric description of track structure is therefore a promising candidate to build a new concept of radiation quality, measurement-based and directly correlated to biological effects. This could be of interest for applications in both radiation therapy and radiation protection, where clonogenic assays are routinely used as the golden standard for the assessment of radiation effects, in order to shorten the time needed for the experiment and remove the source of uncertainty due to biological variability. However, the three nanodosimeters which have been built up to date are very complex and bulky, and consequently not suited for the everyday use required, for instance, in radiotherapy or radiation protection applications. This problem could be overcome with the development of a simplified, portable nanodosimeter, able to analyse significant features of particle track structure at the nanometre level. A possible way to build such a device seems to be the use of nano-structured technology, in which nanoparticles that are sensitive to ionizing radiation are dispersed in a given volume of tissue-equivalent material.

In order to investigate if the simplified track structure description that could be obtained from such a device is still meaningful for the estimation of biological effects, a proof-of-principle study has been carried out by means of Monte Carlo simulations. A

simulation tool has been developed for this purpose, based on the physical models of the GEANT4-DNA track structure code. After an introduction of the physical models on which this toolkit is based, this Chapter discusses the structure of the simulation setup and presents results for two different cases of tracking choices, which are then discussed in order to assess the suitability of such a detector concept for the estimation of radiation effects.

## 6.1 The GEANT4-DNA code

The GEANT4-DNA toolkit was originally developed in collaboration with the European Space Agency (Incerti, 2010a) to extend the modelling capability of the GEANT4 toolkit down to the 10-eV energy range, for radiobiology and radioprotection applications. It is an open-source, regularly-maintained sub-library of GEANT4, in which it is fully integrated. It includes also a chemistry module for the simulation of water radiolysis and diffusion of free radicals, and various geometrical models of different DNA organizational levels, including a full atomistic approach, in order to study yields of DNA strand breaks and base oxidations (Incerti, 2016). Its main disadvantage is that the physical models are valid for liquid water only.

Models are defined for electrons, protons and alpha particles, including their charge states (*i.e.*, neutral hydrogen, neutral helium and singly-charged helium). Gamma interactions are also defined by means of the low-energy electromagnetic models of the GEANT4 toolkit (the so-called *Livermore* models), which are validated down to a threshold energy of 250 eV (GEANT4, Physics Reference Manual). Some ions heavier than helium are also considered. For each process, one or more models are implemented; these models can cover different energy ranges or be alternatives for the same one. The choice of the best model for each specific application is the responsibility of the user, however, default models are defined, which are described in the following.

For electrons, elastic scattering, atomic and vibrational excitations, ionization and electron attachment are modelled. The treatment of ionization and excitations is based on a dielectric response function determined according to (Emfietzoglou, 2003), modified in part in order to improve agreement with experimental $W$-values (Kyriakou, 2015). Four "outer" ionization shells, one "inner" ionization shell (the K-shell of oxygen), and five discrete excitation levels are considered. The energy-differential and total cross sections are calculated in the Born approximation, including some perturbation corrections at energy below 1 keV and relativistic corrections at energies above 10 keV. Both after an ionization and an excitation event, the polar and azimuthal angle of the ejected electrons are calculated using the same algorithm as the one implemented in *MC-Startrack*.

Cross sections for vibrational excitations up to an energy of 100 eV are derived from experimental data on ice films (Michaud, 2003); electron attachment is modelled in the energy range between 4 and 13 eV according to the data of (Melton, 1972). Elastic collisions can be treated according to two different models: one is a theoretical calculation based on a central potential and a partial-wave decomposition (Champion, 2009), the other is based on a screened Rutherford cross section similar to the one implemented in *MC-Startrack*, but with a different parametrization for the screening parameter. At energies below 200 eV, this second model is replaced by the formula proposed by (Brenner, 1983), in order to improve

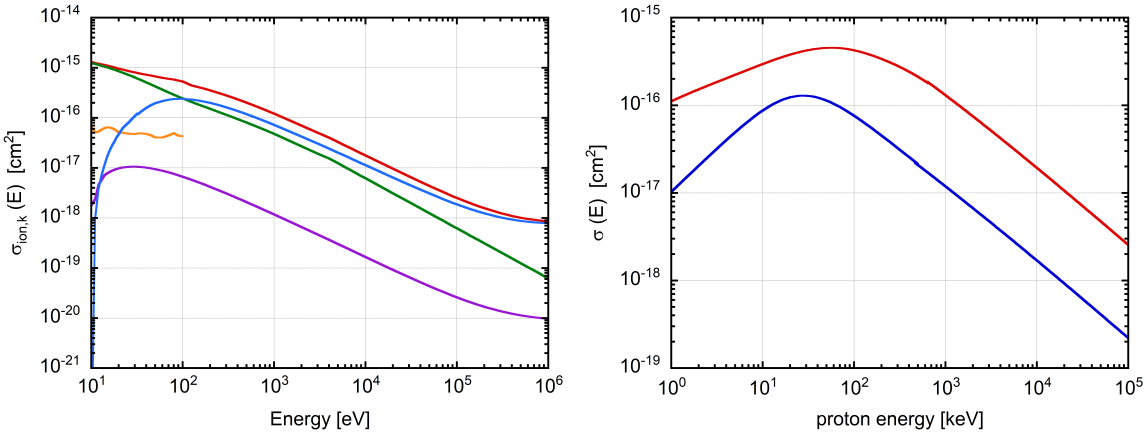


**(a)** **(b)**

**Figure 6.1:** (a) Electron-impact cross sections implemented in GEANT4-DNA: total scattering cross section (red), cross section for elastic scattering (green), atomic excitations (violet), vibrational excitations (orange) and ionizations (blue). Excitation and ionization cross sections are summed over all the sub-shells. The cross sections for vibrational excitations are defined up to a maximum energy of 100 eV. (b) Cross section for excitations (blue) and ionizations (red) due to proton impact.

agreement with experimental data. For a detailed description of electron interactions, the reader is referred to (Kyriakou, 2015). The general trend of GEANT4-DNA electron-impact cross sections is shown in Figure 6.1(a).

For protons, alpha particles, and their charge states, the processes which are implemented are ionization, electronic excitation, elastic scattering and electron capture and loss. Ionizations cross sections are derived from the Rudd model (Rudd, 1992), similarly to the case of *MC-Startrack*; the empirical parameters were modified in order to adapt them to the liquid phase (Dingfelder, 2000). Excitation is modelled according to Miller and Green (Miller, 1973), using a speed scaling from the electron excitation cross section. For alpha particles and helium ions, the cross section are derived from those for protons by means of a speed scaling procedure which takes into account the effective charge of the incident particle, in an analogous way to the case of *MC-Startrack*. For fast protons only (energy above 500 keV), a complementary model for the treatment of excitations and ionizations is defined, which uses the first Born approximation and the dielectric formalism for liquid water, including some corrections to take into account the polarization of the medium and relativistic effects. The cross sections for excitation and ionization due to proton impact are reported in Figure 6.1(b).

Electron loss and capture are modelled according to the semi-empirical models of Dingfelder (Dingfelder, 2000; Dingfelder, 2005), obtained by analytical fitting of experimental cross section data for water vapour. Elastic scattering is modelled using a classical approach based on a screened Coulomb potential (Tran, 2015); the screening functions are derived from (ICRU, 1993) for protons and from (Ziegler, 1985) for $\alpha$ particles. For a detailed description of protons and $\alpha$-particle processes, see (Incerti, 2010b).

Some ions heavier than helium are also considered, namely $^7$Li, $^9$Be, $^{11}$B, $^{12}$C, $^{14}$N,

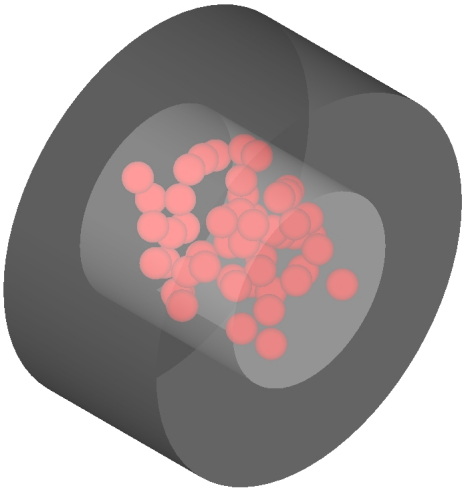

**Figure 6.2:** Geometry of the simulated setup. The sensitive spheres are shown in red in the Figure. The direction of incidence of the primary beam is parallel to the central axis of the two cylinders.

$^{16}$O, $^{28}$Si and $^{56}$Fe. For these ions, only ionization processes are modelled, for energies above 0.5 MeV/u. The treatment is based on the Rudd model, using a speed scaling which takes into account the effective charge of the ion (Francis, 2012). A relativistic correction is included for higher energies.

## 6.2 Description of the simulated setup

The detecting setup which is modelled in the simulation is composed of two coaxial cylinders, which lie with their main axis parallel to the direction of incidence of the primary particle beam. In the inner cylinder, a set of nanometre-sized spheres is embedded, which represent the radiation-sensitive targets. These spheres are randomly distributed inside the inner cylinder, with the only constraint of no overlapping. The dimensions of the inner cylinder have been kept fixed to 20 nm for both length and diameter; for the outer one, the same height of 20 nm is considered, while the diameter has been enlarged to 40 nm. This has been done in order to reduce border effects due to energetic secondary electrons which could escape the inner cylinder. In practice, such a detector could be realized, for instance, by dispersing a certain number of quantum dots in a PMMA layer.

The cylinders are irradiated by a circular homogeneous beam of diameter $D_b$ equal to 20 nm, centred on the main axis of the cylinders. Its cross section coincides with that of the inner cylinder, and the initial direction of the primary particles is parallel to the central axis. Since in Geant4-DNA the interaction cross sections are implemented for liquid water only, all the elements of the simulated setup are made of this material, however, there is the possibility to define a different density value for each element of the setup. A picture of the geometry implemented in the simulation is shown in Figure 6.2.

Gas-based nanodosimeters measure the frequency distribution of the number of ionizations produced by primary particles inside a sensitive volume of millimetric size filled with a low-density gas, which is considered equivalent to a nanometric volume at unit density

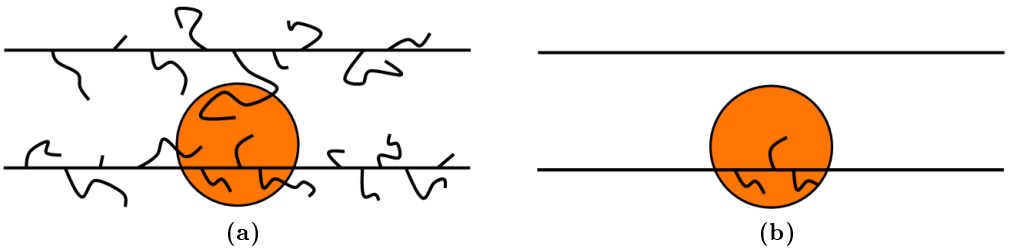


**Figure 6.3:** Pictorial representation of the two different tracking configurations which have been considered: (a) full simulation of the secondary electron tracks, (b) simulation of the secondary electron tracks originated inside the sensitive spheres only, up to the geometrical boundary of the target of production.

based on the equality of their mass thickness. However, the experimental determination of the exact number of ionizations inside a solid volume of nanometric size (for instance inside a quantum dot) could be hardly feasible. In order to deal with this situation and to simplify the track structure description, an alternative possibility was investigated in this study, under the hypothesis that each sphere is able to give a detectable signal if at least a minimum number $k$ of ionizations takes place inside it. A sphere is therefore considered "hit" if the number of ionizations it measures is greater than or equal to a pre-defined threshold value $k$, representing the sensitivity of each detector.

During the simulations, the number of ionizations within each target at the passage of each primary ion is recorded, and used to calculate both the ionization cluster size distributions for each sensitive sphere and the frequency distribution of the number of "hit" targets, by normalising on the total number of incident ions. The features of these distributions are then compared and analysed as a function of both the radiation quality and the geometrical parameters of the setup, such as the number $N_t$ of sensitive spheres, their diameter $D_t$, and the threshold value $k$. Primary beams of protons and carbon ions are considered, in an energy range from 1 to 60 MeV and 0.5 to 400 MeV/u respectively, corresponding to an LET range from 1 to 1000 keV/$\mu$m. The number of sensitive spheres varies between 20 and 100 and their diameter spans the range between 1 nm and 3 nm. Threshold values of 1, 2 and 3 are analysed.

Two different tracking options are considered for each radiation quality and geometrical configuration: in the first, all secondary electron tracks are simulated until they become non-ionizing or escape the setup boundaries; in the second, only the electron tracks originated inside the detecting spheres are simulated, and they are terminated as soon as they leave the volume of their production. A pictorial representation of these two tracking configurations is reported in Figure 6.3. The aim of simulations performed in this second modality is to separate the effect of secondary electrons from that of primary particles, in order to study only the effect of the track-core region or that of the full penumbra.

## 6.3 Study of border effects

In order to check the consistency of the results of these simulations with nanodosimetric data for a broad beam geometry, Figure 6.4 presents the ionization cluster-size distributions $P_\nu^{(i)}(Q)$ produced by incident carbon ions at an energy of 240 MeV inside each sensitive

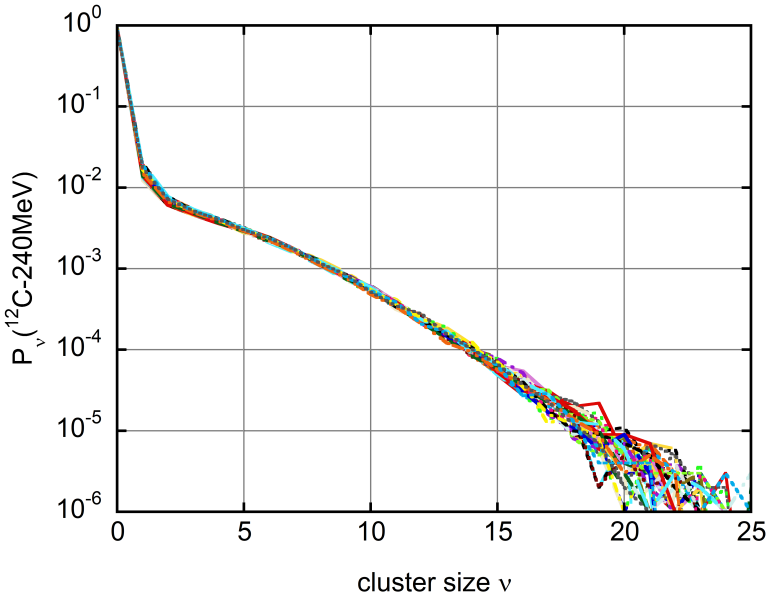


**Figure 6.4:** Probability distribution $P_\nu^{(i)}$ of the number $\nu$ of ionization events in each of the detecting spheres, for an incident beam of 240-MeV carbon ions and a configuration with 50 targets 3 nm in diameter.

volume $(i)$, for a target configuration with 50 detectors 3 nm in diameter, in the case where all secondary electron tracks are simulated. The shape of the distributions is consistent with what is expected for a single nanometric volume irradiated by a homogeneous broad beam (Conte, 2015), moreover, it is very similar for all the spheres regardless of their specific position with respect to the target border and the particle beam. However, some differences are present, in particular at small cluster sizes. These are due to two different effects:

- Since the primary ion trajectories are restricted to the inner cylinder, the target spheres located close to the radial border will score less ionizations than targets near the central axis, because of the lack of secondary electrons coming from the penumbra of primary ions outside the inner cylinder.

- The absence of a build-up layer in front of the cylinders and of a backscattering one at their end enhances the probability of secondary electron escape. Because of this, targets located close to the front and back surface will score less ionizations than those located near the middle plane.

The result of both these effects is that a gradient of ionization density is present in the cylinder if the full penumbra of secondary electrons is simulated, so that target spheres located close to the border will score less ionizations than those located near the centre. This is shown in Figure 6.5: the value of $P_1$ near the centre is much higher than near the border, explaining the differences in the cluster size distributions. The amount of these differences is higher for densely-ionizing particles, and is particularly relevant for small

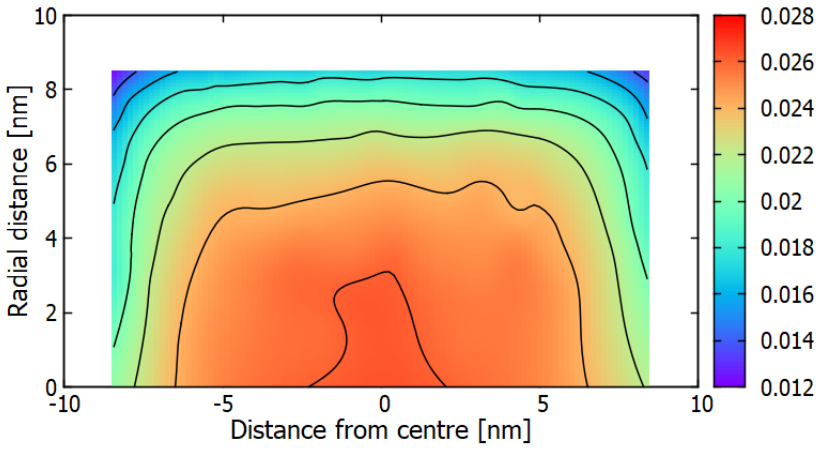


**Figure 6.5:** Colour-coded plot of the value of $P_1^{(i)}$ as a function of the spatial position inside the inner cylinder. The calculation is done for 240-MeV carbon ions and a configuration with 100 spheres 3 nm in diameter.

| Primary ion | $P_0$ | $P_1$ | $P_2$ | $P_3$ | $P_4$ | $F_1$ | $F_2$ | $F_3$ |
|---|---|---|---|---|---|---|---|---|
| $^{1}$H, 20 MeV | 0.0% | 4.3% | 3.7% | 5.7% | 6.6% | 4.3% | 4.5% | 6.1% |
| $^{4}$He, 80 MeV | 0.0% | 4.3% | 3.9% | 6.6% | 6.8% | 4.1% | 4.2% | 5.8% |
| $^{12}$C, 240 MeV | 0.3% | 12.4% | 7.2% | 5.0% | 4.0% | 7.4% | 4.2% | 3.3% |
| $^{12}$C, 150 MeV | 0.5% | 14.0% | 10.5% | 7.8% | 6.0% | 8.7% | 5.4% | 3.9% |
| $^{12}$C, 60 MeV | 1.1% | 15.5% | 13.5% | 12.9% | 11.8% | 11.1% | 8.0% | 6.0% |

**Table 6.1:** Relative variance (in percentage) of the values of $P_\nu^{(i)}$ and $F_k^{(i)}$ for an ensemble of 50 sensitive spheres 3 nm in diameter, considering different values of $\nu$ and $k$, as a function of radiation quality, when the full penumbra is simulated.

cluster sizes. However, if the cumulative distributions $F_k^{(i)}$ are considered, the impact of these differences is reduced, as shown in Table 6.1.

As for the case of a single target volume discussed in the previous Chapters, the cumulative distributions $F_k^{(i)}$ represent the probability that at the passage of a single ionizing particle a cluster of $k$ or more ionizations is formed inside the $(i)$-th detector. For each value of $k$, $F_k^{(i)}$ coincides therefore with the probability that the $(i)$-th sphere is "hit" if a threshold value $k$ is defined, and the mean value $\overline{F_k}$ of $F_k^{(i)}$ on all the detecting spheres represents the average probability for each sphere to be "hit" if a threshold value $k$ is considered.

Given the 10% relative variance in the $F_k^{(i)}$ values when the full penumbra is simulated, the question arises whether it is meaningful in this case to define a unique average probability of being hit for all the spheres, regardless of their spatial position, or if the different $F_k^{(i)}$ values produce differences which cannot be neglected. This issue can be solved by comparing the theoretical probability distributions of the number of hit spheres in the two cases, assuming that all spheres respond independently and track-induced correlations in their response can be neglected:

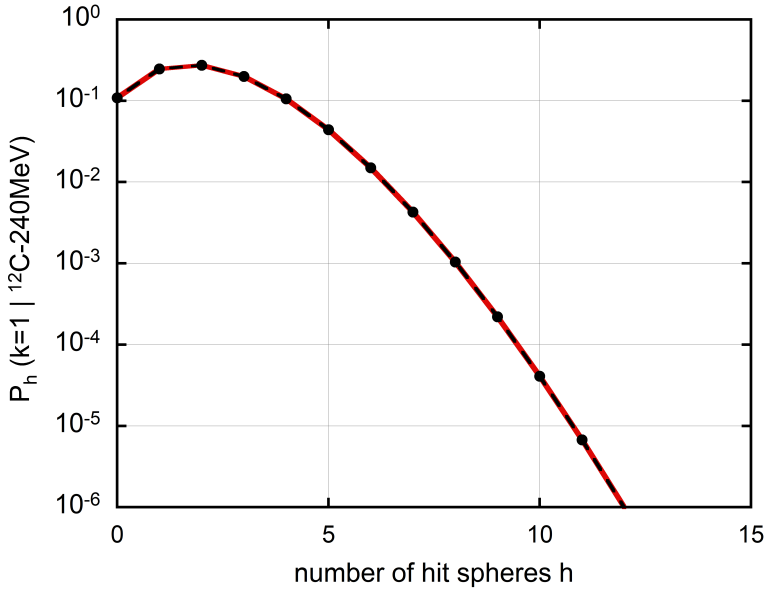


**Figure 6.6:** Comparison between a binomial distribution of parameters $N = N_t$ and $p = \overline{F_k}$ (red continuous line) and the convolution of $N_t$ Bernoulli distributions (black dashed line with black dots) taking into account the differences in the probability $F_k^{(i)}$ of being hit for each sensitive sphere, for an incident beam of 240-MeV carbon ions, a threshold value $k = 1$ and a configuration with 50 spheres 3 nm in diameter.

- If the dependence on spatial position can be neglected as a first approximation, the different $F_k^{(i)}$ can be replaced by a single average value $\overline{F_k} = \frac{1}{N_t}\sum_{i=1}^{N_t} F_k^{(i)}$, a unique probability $p = \overline{F_k}$ of being hit can be defined for all the spheres and the distribution of the number of hit targets should be a binomial distribution $B(N_h;\, N, p)$ with parameters $N = N_t$ and $p = \overline{F_k}$.

- If the dependence on spatial position cannot be neglected, the probability for each target to be hit should be described by a Bernoulli distribution of parameter $p = F_k^{(i)}$ (*i.e.*, a binomial distribution of parameters $N = 1$ and $p = F_k^{(i)}$). The probability of obtaining a number $N_h$ of hit spheres will be given by the convolution $C_{N_t}$ of these $N_t$ Bernoulli distributions $b_i(N_h; F_k^{(i)})$:
  $P(N_h) = b_1(N_h; F_k^{(1)}) * b_2(N_h; F_k^{(2)}) * \ldots * b_{N_t}(N_h; F_k^{(N_t)}) = C_{N_t}(N_h;\, F_k^{(1)}, \ldots, F_k^{(N_t)})$
  The asterisk indicates the convolution operation defined in Section 2.5.1.

These two distributions are compared in Figure 6.6, considering 240-MeV carbon ions as incident radiation quality, a threshold value $k = 1$ and a geometrical configuration with 50 target spheres 3 nm in diameter: the difference between the two curves is almost unnoticeable. It can therefore be stated that as a first approximation each detector responds in the same way to the radiation field, and the frequency distribution of the number of such detectors being "hit" by radiation can be used to characterize the radiation quality also when the full penumbra produced by secondary electron tracks is simulated.

## 6.4 Analysis of the probability distributions

From the number of "hit" spheres in each event, the probability distribution $\tilde{P}_h(k\,|\,Q)$ of the number of hit targets is derived by normalizing on the total number of primary particles, as for the ionization cluster size distributions. It represents the probability that at the passage of each ionizing particle of quality $Q$ (defined by ion type and velocity) a number $h$ of spheres is hit, out of a total of $N_t$. The $\tilde{P}_h(k\,|\,Q)$ distribution is therefore defined for $0 \leq h \leq N_t$.

In the ideal case where track-induced correlations are neglected, it is expected that the distribution of the number of hit spheres is binomial, with parameters $N = N_t$ and $p = \overline{F_k}$, as discussed in Section 6.3. However, particle tracks are highly-structured objects, and sensitive spheres which are aligned along the direction of motion of primary ions have a higher probability to respond together. Track-induced correlations cannot therefore be neglected, and the shape of the $\tilde{P}_h(k\,|\,Q)$ distribution will deviate from a binomial. In particular, it could be assumed that

$$\tilde{P}_h(k\,|\,Q) = \sum_{n=h}^{N_t} C_n \binom{n}{h} (\overline{F_k})^h (1 - \overline{F_k})^{n-h} \tag{6.1}$$

where $C_n$ is a function which takes into account the spatial distribution of the $n$ targets with respect to a random track.

However, since the spheres are uniformly distributed inside the inner cylinder, the mean value $H_1$ of the $\tilde{P}_h(k\,|\,Q)$ distribution should be independent of track-induced correlations. The mean number of hit spheres at the passage of each primary ion is therefore expected to be $N_t\,\overline{F_k}$, according to the intuitive idea that the average number of hit targets is the product of the total number of targets and the probability for each of them to be hit. This will be rigorously shown in Section 6.5.

In the following, the trend of the $\tilde{P}_h(k\,|\,Q)$ distributions is analysed separately for the case where the full penumbra is simulated and for that in which only the secondary electrons produced inside the sensitive targets are tracked up to their boundaries.

### 6.4.1 Simulation of the full penumbra

Figure 6.7 presents the probability distribution of the number of hit spheres resulting from the same simulated data plotted in Figure 6.4. A binomial distribution with parameters $N = N_t$ and $p = \overline{F_k}$ and a Poisson distribution with parameter $\lambda = N_t\overline{F_k}$ are also plotted for comparison. Even if the mean value of the distribution is in good agreement with the theoretical estimation $N_t\overline{F_k}$, it can be seen from the Figure that neither a binomial nor a Poisson model describe satisfactorily the simulated data.

In order to study the dependence of this distribution on target parameters, Figure 6.8 shows the trend of $\tilde{P}_h(k\,|\,Q)$ for configurations with different number of spheres and different diameters, considering again 240-MeV carbon ions and a threshold value $k = 1$. It is clear from the Figure that an increase in the number of targets or in their diameter shifts the distribution towards higher $h$ values, due to the higher amount of volume available for detection, and that the deviations from a binomial distribution due to track-induced

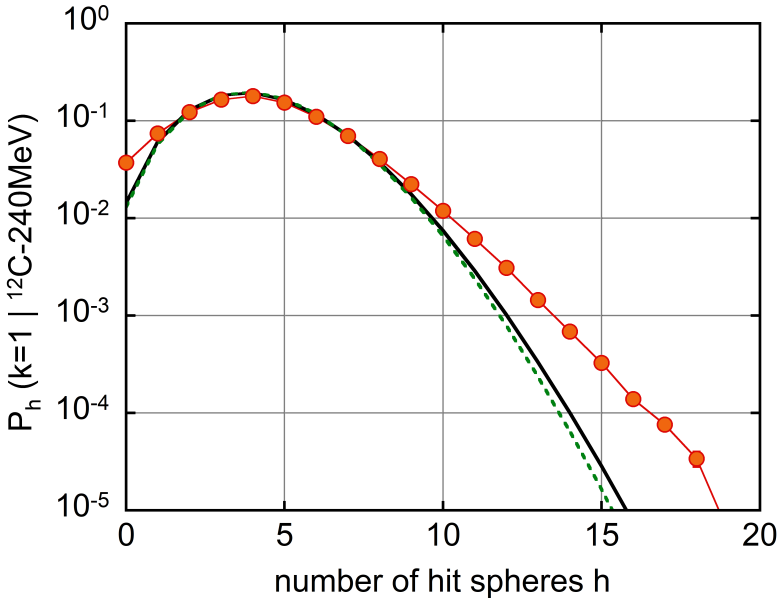


**Figure 6.7:** Probability distribution of the number of hit targets, for an incident beam of 240-MeV carbon ions, considering a configuration with 100 detecting spheres 3 nm in diameter and a threshold value $k = 1$ (orange circles with red line). For comparison, a binomial distribution (green dashed line) and a Poisson one (thick black line) with the same mean value are also plotted.

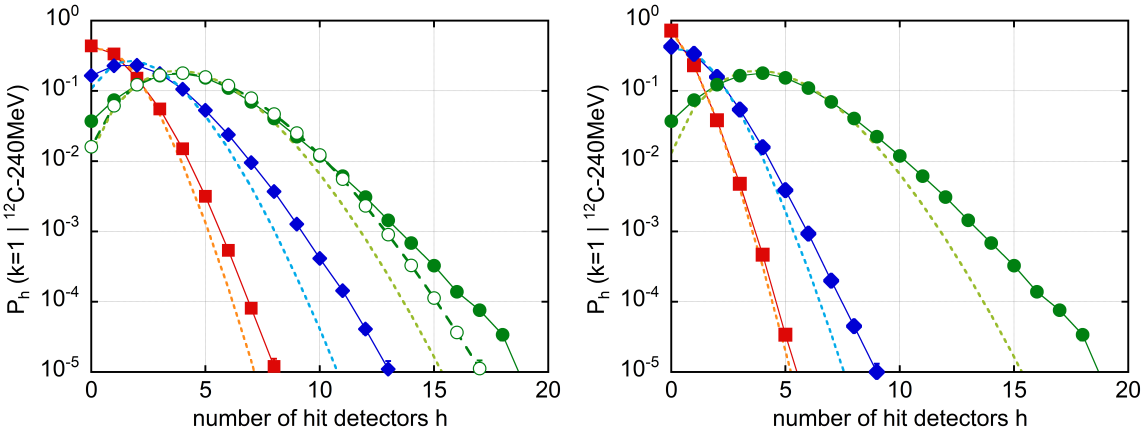


**(a)** Dependence on $N_t$ **(b)** Dependence on $D_t$

**Figure 6.8:** Probability distributions of the number of hit targets, for an incident beam of 240-MeV carbon ions and different geometrical configurations. (a) Dependence on target number, for spheres 3 nm in diameter: $N_t = 20$ (squares with red line), $N_t = 50$ (diamonds with blue line), and $N_t = 100$ (circles with green line). The distribution obtained by 5-fold convolution of that with $N_t = 20$ is also plotted (empty circles with green dashed line). (b) Dependence on target diameter, for a configuration with 100 spheres: $D_t = 1$ nm (squares with red line), $D_t = 1.5$ nm (diamonds with blue line), and $D_t = 3$ nm (circles with green line). For comparison, corresponding binomial distributions with the same mean values are also plotted (dashed lines).

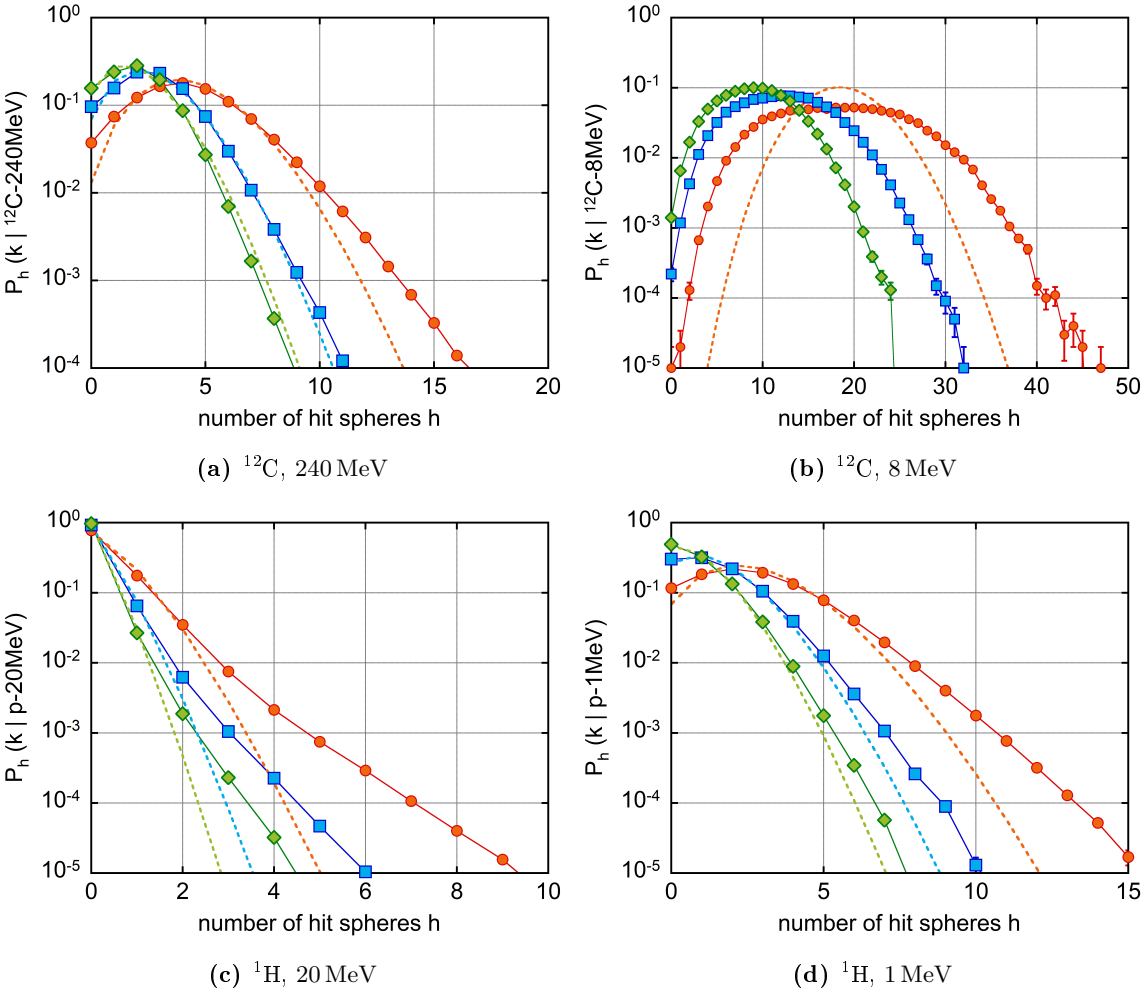


**(a)** $^{12}$C, 240 MeV **(b)** $^{12}$C, 8 MeV

**(c)** $^{1}$H, 20 MeV **(d)** $^{1}$H, 1 MeV

**Figure 6.9:** Dependence of the shape of the probability distribution of the number of hit targets on radiation quality and threshold value, for a setup with 100 spheres 3 nm in diameter. (a) 240-MeV carbon ions, (b) 8-MeV carbon ions, (c) 20-MeV protons, (d) 1-MeV protons. Threshold values of $k = 1$ (orange circles), $k = 2$ (blue squares) and $k = 3$ (green diamonds) are shown. For comparison, corresponding binomial distributions with the same mean values are also plotted in most cases (dashed lines).

correlations are particularly important for a higher number of targets and bigger sphere diameter.

In particular, Figure 6.8(a) shows the distribution of the number of hit targets if the number $N_t$ of spheres is changed: the distribution for a lower target number deviates less from a binomial than that for a configuration with more sensitive spheres. For the case of different target sizes, shown in Figure 6.8(b), the deviations from a binomial are smaller for smaller sphere diameters. However, even if in some cases track-induced correlations are small, they must be studied for each specific configuration: an example is that the distribution for a configuration with 100 detecting spheres cannot be derived from that with 20 by means of a simple 5-fold convolution, as shown in Figure 6.8(b).

Examples of how the $\tilde{P}_h(k\,|\,Q)$ distributions vary with radiation quality and threshold value are shown in Figure 6.9, for a system with 100 detecting spheres 3 nm in diameter. It can be seen that, for the same type of primary ion, the distribution shifts towards higher $h$ values when the energy of the ion is lower. This is mainly due to the increase in the ionization cross section for the primary particle. If primary beams of the same velocity (*i.e.*, the same energy per unit mass) are considered, the distribution shifts towards lower values of $h$ when the atomic number $Z$ is lower, reflecting the decrease of the ionization cross section with decreasing ion charge.

The deviations from a binomial distribution reflect the different track structure of these ions: in particular, a long tail is present in the distributions due to the contribution of low-energy secondary electrons, which alters the distribution shape in particular in the case of low-energy carbon ions, due to their very short mean free path for primary ionization. For any radiation quality, an increase in the threshold value causes a shift of the distribution to the left, due to the more restrictive condition for a sphere to be considered hit. The relative deviations from a binomial generally decrease with increasing threshold, however, this is not always the case, in particular if the mean free path for primary ionizations is larger than the sphere diameter (as it is the case for 20-MeV protons).

### 6.4.2 Simulation of electrons generated inside the spheres only

If secondary electron tracks are simulated only within the target spheres, and their tracks are terminated when they leave the sphere of production, track-induced correlations are expected to play a more relevant role. In particular, the lateral extension of the track is zero in this case, and therefore only the targets located along the direction of incidence of the primary particle have a chance to respond. This implies that a maximum number of hit spheres exists, which corresponds to the ratio between the length of the inner cylinder and the diameter of the detecting sphere.

Figure 6.10 presents the $\tilde{P}_h(k\,|\,Q)$ distribution for 240-MeV carbon ions, considering a geometrical configuration identical to that of Figure 6.7 (100 spheres 3 nm in diameter, threshold value $k = 1$), but for the case where secondary electron tracks are terminated when they leave the sphere of production. The distribution is defined only for a number of hit spheres of 6 or lower and clearly deviates both from a binomial and a Poisson distribution. Its exact shape depends on the arrangement of the spheres within the inner cylinder; however, it shows values lower than the corresponding binomial for $h = 1$, and higher for $h = 2$ and 3. This is a general feature that is independent of the arrangement of the targets in the specific case presented: it reflects the likelihood of having a number $h$ of spheres aligned along a track, for this specific number of targets $N_t$ and sphere diameter $D_t$.

The variation of the $\tilde{P}_h(k\,|\,Q)$ distribution with target parameters is shown in Figure 6.11, for 240-MeV carbon ions and a threshold value $k = 1$. Both reducing the number of spheres without changing their diameter and reducing the sphere diameter without changing their number produce similar effects, *i.e.*, the distribution is shifted to lower values and its similarity with a binomial is increased, due to the fact that less spheres are aligned along a track. The relevant effect of track-induced correlations when the secondary electrons are simulated within the target spheres only is shown very clearly in

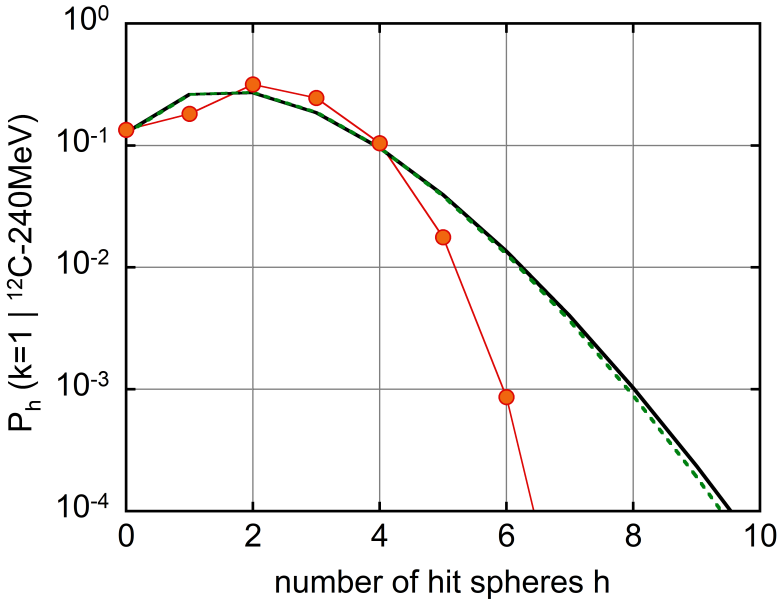


**Figure 6.10:** Probability distribution of the number of hit targets in the case where the secondary electron tracks are simulated only within the sphere of production, for an incident beam of 240-MeV carbon ions, a configuration with 100 detecting spheres 3 nm in diameter and a threshold value $k = 1$ (orange circles with red line). For comparison, a binomial distribution (green dashed line) and a Poisson one (thick black line) with the same mean value are also plotted.

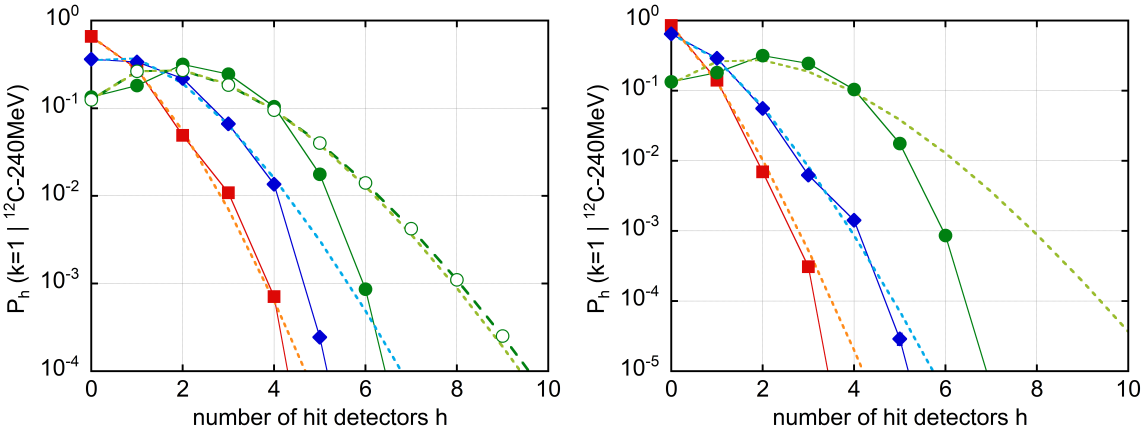


**(a)** Dependence on $N_t$ **(b)** Dependence on $D_t$

**Figure 6.11:** Probability distribution of the number of hit spheres for 240-MeV carbon ions, considering different geometrical configurations. (a) Dependence on target number, for spheres 3 nm in diameter: $N_t = 20$ (squares with red line), $N_t = 50$ (diamonds with blue line), and $N_t = 100$ (circles with green line). The distribution obtained by 5-fold convolution of that with $N_t = 20$ is also plotted (empty circles with green dashed line). (b) Dependence on target diameter, for a configuration with 100 spheres: $D_t = 1$ nm (squares with red line), $D_t = 1.5$ nm (diamonds with blue line), and $D_t = 3$ nm (circles with green line). For comparison, corresponding binomial distributions with the same mean values are also plotted (dashed lines).

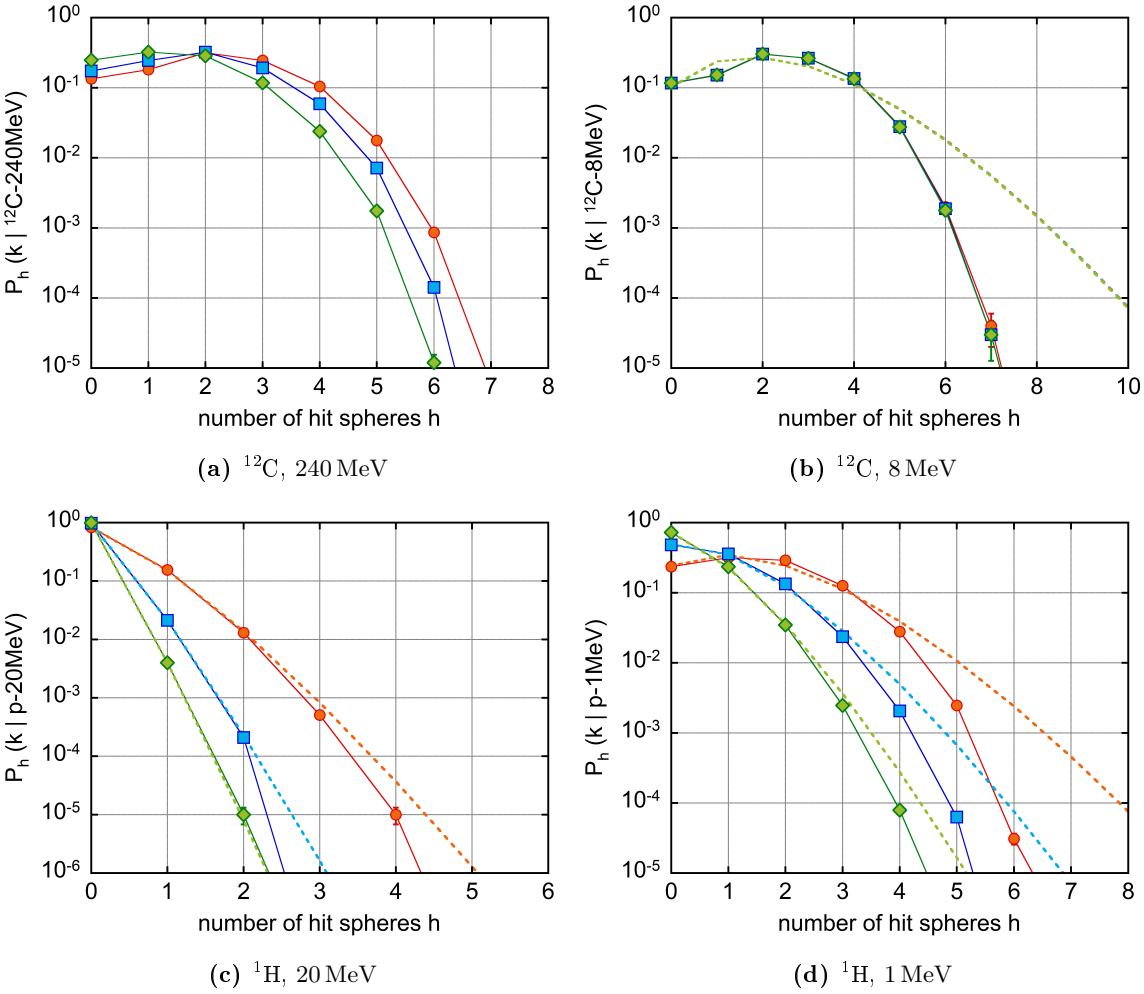


**(a)** $^{12}$C, 240 MeV **(b)** $^{12}$C, 8 MeV

**(c)** $^{1}$H, 20 MeV **(d)** $^{1}$H, 1 MeV

**Figure 6.12:** Dependence of the shape of the probability distribution of the number of hit targets on radiation quality and threshold value, for a setup with 100 spheres 3 nm in diameter. (a) 240-MeV carbon ions, (b) 8-MeV carbon ions, (c) 20-MeV protons, (d) 1-MeV protons. Threshold values of $k = 1$ (orange circles), $k = 2$ (blue squares) and $k = 3$ (green diamonds) are shown. For comparison, corresponding binomial distributions with the same mean values are also plotted in most cases (dashed lines).

Figure 6.11(a): the distribution obtained from the 5-fold convolution of that with $N_t = 20$ is completely different from that with $N_t = 100$, and much more similar to a binomial than the latter. This is due to the fact that track-induced correlations are lost almost completely in the convolution.

The dependence on radiation quality and threshold value is presented in Figure 6.12, for the same type and energy of primary particles discussed in Figure 6.9, considering a configuration with 100 spheres 3 nm in diameter. The maximum value of 6 hit spheres can be seen very clearly in all cases, apart from the sparsely-ionizing 20-MeV protons for which the mean free path is longer than the size of the sensitive spheres. The shape of the distributions can therefore be changed only within this limit, and tends to assume a more

rounded shape when either the threshold value is lowered or the incident radiation is more densely ionizing. When the mean free path for primary ionizations becomes much shorter than target diameter, the distribution converges for all threshold values to the stochastic distribution of the number of targets along a random chord parallel to the central axis of the containing cylinder: this is clearly visible in the case of 8-MeV carbon ions, reported in Figure 6.12(b).

When the secondary electrons are simulated only within the sphere of production, the distribution of the number of hit targets is thus the result of a convolution of the stochastic distribution of the number of targets aligned along a track and the probability of inducing at least $k$ ionizations within a sphere crossed by the trajectory of the primary particle. The latter depends on the ratio between the target diameter and the mean free path for primary ionizations. It is therefore clear why for sparsely-ionizing particles such as 20-MeV protons the similarity to a binomial distribution is more pronounced: the stochastics of the number of ionizations within the single sphere dominates over that of the number of targets aligned along a track. This feature can also be seen for higher threshold values in the case of 1-MeV protons, shown in Figure 6.12(d).

## 6.5 Analysis of the mean values

The mean values $H_1$ have been calculated from the distribution of the number of hit targets $h$ as

$$H_1(k \,|\, Q) = \sum_{h=0}^{N_t} h \, \tilde{P}_h(k \,|\, Q) \tag{6.2}$$

In order to show that $H_1(k \,|\, Q) = N_t \, \overline{F_k}(Q)$, a Boolean function $h_{i,j}$ can be defined for each target $(i)$, which assumes a value of 1 if the target is hit during the event $j$, and a value of 0 if it is not. Using this function, the value of $F_k^{(i)}$ for each target $(i)$ can be defined as the ratio of the number of times in which the target is hit to the total number of primary events $N_p$:

$$F_k^{(i)} = \frac{1}{N_p} \sum_{j=1}^{N_p} h_{i,j} \tag{6.3}$$

Moreover, $H_1$ can also be expressed more directly as the mean number of hit targets over all the primary events:

$$H_1 = \frac{1}{N_p} \sum_{j=1}^{N_p} N_j = \frac{1}{N_p} \sum_{j=1}^{N_p} \sum_{i=1}^{N_t} h_{i,j} \tag{6.4}$$

where $N_j$ is the number of targets which are hit in the event $j$. By changing the summation order it can finally be obtained

$$H_1 = \sum_{i=1}^{N_t} \frac{1}{N_p} \sum_{j=1}^{N_p} h_{i,j} = \sum_{i=1}^{N_t} F_k^{(i)} = N_t \, \overline{F_k} \tag{6.5}$$

The relation $H_1(k \,|\, Q) = N_t \, \overline{F_k}(Q)$ is therefore valid for all incident radiation qualities, threshold values and geometrical configurations of the target spheres.

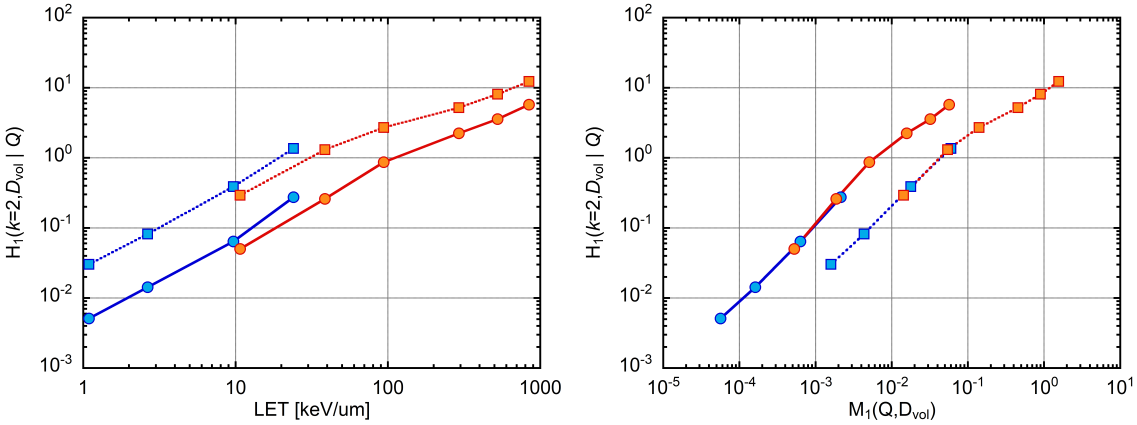


**Figure 6.13:** Dependence of the mean number of hit spheres $H_1$ on radiation quality, for protons (blue) and carbon ions (orange), considering a threshold value $k = 2$, when the full penumbra created by secondary electrons is simulated: (a) dependence on LET, (b) dependence on the average ionization yield $\overline{M_1}$ inside each target sphere. Squares with dotted line correspond to a configuration with $N_t = 100$ and $D_t = 3\,\mathrm{nm}$, circles with continuous line to one with $N_t = 900$ and $D_t = 1\,\mathrm{nm}$.

Given the strong link between $H_1(k\,|\,Q)$ and $\overline{F_k}(Q)$, it is expected that the trend of these two magnitudes is identical when the type and energy of incident radiation is changed. The variation of $H_1$ as a function of the radiation quality is presented in Figure 6.13 for the case where the full penumbra created by secondary electrons is simulated, and in Figure 6.14 for that in which the secondary electron tracks are simulated only inside the spherical targets of production. In both cases, the values of $H_1$ are plotted both as a function of the incident LET and of the mean ionization yield $\overline{M_1}$ averaged over all the target spheres, calculated from the ionization cluster-size distributions for each sphere $(i)$:

$$\overline{M_1} = \frac{1}{N_t} \sum_{i=1}^{N_t} M_1^{(i)} \tag{6.6}$$

In both cases, plotting the values of $H_1$ as a function of $\overline{M_1}$ strongly reduces the differences that are seen between protons and carbon ions when the same data are plotted as a function of LET. This points again to the fact that particles of the same LET have different track structure: in particular, proton tracks are narrower than carbon ion ones for a given LET value, because their velocity is lower. The probability of hitting more spheres within the 10 nm radius of the containing cylinder is therefore higher as well.

For what concerns the case where the full penumbra is simulated, it can be seen in Figure 6.13 that $H_1$ increases with increasing LET with a constant slope up to an LET value of $100\,\mathrm{keV}/\mu\mathrm{m}$, then it keeps increasing but with a less steep slope. This trend is maintained for different target diameters and also for different thresholds, apart from some differences in the slopes before $100\,\mathrm{keV}/\mu\mathrm{m}$: in particular, for $k = 1$ the slope in this LET range is lower. Similar differences are seen for different sphere diameters and threshold

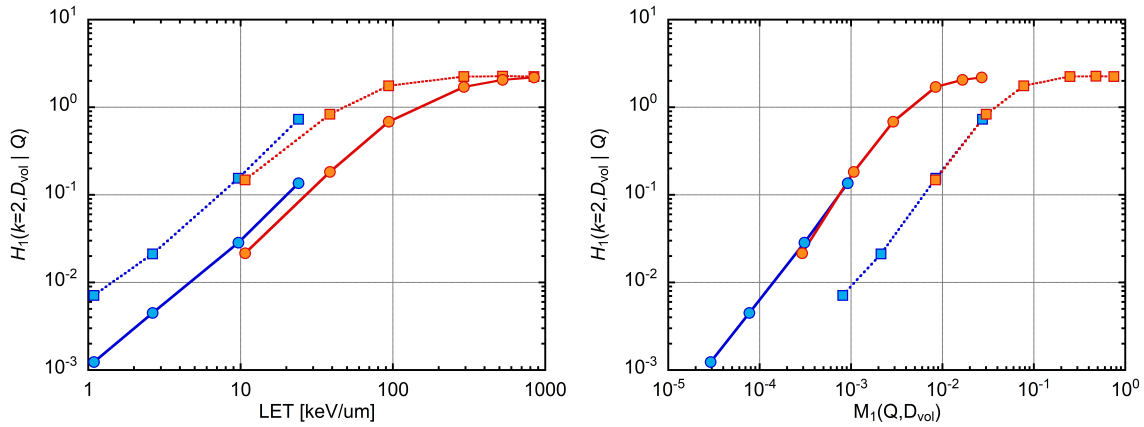


**(a)** **(b)**

**Figure 6.14:** Dependence of the mean number of hit spheres $H_1$ on radiation quality, for protons (blue) and carbon ions (orange), considering a threshold value $k = 2$, when secondary electrons are simulated only within the sphere of production: (a) dependence on LET, (b) dependence on the average ionization yield $\overline{M_1}$ inside each target sphere. Squares with dotted line correspond to a configuration with $N_t = 100$ and $D_t = 3\,\mathrm{nm}$, circles with continuous line to one with $N_t = 900$ and $D_t = 1\,\mathrm{nm}$.

values when the data are plotted as a function of $\overline{M_1}$. In any case, the value of $H_1$ keeps increasing both with increasing LET and with increasing $\overline{M_1}$, regardless of the specific target size and threshold value under consideration.

The trend is completely different when the secondary electron tracks are terminated as soon as they leave the sphere of production: in this case, a clear saturation is visible for high LET or $\overline{M_1}$, regardless of target diameter and threshold value. This can be explained by the fact that when the mean free path for primary ionizations becomes much smaller than the target diameter, all the spheres crossed by a primary ion will be hit. The mean number of hit targets converges therefore to the mean number of spheres crossed by a random chord parallel to the central axis of the inner cylinder, since primary particles travel approximately on straight lines parallel to this axis and are arranged uniformly on the cross section of the incident beam.

The saturation value depends of course on the number $N_t$ of sensitive spheres, and since $H_1(k \mid Q) = N_t\,\overline{F_k}(Q)$ it reflects the saturation of the $\overline{F_k}$ values. For the case where the secondary electron tracks are simulated only within the target sphere of production, $\overline{F_k}$ is the product of two factors: the probability that the primary particles enters the target sphere and the probability that if it indeed enters the target sphere, it produces more than $k$ ionizations within it, according to the law of conditional probability. The first factor is given by the ratio of the cross section of the target sphere to that of the primary beam, *i.e.* $D_t^2/D_b^2$, since the beam is uniform. The second depends on radiation quality and is conceptually identical to the cumulative probability of inducing more than $k$ ionizations in a single target volume defined in Section 2.1, provided that the primary particle indeed crosses the volume of interest. Due to the latter constraint, this probability will be indicated in the following with $\overline{F_k}^{(c)}$.

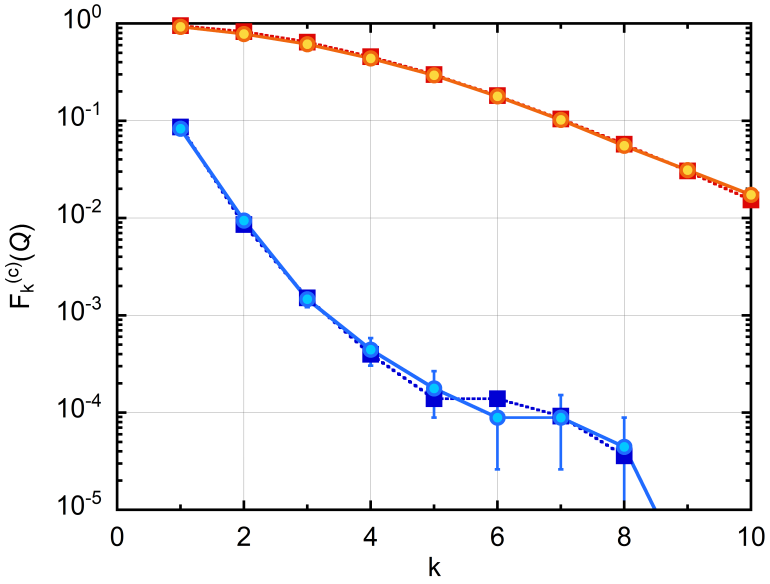


**Figure 6.15:** Comparison between simulated and experimental values of $\overline{F_k}^{(c)}$ as a function of the threshold value $k$, for 20-MeV protons (blue) and 240-MeV carbon ions (orange) when the secondary electrons are transported only up to the boundary of the sphere of production. Squares with dotted line correspond to experimental data measured with the Startrack counter, circles with continuous line to GEANT4 simulations. Statistical uncertainties are plotted for the Monte Carlo data only.

For the case where the secondary electrons are transported only up to the boundary of the sphere of production, the value of $H_1$ can thus be expressed as

$$H_1(k\,|\,Q) = N_t \frac{D_t^2}{D_b^2} \overline{F_k}^{(c)}(Q) \tag{6.7}$$

and $H_1$ saturates to a value of $N_t \cdot D_t^2/D_b^2$ when $\overline{F_k}^{(c)} \to 1$. The LET or $\overline{M_1}$ value at which the saturation is reached and the slope before saturation depend on the threshold value, as it can be expected from the proportionality between $H_1$ and $\overline{F_k}^{(c)}$.

Given this finding, it can be interesting to compare the results of these simulations to experimental measurements carried out with the Startrack counter, and to inactivation cross sections for different survival levels. The former comparison is shown in Figure 6.15, for 20-MeV protons and 240-MeV carbon ions, as a function of the threshold value $k$. For the simulated data, a configuration with 100 detecting spheres 3 nm in diameter is considered, and $H_1$ values have been divided by the factor $N_t \cdot D_t^2/D_b^2$ in order to obtain $\overline{F_k}^{(c)}$. Experimental data are derived from ionization cluster-size distributions measured with the Startrack counter at a propane pressure of 300 Pa, corresponding to an effective target size of 5 nm at unit density. Since measurements in a site size of 3 nm have not been taken yet for these radiation qualities, an impact parameter of 1.5 mm (corresponding to 2 nm) has been considered in order to obtain an effective travelling length of 3 nm inside the target volume. The different chord length distribution and the asymmetry in the secondary

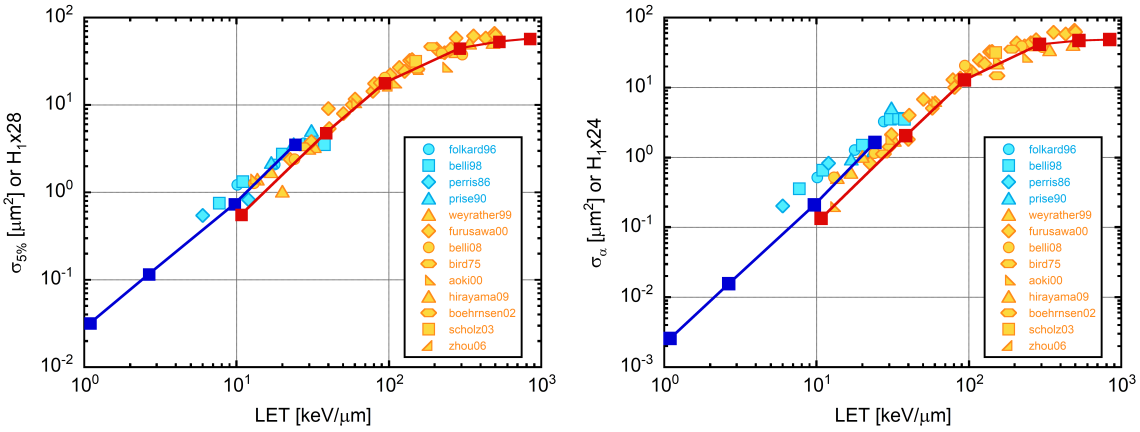


(a) (b)

**Figure 6.16:** Comparison between inactivation cross sections for V79 cells at two survival levels and GEANT4 simulations (squares) for different target sizes and threshold values. (a) $\sigma_{5\%}$ compared with scaled $H_1$ values for a configuration with 900 sensitive spheres 1 nm in diameter, considering a threshold value $k = 2$. (b) $\sigma_\alpha$ compared with scaled $H_1$ values for a configuration with 400 sensitive spheres 1.5 nm in diameter, considering a threshold value $k = 3$. The saturation value of $H_1$ is 2.25 in both cases. The inactivation cross sections are shown in light blue for irradiation with protons, in orange with carbon ions.

electron degradation are expected to play only a minor role in this case. Indeed, the two curves are very similar, and all experimental points lie within the statistical uncertainty of the simulation.

Figure 6.16 compares the results of GEANT4 simulations to inactivation cross sections at 5% survival level and at initial survival. Given the results presented in Section 5.2, it can be expected that for the case of $\sigma_{5\%}$, the correlation is optimized considering a threshold value $k = 2$ and sensitive targets 1 nm in size, while for $\sigma_\alpha$ values of $k = 3$ and $D_t = 1.5$ nm must be considered. Moreover, since $H_1$ saturates at a value of $N_t \cdot D_t^2/D_b^2$, it should be scaled by a factor $C_\sigma \cdot D_b^2/(N_t \cdot D_t^2)$, where $C_\sigma$ is the same scaling factor applied in Section 5.2 to experimental data. This is indeed the case: after $H_1$ values are scaled for this factor in order to match their saturation level to that of inactivation cross sections, the agreement between the two sets of data is very good.

The detector concept implemented in this study seems therefore a promising candidate for the development of a portable nanodosimeter, since the mean number $H_1$ of hit targets retains enough information for a consistent characterization of the radiation field. This is because $H_1$ is equal to $N_t \overline{F_k}$, where $N_t$ is the number of detecting spheres and $\overline{F_k}$ is the probability for each of them to be "hit". Therefore, if the total number of spheres is known and the threshold value $k$ with which they respond is tuneable, an estimation of the single-event quantity $\overline{F_k}$ can be made from the value of $H_1$, providing access to a quantity which would probably be unmeasurable in a real nanometric volume at unit density. In addition, since $H_1$ is defined as a mean value, it can be obtained by normalising the total number of hit targets on the total number of primary ions, thus removing the need for single particle detection, provided that the incident particle fluence is kept low enough so

that the probability of two-particle hit inside a single sphere is negligible.

However, the trend of $H_1$ as a function of incident LET matches that of inactivation cross sections only if the geometrical boundary of the sensitive targets is impenetrable to secondary electrons. The latter fact makes the feasibility of such a detector far from obvious, even if other constraints on target number, diameter and threshold tuning are met.

# Chapter 7

# Conclusions

The work presented in this thesis developed towards three main aims:

1. To measure the ionization yield in a sensitive volume about 1 nm in size: the operative range of the Startrack counter had therefore to be extended to pressure values lower than the standard one of 300 Pa, assessing at the same time the effect of a drastic decrease in the detection efficiency.

2. To identify nanodosimetric magnitudes which can be used as monitors for biological effects at cellular level, by analysing the correlation between measurable descriptors of particle track structure and given end-points for cell survival.

3. To investigate if a simplified multi-target system retains enough information for a consistent characterization of the track structure, even if it does not measure the full stochastic distribution of the ionization yield, as a first proof-of principle study for a compact, portable nanodosimeter to be used for radiotherapy or radiation protection applications.

For what concerns the first aim, the main conclusions of this work are resumed in the following:

- The Startrack counter gives a consistent characterization of the track structure at a gas pressure of 200 Pa, both for sparsely-ionizing and densely-ionizing radiation. A comparison with the Monte Carlo code *MC-Startrack* suggests that the assumption of a uniform scaling of the efficiency map when the gas pressure is reduced is reliable. In these conditions, the average detection efficiency is about 7%. From a comparison with Monte Carlo simulations carried out at 100% detection efficiency, an effective target size of 1.5 nm can be defined for the Startrack counter at this pressure.

- At a gas pressure of 170 Pa, the validity of the approximation of uniform scaling of the efficiency map is confirmed, and the average detection efficiency is about 4%. However, first indications arise from the comparison with simulations at 100% efficiency that the definition of an effective target size is problematic at this pressure, since the site size that optimizes the correlation between experimental and calculated data varies slightly with the radiation quality. Further measurements and simulations are therefore needed in order to investigate this point.

- Preliminary tests with a single radiation quality ($^7$Li at 16.4 MeV) indicate that the response of the Startrack counter is consistent up to a minimum propane pressure of 150 Pa. The measurements should however be extended to other radiation qualities.

Concerning the second aim, an outstanding correlation is found between the inverse cumulative distribution functions $F_k$ obtained from experimental measurements and inactivation cross sections for different end-points of cell survival. In particular, for radio-resistant cell lines, the inactivation cross section $\sigma_{5\%}$ at 5% survival level is proportional to the cumulative probability $F_2$ of measuring two ionizations in a target volume 1 nm in size, and the cross section $\sigma_\alpha$ for initial survival is proportional to the cumulative probability $F_3$ of measuring at least three ionizations in a target volume 1.5 nm in size. For radio-sensitive cell lines, such as the mutant XRS5, the inactivation cross section is the same for all survival level, and it was found to be proportional to $F_1$, *i.e.*, the probability of measuring at least one ionization in the target volume, if the latter is 0.3 nm in size.

This direct proportionality between inactivation cross sections and cumulative probabilities was found to be valid regardless of the specific cell line which is considered: both rodent (V79, CHO) and human (HSG, T1) radio-resistant cell lines show the same behaviour, only with a different proportionality factor, which is specific for each cell line. Given the direct proportionality between $F_2$ and $\sigma_{5\%}$ and $F_3$ and $\sigma_\alpha$, the $\alpha$ and $\beta$ parameters of the linear-quadratic dose-response model of cell survival can be calculated for an unknown radiation field from a nanodosimetric measurement of $F_2$ and $F_3$, after the proportionality factor $C_{5\%}$ and $C_\alpha$ for the specific cell line under analysis have been derived from a calibration on radiobiological data, using a reference radiation quality. The full cell survival curve can thus be reconstructed from nanodosimetric measurements, also in unknown radiation fields.

The validity of this procedure has been studied on a set of published cell survival curves for V79 cells irradiated by carbon ions with different incident LET, obtaining in most cases quite a good agreement between the literature curve and the nanodosimetry-derived one. Some discrepancies are however found, in particular at higher LET. This study must therefore be extended in order to assess possible uncertainties and limits of applicability.

However, direct nanodosimetric measurements cannot be obtained at present for all radiation qualities considered in the literature cell survival curves examined in the present study, due to the beam energy limits of the Tandem-ALPI accelerator complex of INFN-LNL. In particular, for carbon ions the maximum available energy is 240 MeV, corresponding to an LET of about 100 keV/$\mu$m and a $M_1$ in a volume of 1 nm of about 1.1; the available carbon ion qualities are therefore those identified by the red area shown in Figure 7.1. Vice versa, in the case of charge state $Z = 1$ the minimum energy at which a stable operation of the accelerator can be achieved is about 8 MeV for protons and 4 MeV for deuterons. The latter corresponds to an LET of about 10 keV/$\mu$m and to a $M_1$ of 0.1 in a volume of 1 nm; the available range is therefore that shown in blue in Figure 7.1.

Given the limited portability of the Startrack counter, it would be necessary to build a simplified version of it, which could be moved to other accelerator facilities in order to investigate both higher-energy carbon ion beams and lower-energy proton ones. In this way, nanodosimetric measurements could be carried out with the same radiation qualities used in the radiobiological experiments, and a one-to-one correspondence between the two

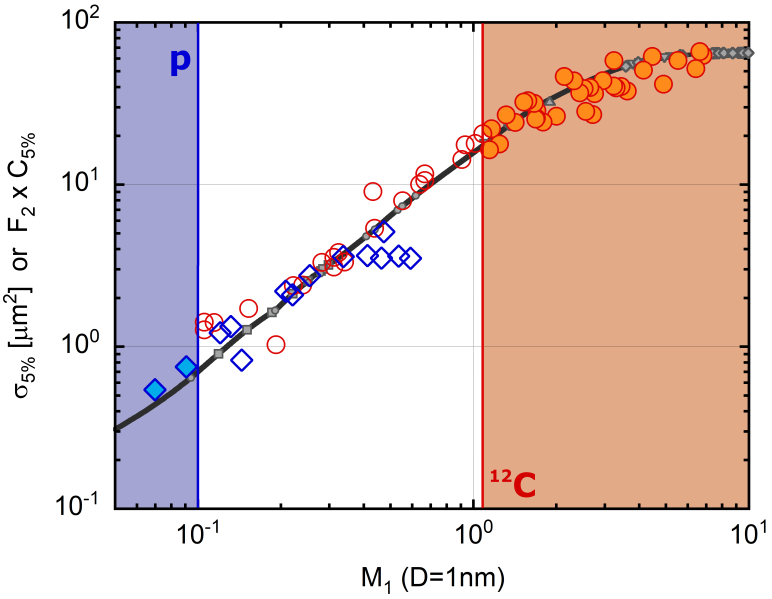


**Figure 7.1:** Range of radiation qualities for which the $F_2$ value corresponding to a given inactivation cross section can be measured at present with the Startrack counter installed at the Tandem-ALPI accelerator facility at INFN-LNL: full symbols correspond to radiobiological data for which the corresponding $F_2$ value can be measured at present, for protons (blue) and carbon ions (orange); empty ones to data for which the corresponding nanodosimetric measurement cannot be carried out.

sets of data could be made.

For what concerns the third aim, a simulation tool has been developed in order to study particle track structure in a multi-target environment. It is based on the GEANT4-DNA physical models of the GEANT4 toolkit and models a set of nanometre-sized spherical detecting volumes dispersed in a cylindrical outer layer. Each sensitive volume is considered "hit" if $k$ or more ionizations take place inside it, where $k$ is a tuneable threshold value which represents the sensitivity of individual targets to radiation damage. Two different tracking options have been considered: in the first one, the full penumbra is simulated; in the second one, the secondary electrons are simulated only up to the geometrical boundary of the volume of their production.

It has been found that for both tracking options the mean value $H_1$ of the distribution is given by $N_t \cdot \overline{F_k}$, where $N_t$ is the number of target spheres and $\overline{F_k}$ is the average probability for each of them to be "hit", which corresponds to the $k$-th value of the cumulative distribution function of the ionization cluster size distribution (*i.e.*, at least $k$ ionizations take place within the sensitive volume). Therefore, if the total number of spheres is known, an estimation of the single-event quantity $\overline{F_k}$ can be made from the value of $H_1$. Moreover, when the secondary electrons are simulated only up to the boundary of the volume of their production, the trend of $H_1$ reproduces that of inactivation cross sections both at 5% survival level and at initial survival, if the target diameter and threshold value are tuned to specific values ($k = 2$ and diameter of 1 nm in the first case, and $k = 3$ and diameter of 1.5 nm in the second).

The setup implemented in this study seems therefore a good detector concept for a portable nanodosimeter, since the mean number $H_1$ of hit targets retains enough information for a consistent characterization of particle track structure. This could be of interest for the application of nanodosimetry to radiation therapy and radiation protection. However, the trend of $H_1$ as a function of LET matches that of inactivation cross sections only if the target spheres are screened from the secondary electron contribution generated by primary particles not directly crossing their volume. The requirement of an ideally impenetrable boundary of the sensitive structures increases the difficulty in the practical realization of such a detector concept. Experimental and theoretical options to overcome this problem will be a matter for future study.

# Bibliography


[Alkhazov, 1970] Alkhazov, G.D., *Statistics of electron avalanches and ultimate resolution of proportional counters.* Nucl. Instrum. Meth. 89, 155–165 (1970).

[Aoyama, 1985] Aoyama, T., *Generalized gas gain formula for proportional counters.* Nucl. Instrum. Meth. Phys. Res. A 234, 125–131 (1985).

[Bantsar, 2006] Bantsar, A., Grosswendt, B. and Pszona, S., *Formation of ion clusters by low-energy electrons in nanometric targets: experiment and Monte Carlo simulation.* Radiat. Prot. Dosim. 122, 82–85 (2006).

[Bashkirov, 2006] Bashkirov, V., Schulte, R., Breskin, A., Chechik, R., Shchemelinin, S., Garty, G., Wroe, A., Sadrozinski, H. and Grosswendt, B., *Ion-counting nanodosimeter with particle tracking capabilities.* Radiat. Prot. Dosim. 122, 415–419 (2006).

[Bashkirov, 2009] Bashkirov, V., Schulte, R., Wroe, A., Sadrozinski, H., Gargioni, E. and Grosswendt, B., *Experimental validation of track structure models.* IEEE Trans. Nucl. Sci. 56, 2859–2863 (2009).

[Belli, 1998] Belli, M., Cera, F., Cherubini, R., Dalla Vecchia, M., Haqjue, A.M.I., Ianzini, F., Moschini, G., Sapora, O., Simone, G., Tabocchini, M.A. and Tiveron, P., *RBE-LET relationships for cell inactivation and mutation induced by low energy protons in V79 cells: Further results at the LNL facility.* Int. J. Radiat. Biol. 74, 501–509 (1998).

[Belli, 2008] Belli, M., Bettega, D., Calzolari, P., Cherubini, R., Cuttone, G., Durante, M., Esposito, G., Furusawa, Y., Gerardi, S., Gialanella, G., Grossi, G., Manti, L., Marchesini, R., Pugliese, M., Scampoli, P., Simone, G., Sorrentino, E., Tabocchini, M.A. and Tallone, L., *Effectiveness of monoenergetic and spread-out Bragg peak carbon-ions for inactivation of various normal and tumour human cell lines.* J. Radiat. Res. 49, 597–607 (2008).

[Belloni, 2002] Belloni, F., Bettega, D., Calzolari, P., Cherubini, R., Massariello, P. and Tallone, L., *Inactivation cross sections for mammalian cells exposed to charged particles: a phenomenological approach.* Radiat. Prot. Dosim. 99, 199–202 (2002).

[Berger, 1963] Berger, M.J., *Monte-Carlo calculations of the penetration and diffusion of fast charged particles.* In: Alder, B., Fenebach, S., Rotenberg, M. (Eds.), Methods in Computational Physics, vol. 1. Academic Press, New York, p. 135 (1963).

[Berger, 1970] Berger, M.J., *Spectrum of energy deposited by electrons in spherical regions.* In: Ebert, H.G. (Ed.), Proceedings of the Second Symposium on Microdosimetry

(Report EUR 4452). Commission of the European Communities, Brussels, p. 541–559 (1970).

[Bernal, 2015] Bernal, M.A., Bordage, M.C., Brown, J.M.C., Davídková, M., Delage, E., El Bitar, Z., Enger, S.A., Francis, Z., Guatelli, S., Ivanchenko, V.N., Karamitros, M., Kyriakou, I., Maigne, L., Meylan, S., Murakami, K., Okada, S., Payno, H., Perrot, Y., Petrovic, I., Pham, Q.T., Ristic-Fira, A., Sasaki, T., Štěpán, V., Tran, H.N., Villagrasa, C. and Incerti., S., *Track structure modelling in liquid water: A review of the* Geant4-DNA *very low energy extension of the* Geant4 *Monte Carlo simulation toolkit.* Phys. Med. 31, 861–874 (2015).

[Brenner, 1983] Brenner, D.J. and Zaider, M., *A computationally convenient parametrisation of experimental angular distributions of low energy electrons elastically scattered off water vapour.* Phys. Med. Biol. 29, 443–447 (1983).

[Breskin, 1983] Breskin, A., Chechik, R., Levin, I. and Zwang, N., *Heavy particle timing and imaging with low-pressure MWPCs.* Nucl. Instrum. Meth. Phys. Res. 217, 107–111 (1983).

[Breskin, 1984] Breskin, A., Charpak, G. and Majewski, S., *On the low-pressure operation of multistep avalanche chambers.* Nucl. Instrum. Meth. Phys. Res. A 220, 349–355 (1984).

[Byrne, 1969] Byrne, J., *Statistics of electron avalanches in the proportional counter.* Nucl. Instrum. Meth. 74, 291–296 (1969).

[Champion, 2009] Champion, C., Incerti, S., Aouchiche, H. and Oubaziz, D., *A free-parameter theoretical model for describing the electron elastic scattering in water in the* Geant4 *toolkit.* Rad. Phys. Chem. 78, 745–750 (2009).

[Chouki, 1994] Chouki, A., *Détermination des sections efficaces de collision électron-molécule dans l'éthane, le propane et l'isobutane.* Doctoral thesis at Paul Sabatier University, Toulouse, France (1994).

[Conte, 2010] Conte, V., De Nardo, L., Colautti, P., Ferretti, A., Grosswendt, B., Lombardi, M., Poggi, M., Canella, S., Moro, D. and Tornielli, G., *First track-structure measurements of 20 MeV protons with the STARTRACK apparatus.* Radiat. Meas. 45, 1213–1216 (2010).

[Conte, 2012] Conte, V., Colautti, P., Grosswendt, B., Moro, D., De Nardo, L., *Track structure of light ions: experiments and simulations.* New J. Phys. 14, 093010 (2012).

[Conte, 2014] Conte, V., Colautti, P., Moro, D. and Grosswendt, B., *Track structure of carbon ions: measurements and simulations.* Radiat. Prot. Dosim. 161, 445–448 (2014).

[Conte, 2015] Conte, V., Moro, D., Colautti, P., Grosswendt, B., *Nanodosimetric track structure in homogeneous extended beams.* Radiat. Prot. Dosim. 166, 219–222 (2015).

[Dalla Pellegrina, 1998] Dalla Pellegrina, A., *Caratterizzazione di un rivelatore di singoli elettroni per misure di nanodosimetria di traccia.* Tesi di Laurea at the University of Padua, Padua, Italy (1998).

[De Nardo, 1995] De Nardo, L., *Un rivelatore per nanodosimetria di traccia.* Tesi di Laurea at the University of Padua, Padua, Italy (1995).

[De Nardo, 1998] De Nardo, L., *High resolution track-nanodosimetry analysis of charged particles.* Doctoral thesis at the University of Padua, Padua, Italy (1998).

[De Nardo, 2002a] De Nardo, L., Colautti, P., Conte, V., Baek, W.Y., Grosswendt, B., and Tornielli, G., *Ionization-cluster distributions of $\alpha$-particles in nanometric volumes of propane: measurement and calculation.* Radiat. Environ. Biophys. 41, 235–256 (2002).

[De Nardo, 2002b] De Nardo, L., Alkaa, A., Khamphan, C., Conte, V., Colautti, P., Ségur, P. and Tornielli, G., *A detector for track-nanodosimetry.* Nucl. Instrum. Methods. Phys. Res. A 484, 312–326 (2002).

[Dingfelder, 2000] Dingfelder, M., Inokuti, M., Paretzke, H.G., *Inelastic-collision cross sections of liquid water for interactions of energetic protons.* Radiat. Phys. Chem. 59, 255–275 (2000).

[Dingfelder, 2005] Dingfelder, M., Toburen, L.H. and Paretzke, H.G., *An effective charge scaling model for ionization of partially dressed helium ions with liquid water.* In: Proceedings of the Monte Carlo 2005 Topical Meeting, Chattanooga, Tennessee (2005).

[Durante, 2016] Durante, M. and Paganetti, H., *Nuclear physics in particle therapy: a review.* Rep. Prog. Phys. 79, 096702 (2016).

[Emfietzoglou, 2003] Emfietzoglou, D., *Inelastic cross-sections for electron transport in liquid water: a comparison of dielectric models.* Radiat. Phys. Chem. 66, 373–385 (2003).

[Ferretti, 2006] Ferretti, A., *Startrack: analisi dei primi dati sperimentali e studio di un nuovo rivelatore di singolo elettrone.* Tesi di Laurea at the University of Padua, Padua, Italy (2006).

[Folkard, 1996] Folkard, M., Prise, K.M. and Voijnovic, B., *Inactivation of V79 cells by low-energy protons, deuterons and helium-3 ions.* Int. J. Radiat. Biol. 69, 729–738 (1996).

[Francis, 2012] Francis, Z., Incerti, S., Ivanchenko, V., Champion, C., Karamitros, M., Bernal, M.A. and El Bitar, Z., *Monte Carlo simulation of energy-deposit clustering for ions of the same LET in liquid water.* Phys. Med. Biol. 57, 209–224 (2012).

[Friedland, 2011] Friedland, W., Dingfelder, M., Kundrát, P. and Jacob, P., *Track structures, DNA targets and radiation effects in the biophysical Monte Carlo simulation code* PARTRAC. Mutat. Res. 711, 28–40 (2011).

[Friedrich, 2013] Friedrich, T., Scholz, U., Elsässer, T., Durante, M. and Scholz, M., *Systematic analysis of RBE and related quantities using a database of cell survival experiments with ion beam irradiation.* J. Radiat. Res. 54, 494–514 (2013).

[Garty, 2002] Garty, G., Shchemelinin, S., Breskin, A., Chechik, R., Assaf, G., Orion, I., Bashkirov, V., Schulte, R.W. and Grosswendt, B., *The performance of a novel ion-counting nanodosimeter.* Nucl. Instrum. Meth. Phys. Res. A 492, 212–235 (2002).

[Garty, 2010] Garty, G., Schulte, R., Shchemelinin, S., Leloup, C., Assaf, G., Breskin, A., Chechik, R., Bashkirov, V., Milligan, J. and Grosswendt, B., *A nanodosimetric model of radiation-induced clustered DNA damage yields.* Phys. Med. Biol. 55, 761–781 (2010).

[GEANT4, Physics Reference Manual] GEANT4 Collaboration, *Physics Reference Manual.* Available online: http://geant4.web.cern.ch/geant4/UserDocumentation/UsersGuides/PhysicsReferenceManual/fo/PhysicsReferenceManual.pdf

[Goodhead, 1994] Goodhead, D.T., *Initial events in the cellular effects of ionizing radiations: clustered damage in DNA.* Int. J. Radiat. Biol. 65, 7–17 (1994).

[Green, 1972] Green, A.E.S. and Sawada, T., *Ionization cross sections and secondary electron distributions.* J. Atmosph. Terr. Phys. 34, 1719–1728 (1972).

[Grosswendt, 2000] Grosswendt, B. and Baek, W.Y., *Basic physical data in organic gases.* In: Colautti, P. (Ed.), Radiation quality assessment based on physical radiation interaction at nanometer level (LNL Report 161). INFN-Laboratori Nazionali di Legnaro, Padova, Italy, p. 5–26 (2000).

[Grosswendt, 2002a] Grosswendt, B., *Formation of ionization clusters in nanometric structures of propane-based tissue-equivalent gas or liquid water by electrons and $\alpha$-particles.* Radiat. Environ. Biophys. 41, 103–112 (2002).

[Grosswendt, 2002b] Grosswendt, B. and Pszona, S., *The track structure of alpha-particles from the point of view of ionization-cluster formation in 'nanometric' volumes of nitrogen.* Radiat. Environ. Biophys. 41, 91–102 (2002).

[Grosswendt, 2004a] Grosswendt, B., De Nardo, L., Colautti, P., Pszona, S., Conte, V. and Tornielli, G., *Experimental equivalent cluster-size distributions in nanometric volumes of liquid water.* Radiat. Prot. Dosim. 110, 851–857 (2004).

[Grosswendt, 2004b] Grosswendt, B., *Recent advances of nanodosimetry.* Radiat. Prot. Dosim. 110, 789–799 (2004).

[Grosswendt, 2014] Grosswendt, B., Conte, V. and Colautti, P., *An upgraded track structure model: experimental validation.* Radiat. Prot. Dosim. 161, 464–468 (2014).

[Grosswendt, priv. comm.] Grosswendt, B., *The arrival-time distribution of electrons at the electron detector.* Private communication.

[Hilgers, 2015] Hilgers, G., Bug, M.U., Gargioni, E. and Rabus, H., *Secondary ionisations in a wall-less ion-counting nanodosimeter: quantitative analysis and the effect on the comparison of measured and simulated track structure parameters in nanometric volumes.* Eur. Phys. J. D 69, 239 (2015).

[Hilgers, 2017] Hilgers, G., Bug, M.U. and Rabus, H., *Measurement of track structure parameters of low and medium energy helium and carbon ions in nanometric volumes.* Phys. Med. Biol. 62, 7569–7597 (2017).

[Hunter, 2009] Hunter, N. and Muirhead, C.R., *Review of relative biological effectiveness dependence on linear energy transfer for low LET radiations.* J. Radiol. Prot. 29, 5–21 (2009).

[Hwang, 1996] Hwang, W., Kim, Y.K. and Rudd, M.E., *New model for electron-impact ionization cross sections of molecules.* J. Chem. Phys. 104, 2956–2966 (1996).

[ICRU, 1970] ICRU, *Linear Energy Transfer.* International Commission on Radiation Units and Measurements, Report No. 16 (1970).

[ICRU, 1993] ICRU, *Stopping powers and ranges for protons and alpha particles.* International Commission on Radiation Units and Measurements, Report No. 49 (1993).

[ICRU, 1996] ICRU, *Secondary electron spectra from charged particle interactions.* International Commission on Radiation Units and Measurements, Report No. 55 (1996).

[ICRU, 2011] ICRU, *Fundamental quantities and units for ionizing radiation.* International Commission on Radiation Units and Measurements, Report No. 85 (revised) (2011).

[Incerti, 2010a] Incerti, S., Baldacchino, G., Bernal, M.A., Capra, R., Champion, C., Francis, Z., Guèye, P., Mantero, A., Mascialino, B., Moretto, P., Nieminen, P., Villagrasa, C. and Zacharatou, C., *The* GEANT4-DNA *project.* Int. J. Model. Simul. Sci. Comput. 1, 157–178 (2010).

[Incerti, 2010b] Incerti, S., Ivanchenko, A., Karamitros, M., Mantero, A., Moretto, P., Tran, H.N., Mascialino, B., Champion, C., Ivanchenko, V.N., Bernal, M.A., Francis, Z., Villagrasa, C., Baldacchino, G., Guèye, P., Capra, R., Nieminen, P. and Zacharatou, C., *Comparison of* GEANT4 *very low energy cross section models with experimental data in water.* Med. Phys. 37, 4692–4708 (2010).

[Incerti, 2016] Incerti, S., Douglass, M., Penfold, S., Guatelli, S. and Bezak, E., *Review of* GEANT4-DNA *applications for micro and nanoscale simulations.* Phys. Med. 32, 1187–1200 (2016).

[Jackman, 1977] Jackman, C.H., Garvey, R.H. and Green, A.E.S., *Electron impact on atmospheric gases. I. Updated cross sections.* J. Geophys. Res. 82, 5081–5090 (1977).

[Kiefer, 2008] Kiefer, J., *The physical basis for the biological action of heavy ions.* New J. Phys. 10, 075004 (2008).

[Kim, 1994] Kim, Y.K. and Rudd, M.E., *Binary-encounter-dipole model for electron-impact ionization.* Phys. Rev. A 50, 3954–3967 (1994).

[Kyriakou, 2015] Kyriakou, I., Incerti, S. and Francis, Z., *Improvements in* GEANT4 *energy-loss model and the effect on low-energy electron transport in liquid water.* Med. Phys. 42, 3870–3876 (2015).

[Melton, 1972] Melton, E.C., *Cross sections and interpretation of dissociative attachment reactions producing* $OH^-$, $O^-$ *and* $H^-$ *in* $H_2O$. J. Chem. Phys. 57, 4218–4225 (1972).

[Michaud, 2003] Michaud, M., Wen, A. and Sanche, L., *Elastic and inelastic cross-sections for low-energy* $(1 - 100\ eV)$ *electron scattering in amorphous ice.* Radiat. Res. 159, 3–22 (2003).

[Miller, 1973] Miller, J.H. and Green, A.E.S., *Proton energy degradation in water vapour.* Radiat. Res. 54, 343–363 (1973).

[Mitev, 2005] Mitev, K., Ségur, P., Alkaa, A., Bordage, M.C., Furstoss, C., Khamphan, C., De Nardo, L., Conte, V. and Colautti, P., *Study of non-equilibrium avalanches, application to proportional counters.* Nucl. Instrum. Meth. Phys. Res. A 538, 672–685 (2005).

[Nikjoo, 2006] Nikjoo, H., Uehara, S., Emfietzoglou, D. and Cucinotta, F.A., *Track-structure codes in radiation research.* Radiat. Meas. 41, 1052–1074 (2006).

[Peisert, 1984] Peisert, A. and Sauli, F., *Drift and diffusion of electrons in gases: a compilation* (CERN Technical Report 84-08). European Organization for Nuclear Research (1984).

[Porter, 1976] Porter, H.S., Jackman, C.H. and Green, A.E.S., *Efficiencies for production of atomic nitrogen and oxygen by relativistic proton impact in air.* J. Chem. Phys. 65, 154–167 (1976).

[Pszona, 2000] Pszona, S., Kula, J. and Marjanska, S., *A new method for measuring ion clusters produced by charged particles in nanometre track sections of DNA size.* Nucl. Instrum. Meth. Phys. Res. A 447, 601–607 (2000).

[Rogakou, 1998] Rogakou, E.P., Pilch, D.R., Orr, A.H., Ivanova, V.S. and Bonner, W.M., *DNA double-stranded breaks induce histone H2AX phosphorylation on serine 139.* J. Biol. Chem. 273, 5858–5868 (1998).

[Rudd, 1988] Rudd, M.E., *Differential cross sections for secondary electron production by proton impact.* Phys. Rev. A 38, 6129–6137 (1988).

[Rudd, 1992] Rudd, M.E., Kim, Y.K., Madison, D.H. and Gay, T.J., *Electron production in proton collisions with atoms and molecules: energy distributions.* Rev. Mod. Phys. 64, 441–490 (1992).

[Schardt, 2010] Schardt, D., Elsässer, T. and Schulz-Ertner, D., *Heavy-ion tumor therapy: physical and radiobiological benefits.* Rev. Mod. Phys. 82, 383–425 (2010).

[Schmidt, 1992] Schmdt, B. and Roncossek, M., *Drift velocity, longitudinal and transverse diffusion in hydrocarbons derived from distributions of single electrons.* Aust. J. Phys. 45, 351–363 (1992).

[Snyder, 1947] Snyder, H.S., *Fluctuations for proportional counters.* Phys Rev. 72, 181 (1947).

[Tran, 2015] Tran, H.N., El Bitar, Z., Champion, C., Karamitros, M., Bernal, M.A., Francis, Z., Ivantchenko, V., Lee, S.B., Shin, J.I. and Incerti, S., *Modeling proton and alpha elastic scattering in liquid water in* Geant4-DNA. Nucl. Instrum. Meth. Phys. Res. B 343, 132–137 (2015).

[Uehara, 1993] Uehara, S., Nikjoo, H. and Goodhead, D.T., Cross-sections for water vapour for the Monte Carlo electron track structure code from 10 eV to the MeV region. Phys. Med. Biol. 38, 1841–1858 (1993).

[Wang, 2013] Wang, M., Saha, J., Hada, M., Anderson, J.A., Pluth, J.M., O'Neill, P. and Cucinotta, F.A., *Novel Smad proteins localize to IR-induced double-strand breaks: interplay between TGF$\beta$ and ATM pathways.* Nucleic Acids Res. 41, 933–942 (2013).

[Weyrather, 2004] Weyrather, K. and Kraft, G., *RBE of carbon ions: experimental data and the strategy of RBE calculation for treatment planning.* Radiother. Oncol. 73(2), S161–S169 (2004).

[Wilson, 1975] Wilson, W.E. and Toburen, L.H., *Electron emission from proton-hydrocarbon-molecule collisions at $0.3 - 2.0$ MeV.* Phys. Rev. A 11 1303–1308 (1975).

[Ziegler, 1985] Ziegler, J., Biersack, J. and Littmark, U., *The stopping and ranges of ions in matter* (vol.1). Pergamon Press, Elmsford, New York (1985).

# Acknowledgements

This PhD journey would not have been completed without the large number of people who day by day gave me some of their time, some of their enthusiasm or also a good piece of advice in more than one occasion.

First of all, I wish to thank my supervisor, Dr. Valeria Conte, for accepting me as a PhD student, following me patiently during these three years and above all for sharing with me her enthusiasm for nanodosimetry: her rigorous scientific guidance has made me grow not only as a researcher but also as a person. The possibility of being a mother and a researcher at the same time does not seem so far-fetched now.

My sincerest thanks also to Dr. Paolo Colautti, for sharing with me his huge scientific experience on microdosimetry, nanodosimetry and gas detectors in general, for the intense scientific discussions, for his constant urging to try things out (*"Your intelligence lies in your hands!"*), and for providing support when I most needed it.

I also wish to thank my university co-supervisor, Prof. Silvia Lenzi, for giving me the opportunity to start this PhD journey and for being a constant source of support throughout the years.

My gratitude goes also to Prof. Berndt Grosswendt, for sharing with me his huge experience on interaction cross sections models and Monte Carlo codes. A heartfelt thank you also to Davide Moro, who first showed me "which buttons I need to press" in order to carry out measurements with the Startrack counter.

I also wish to express my heartfelt gratitude to Dr. Hans Rabus and Prof. Stefano Agosteo for accepting to evaluate my work and for the time they spent in reviewing this thesis.

For the day-to-day life in Legnaro, my heartfelt thank you to all the students, both master and PhD, who worked with the group and shared with me ideas, questions, skills or working times: Elisa, Sabina, Davide2, Stefano, Davide3, Anna2 and Lorenzo. Thanks also to Gabriele, for his dropping by at the end of the day and the lifts back home.

Outside the lab, a huge thank you goes also to all my PhDFriends around the world, for all the advice and for not allowing me to forget that *we are the normal ones*. In particular, thanks to Laura and Cate for the long chats, and to Alberto, for his wisdom of a life lived. Thanks also to Sabine, for not allowing me to overlook the broader perspective.

To all my other friends, a huge thank you for your support during all the years that we've known each other, and for putting up with me in these last few months. In particular, a big thank you to "the girls", for their cheeky questions and blunt honesty.

Thanks to Mattia, living example that a life can be rewritten from scratch at any time, and to Tex, a real friend, for being there at any hour if we need him. Thanks to Jeny, my

sister beyond the seas, and to Paola, the best friend I can never get rid of.

A huge thank you to my parents, for their constant support even when they don't really feel up to it, and to my grandparents, for their down-to-earth wisdom.

Finally, thanks to Davide, once again, for the unconditional love and never-ending support. And most important, for the future that is yet to come.

*Somewhere along the way, I discovered joy*
*as an act of defiance.*

Paul Hewson